Investigation of Ni/ZrO₂ catalysts for the hydrodeoxygenation of microalgae oil

Sebastian Dieter Foraita

„Mit meinem Gott überspringe ich Mauern." Psalm 18,30

Acknowledgment

It has been a long way and a hard piece of work. There are many people, who supported me all the way or significant parts of it and contributed to this thesis. I am deeply grateful and want to particularly thank them, here.

First of all I want to express my sincere gratitude to Johannes (Prof. Dr. Johannes A. Lercher) giving me an opportunity with this interesting topic in your high level and famous catalysis group. Thank you for teaching me well and your critical guidance with your broad knowledge in catalysis and science. I enjoyed the international style and experience of your group.

I thank Prof. Dr. Thomas Brück as my second examinor and project leader of the Algen-FlugKraft project supported by Bavarian Ministry of Economic Affairs and Media, Energy and Technology ("Bayerisches Staatsministerium für Wirtschaft und Medien, Energie und Technologie") and Bavarian State Ministry of Education, Science and the Arts ("Bayerisches Staatsministerium für Bildung und Kultus, Wissenschaft und Kunst").

I want to thank Chen, Eszter and Yue for their co-supervision as responsible subgroup leaders. Thank you for the help in planning experiments, discussing results and shaping paper manuscripts and presentations.

Many and special thank deserve to Gary (Prof. Gary Haller) for our fruitful collaboration, discussions, your patience and the additional guidance. I appreciate your advice a lot.

I am grateful to Don (Donald M. Camaioni) and John L. Fulton from Pacific Northwest National Laboratory (PNNL) for co-supervision, EXAFS-lessons, scientific discussions, good collaboration, overwhelming hospitality and the great time at the Advanced Photon Source in Argonne, IL and the PNNL in Richland, WA.

I appreciate the feedback and support of Andy, Oliver, Maricruz, Erika and André in daily lab situations and especially in our group's seminars.

I want to thank Dipl.-Min. Katia Rodewald for teaching me how to operate the High Resolution SEM and sharing her extensive experience with me and Dr. Gabriele Raudaschl-Sieber for solid state ^{29}Si-NMR measurements.

Symbols and Abbreviations

AAS	Atomic absorption spectroscopy
BAS	Brønsted acid site
BET	Brunauer-Emmett-Teller
CN	Coordination number
Conv.	Conversion
CRF	Common reporting format
c-ZrO$_2$	$cubic$-ZrO$_2$
D	Dispersion
d_A	Diameter of particle from element A
DFT	Density functional theory
EDX	Energy dispersive X-ray (spectroscopy)
Eq.	Equation
EU	European Union
EXAFS	Extended X-ray absorption fine structure
FAME	Fatty acid methyl ester
FID	Flame ionization detector
FT	Fourier transformation
GC	Gas chromatography
GHG	Green house gas
HDN	Hydrodenitrogenation

HDO	Hydrodeoxygenation
HDS	Hydrodesulfurization
HR-SEM	High resolution scanning electron microscopy
ICP-OES	Inductively Coupled Plasma Optical Emission Spectrometry
IR (spectroscopy)	Infrared spectroscopy
K	Reaction equilibrium constant
k	Reaction rate constant
LAS	Lewis acid site
LULUCF	Land use, land-use change and forestry
MS	Mass spectrometry
m-ZrO_2	$monoclinic$-ZrO_2
NERD	Non-esterified renewable diesel
p	Pressure
R	Radial distance in EXAFS
S	Selectivity
S_{BET}	Specific surface area, derived from BET-model
SEM	Scanning electron microscopy
T	Temperature
TEM	Transmission electron microscopy
TMS	Tetramethylsilan
TOF	Turnover frequency
TPD	Temperature programmed desorption (of NH_3 or CO_2)

TPIE	Temperature programmed isotope exchange
TPR	Temperature programmed reaction (commonly also used as Temperature programmed reduction)
t-ZrO$_2$	$tetragonal$-ZrO$_2$
UN	United Nations
wt%	Weight percent
X	Conversion
XANES	X-ray absorption near edge structure
XAS	X-ray absorption spectroscopy
XRD	X-ray diffraction
Y	Yield

Physical units

°C	Degree Celsius/centigrade
A	Ampere
Å	Ångstrom (= 10^{-10} m)
a	Year (*lat. annum*)
bar	Bar (= 10^5 Pa = 1 kg·m^{-1}·s^{-2})
cm^{-1}	Reciprocal centimeter (= $1.99·10^{-23}$ J)
eV	Electron volt (= $1.6·10^{-19}$ J)
g	Gram
h	Hour
Hz	Hertz (= s^{-1})
J	Joule (= 1 N·m)
L	Liter
m	Meter
min	Minute
mol	Mole
rpm	Rounds per minute (= min^{-1})
t	Metric ton (= 1000 kg)
T	Tesla
V	Volt

Abstract

The catalytic properties of metallic Ni supported on *monoclinic* and *tetragonal* ZrO_2 for hydrodeoxygenation of stearic acid was investigated. Due to a higher concentration of oxygen defect sites*, monoclinic* ZrO_2 supported catalysts were three times more active, because the adsorption of carboxylic acid was enhanced. An even higher activity was achieved by incorporation of SiO_2 into the ZrO_2 lattice. Those materials form novel nano-layers possessing Brønsted acid sites and high specific surface area.

Zusammenfassung

Die katalytischen Eigenschaften von metallischem Ni geträgert auf *monoklinem* und *tetragonalem* ZrO_2 wurden für die Hydrodeoxygenierung von Stearinsäure untersucht. Durch die höhere Konzentration von Sauerstoffdefektenstellen waren die auf *monoklinem* ZrO_2 geträgerten Katalysatoren dreimal aktiver, da die Adsorption der Carboxysäure erhöht wurde. Eine noch höhere Aktivität konnte durch den Einbau von SiO_2 in das ZrO_2 Gitter erreicht werden. Diese Materialien bilden neuartige Nanoschichten aus, die Brønsted-Säure-Zentren und eine hohe spezifische Oberfläche besitzen.

Table of Contents

Curriculum Vitae

List of Publications

Journal publications

Oral presentations

Poster presentations

Statutory Declaration

Chapter 1

Introduction and general background

Recent global political events led to an interim drop in crude oil prize (29 \$/barrel for Brent in January 2016)[1], pretending that the necessity to displace fossil fuels is less urgent. However, extreme weather events, even in moderate climate regions, are commonly agreed to be related to climate change and the increase of the average temperature worldwide. This rise of the mean global temperature is caused by the emissions of greenhouse gases (GHG).[2] The European Union (EU) has decided to restrict the increase of the mean global temperature to 2 °C above pre-industrial levels by mitigating the emissions of GHG by 20%, increase the share of renewable energy to 20% and raise energy efficiency by 20% until 2020 compared with the level from 1990 (Europe 2020 strategy targets).[3] The limit of 2 °C increase was adapted by the "Paris Agreement" under the United Nations Framework Convention on Climate Change.[4] CO_2 is the most abundant GHG, which is predominantly generated by the combustion of fossil fuels.[5] With a share of 18%, the transportation sector is still the second highest contributor of GHG-emissions in Germany (**Figure 1-1**),[6] consuming gasoline, diesel, kerosene and heavy fuel oil originated from fossil oil. Renewable fuels (*i.e.* biofuels) are the most promising approach to overcome these problems because they are considered as CO_2-neutral.[7] This means that the emitted amount of CO_2 by combustion of those biofuels is equal to the sequestered amount of CO_2, which is captured *via* photosynthesis during growth of the respective plant of origin.[8]

In a first generation of biofuels, ethanol is produced by fermentation of glucose from edible plants (*e.g.* corn and sugar cane). The second generation of biofuels is fatty acid methyl ester (FAME), known as bio-diesel, produced from vegetable oil (sunflower oil, palm oil, rapeseed oil) *via* transesterification with methanol. Those plant sources of the vegetable oil, however, compete with arable land necessary for food production and consume fresh water. Additionally, bio-diesel bears several technical and practical disadvantages compared to conventional diesel. Microalgae, however, are envisioned as a renewable source for the production of third generation biofuels, converted to hydrocarbon diesel (*i.e. green diesel*) by hydrodeoxygenation.[9]

Annual greenhouse gas emissions in Germany [Mio. t CO_2-equi.]
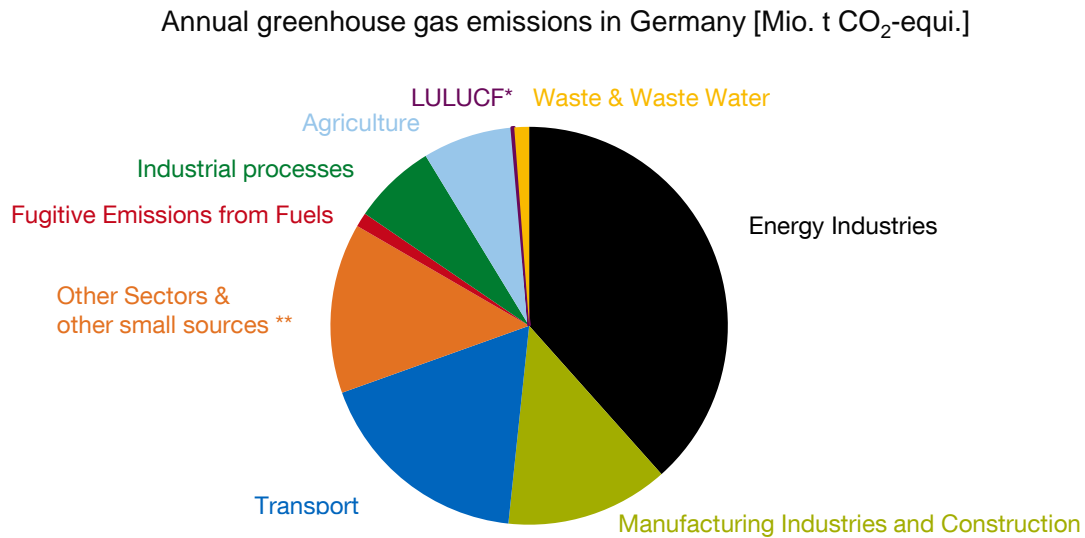
Figure 1-1. Annual greenhouse gas emissions in Germany in million tons CO_2 equivalent based on data from [6]: * Land use, land-use change and forestry; ** common reporting format

1.1 Microalgae – a renewable source of triglycerides for biofuels

Microalgae are either prokaryotic or eukaryotic photosynthetic microorganisms,[10] directly converting sunlight, CO_2 and nutrients into O_2 and biomass (*i.e.* mainly triglycerides, proteins and saccharides).[11] **Figure 1-2** shows a general molecular formula of a triglyceride representing microalgae oil. The photosynthetic rates of microalgae are higher than those of terrestrial plants and they capture 10% of incident solar energy.[5] Reaching up to 70 wt% of dry biomass,[12] the oil content is extraordinarily high and the growth rates are 10-20 times faster than conventional terrestrial oil plants (*e.g.* rapeseed, palm and sunflower).[10, 13] In contrast to the first- and second generation of biofuels, the third generation is advantageous from an ethical point of view, because the production of microalgae is not competing with agriculture, as no arable land is required.[10, 13-14] In general, microalgae are highly adaptable to extreme living conditions.[9b, 15] Halophile microalgae tolerate saline concentrations of seawater and above, which is a clear advantage at places with high sunlight radiation, often related to short fresh water supply that is more urgently needed for survival of the domestic population. In addition to that, salt water as growing media is more resistant against contamination.[14] The ideal setup for an integrated production of microalgae at large scale uses wastewater as N-source[14] and flue gas from fossil fuel power plants as CO_2-source.[10, 13]

When the algae is under nutrient stress (limitation of nitrogen or phosphorous), osmotic stress, radiation, (extreme) pH, temperature, heavy metals or other chemicals, the cell produces triglycerides. Those lipids provide an energy storage for the cell, enabling the microalgae to endure unfavorable environmental conditions. This is called *lipid induction*. Among those, the limitation of N-source is the most widely applied technique leading to the accumulation of storage compounds (*i.e.* triglyceride) within the algae cell.[16] In order to obtain the desired triglyceride out of the cell, it has to be extracted, which is economically and energetically the most crucial step in the concept of bio-fuels from microalgae. Methods for cell disruption includes high-pressure homogenization, bead beating, ultrasonication (micro-cavitation), treatment with microwaves, hydrothermal treatment, supercritical fluid extraction, solvent extraction and sulfuric acid treatment.[17]
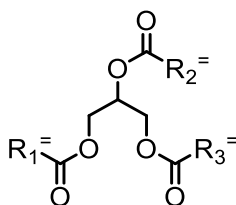
Figure 1-2. General molecular formular of a triglyceride – $R_1^=$, $R_2^=$ and $R_3^=$ are representing saturated or unsaturated fatty acid residues.

1.2   Routes of triglyceride conversion

Transesterification with alcohol is the most conventional route in upgrading triglycerides from vegetable oil, algae oil or waste fats that has been applied commercially so far (**Scheme 1-1**). The composition of a representative microalgae oil and the distribution of fatty acid residues is compiled in **Table 1-1**. Depending on the availability and economic considerations,[5, 18] the most common product is fatty acid methyl ester (FAME), usually blended with petroleum diesel and sold as Biodiesel.[19] Chemically, however, this Biodiesel is explicitly different to petroleum diesel, leading to several disadvantages. Due to the (relatively) high oxygen content, the energy density is lower compared to petroleum diesel. The flow quality at low temperatures is poor and the thermal- and oxidation stability is low,

requiring technical solutions necessary that go together with abrasive wear of the engine and parts thereof.[20]
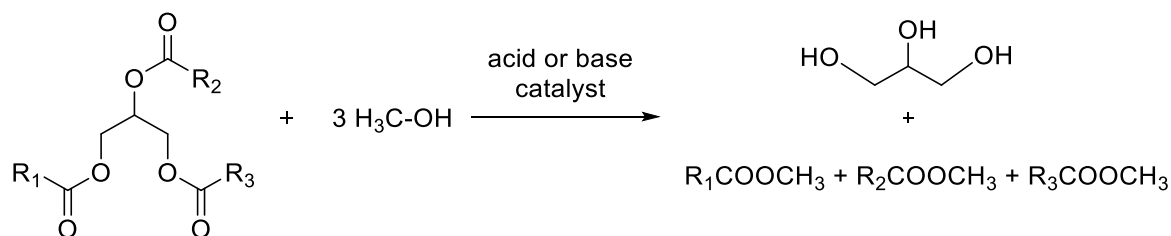
Scheme 1-1. Transesterification of triglyceride with methanol leading to glycerol and fatty acid methyl ester (FAME).

Table 1-1. Fatty acid composition of microalgae oil.[a]

Fatty acids composition [wt%]

$C_{14:0}$[b]	$C_{16:0}$	$C_{18:2}$	$C_{18:1}$	$C_{18:0}$	$C_{20:4}$	$C_{20:0}$	$C_{22:6}$	$C_{22:4}$	$C_{22:1}$	$C_{22:0}$	$C_{24:0}$	Sterol
0.04	4.41	56.2	32.2	4.41	0.07	0.43	0.13	0.19	0.97	0.44	0.36	0.12

[a] Crude microalgae oil provided by Verfahrenstechnik Schwedt GmbH.

[b] The nomenclature shows the number of carbon atoms and the number of C=C double bonds: *e.g.* the alkyl chain of the present fatty acid contains 14 C atoms and no double bonds ($C_{14:0}$).

This thesis, however, shall deal with a more sustainable approach, focusing on non-esterified renewable diesel (NERD) also referred to as *Green Diesel*. As stated above, the relatively high oxygen content of triglycerides and FAME is disadvantageous and oxygen has to be removed directly from the triglyceride to obtain long chain alkanes in the diesel range (C_9-C_{22}).[21] Similar to the removal of nitrogen through hydrodenitrogenation (HDN) and sulfur through hydrodesulfurization (HDS), oxygen can be removed *via* hydrotreating catalysts using H_2.[22] This removal of oxygen from an organic molecule with H_2 is called hydrodeoxygenation (HDO). Suitable catalysts are supported or unsupported transition metal sulfides (*e.g.* NiMo and CoMo sulfide)[23] which are already applied commercially for this purpose and offer the advantage of using an existing infrastructure.[24] With these catalysts, triglycerides can be converted to longchain and unbranched alkanes in the diesel range at process conditions of 10-200 bar H_2 at 350-450 °C.[25] This renewable diesel has high cetane numbers in the range of 70-90.[26] Transition metal sulfides catalysts, however, are not

ideal because they deactivate in such oxygen rich (*i.e.* sulfur free) feeds and contaminate the product with sulfur leached from the catalyst by a reverse Mars-van-Krevelen-mechanism.[27]

In order to overcome this drawback, sulfur free catalysts were developed. Catalytic deoxygenation of triglycerides and fatty acids was achieved with Ru, Pd, Pt, Re, Ir, Os, Mo, Rh and Ni supported on SiO_2, MgO, C, Al_2O_3 or zeolites (HBEA, H-ZSM-5).[28] Among those, Pd and Pt show the highest conversion of stearic acid and high selectivity towards *n*-heptadecane. Additionally and in contrast to hydrotreating, catalytic deoxygenation requires lower reaction temperature (250-300 °C),[28b] provides higher selectivity of the corresponding alkane and has lower consumption of H_2.[9b, 28a, 29]
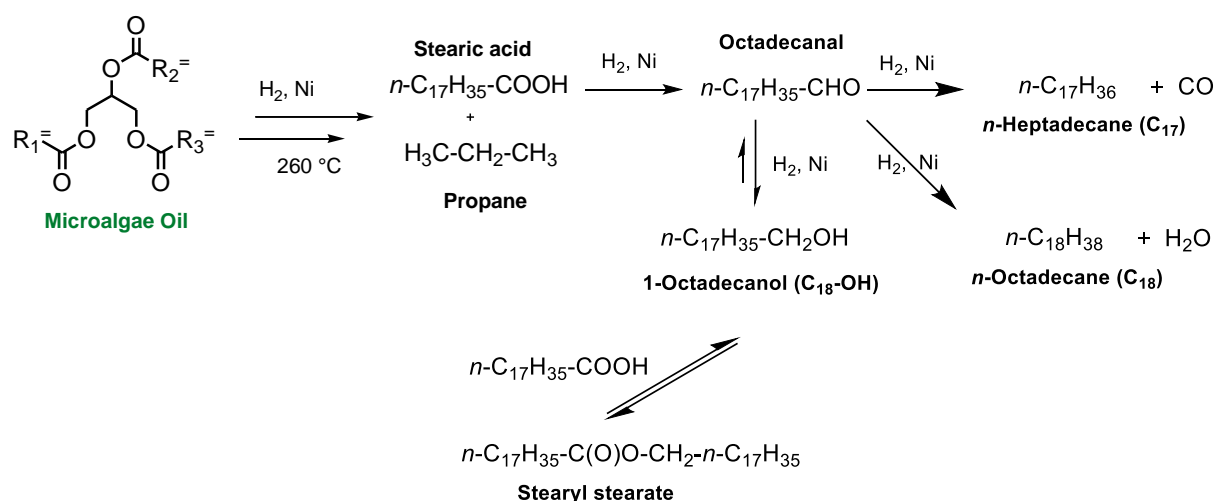
Scheme 1-2. Proposed reaction network for hydrogenation and hydrogenolysis of microalgae oil and the hydrodeoxygenation of stearic acid, showing the decarbonylation route towards *n*-heptadecane (C_{17}), dehydration/hydrogenation to *n*-octadecane (C_{18}) and reversible esterification towards stearyl stearate.

Starting with microalgae oil as a typical triglyceride (**Figure 1-2**), the deoxygenation to alkanes is carried out in a reaction sequence (**Scheme 1-2**). In a first step, the double bonds of the unsaturated fatty acid residues are hydrogenated (**Eq. 1**) and the ester bonds of the fatty acids with the glycerol backbone are cleaved *via* hydrogenolysis resulting in the formation of propane and carboxylic acid (**Eq. 2**). Those fatty acids (*e.g.* stearic acid) are hydrogenated (**Eq. 3**) leading to the corresponding aldehyde (octadecanal), that is equilibrated with alcohol (1-octadecanol) *via* hydrogenation-dehydrogenation (**Eq. 4**).[30] The de-

oxygenation of the aldehyde takes place *via* decarbonylation (-CO), without a net consumption of H_2 (**Eq. 5**), whereas the alcohol can be deoxygenated by Brønsted-acid-catalyzed dehydration with subsequent hydrogenation over transition metal (**Eq. 6** + **Eq. 1**).[31] Alternatively, the fatty acid can directly undergo decarboxylation (-CO_2, **Eq. 7**) on Pd/SiO_2 or hydrodeoxygenation (-H_2O, **Eq. 8**) on Pd/$NbOPO_4$.[32] Both decarbonylation and decarboxylation lead to the loss of one carbon atom, whereas the product formed by dehydration-hydrogenation or hydrodeoxygenation has the same carbon number as the substrate carboxylic acid. Therefore, decarbonylation and decarboxylation reaction consume less H_2, but the carbon economy is lower. The long chain alkane obtained *via* hydrodeoxygenation from microalgae oil is chemically indistinguishable from petroleum based diesel fuel.[33]

However, precious metals are costly and therefore their feasibility for industrial application is limited. Recently the quantitative conversion of both stearic acid and crude microalgae oil (without purification) was achieved with supported Ni catalysts, which is more economical.[31, 34] However, H-ZSM-5 (Si/Al = 45) used as a support there, lead to severe cracking, because of the high concentration of Brønsted acid sites. Consequently, those products do not fit in the diesel range. Obviously, in addition to the catalytically active metal, the support has significant contribution to the catalytic performance. After investigating a series of oxidic supports including SiO_2, Al_2O_3, TiO_2, CeO_2 and ZrO_2, ZrO_2 turned out to be the best one, enhancing the catalytic activity synergistically.[30]

In presence of a reducible oxide (*i.e.* ZrO_2), oxygen vacancies of ZrO_2 facilitate the concerted adsorption of stearic acid and H_2 activation (**Figure 1-3**). The oxygen vacancy from the transition metal oxide is (re)filled with an oxygen from the carboxylic group of the acid.[35] In line with that, a surface carboxylate is formed and α-hydrogen is abstracted forming a ketene intermediate,[36] which is in turn hydrogenated to aldehyde on Ni and subsequently decarbonylated to *n*-heptadecane and CO.[37] Therefore, the oxygen vacancy is an active site for the first hydrogenation/deoxygenation step and anchoring the reactant molecule. To regenerate the oxygen vacancy of ZrO_2, the abstracted α-hydrogen and the proton from the carboxylic acid OH-group recombine with oxygen bound to ZrO_2 forming H_2O. Hence, the selective hydrogenation of fatty acid to aldehyde takes place *via* a Mars-van-Krevelen-mechanism.[38] The bond strength of the metal oxide is crucial and has to be balanced that facilitates both the creation of the vacancy and the adsorption of the carboxylic

groups in fatty acids.[35] Together, the redundancy function of Ni and ZrO_2 enhances the overall hydrodeoxygenation of stearic acid.
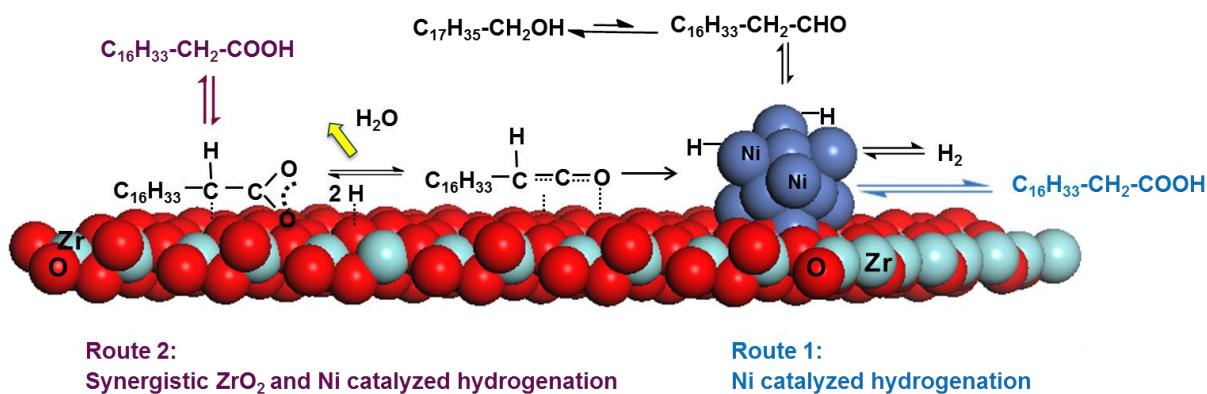
Figure 1-3. Proposed reaction mechanism of the hydrogenation of stearic acid to octadecanal by synergistic catalysis over Ni/ZrO_2 in the presence of H_2 (adapted from [37a] with permission of John Wiley and Sons).

The important reactions during the hydrodeoxygenation process are summarized in **Eq. 1-8**:

Equation 1   Hydrogenation of double bond (*e.g.* oleic acid):
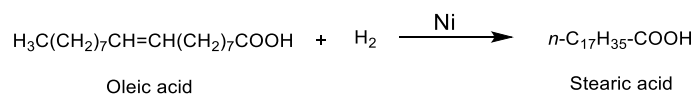
Equation 2   Ester hydrogenolysis:
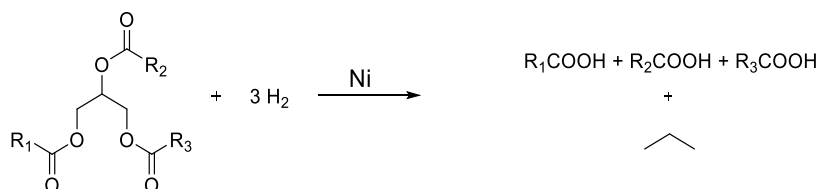
Equation 3   Hydrogenation of carboxylic acid to aldehyde:

$$n\text{-}C_{17}H_{35}\text{-}COOH \quad + H_2 \quad \xrightarrow{[Ni]} \quad n\text{-}C_{16}H_{33}\text{-}CH_2\text{-}C\overset{O}{\underset{H}{\diagdown}} \quad + H_2O$$

Stearic acid   Octadecanal
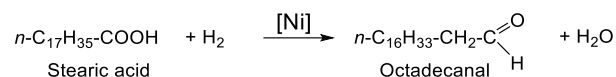
Equation 4   Hydrogenation of aldehyde to alcohol and equilibrated with reverse reaction:

$$n\text{-}C_{16}H_{33}\text{-}CH_2\text{-}C\overset{O}{\underset{H}{\diagdown}} \quad + H_2 \quad \underset{\longleftarrow}{\overset{[Ni]}{\longrightarrow}} \quad n\text{-}C_{17}H_{35}\text{-}CH_2OH$$

Octadecanal   1-Octadecanol
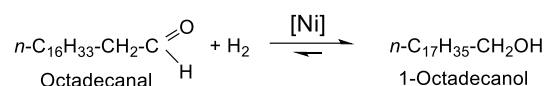
Equation 5   Decarbonylation of aldehyde:

$$n\text{-}C_{16}H_{33}\text{-}CH_2\text{-}C\overset{O}{\underset{H}{\diagdown}} \quad \xrightarrow{[Ni]} \quad n\text{-}C_{17}H_{36} \quad + CO$$
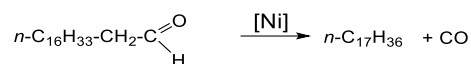
Equation 6   Dehydration of alcohol to alkene:

$$n\text{-}C_{16}H_{33}\text{-}CH_2\text{-}CH_2OH \quad \xrightarrow{[H^+]} \quad n\text{-}C_{16}H_{33}\text{-}CH=CH_2 \quad + H_2O$$

1-Octadecanol   1-Octadecene
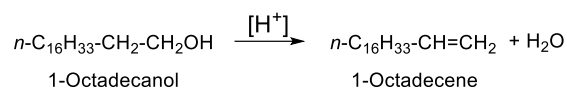
Equation 7   Decarboxylation of carboxylic acid to alkane:

$$n\text{-}C_{17}H_{35}\text{-}COOH \quad + H_2 \quad \xrightarrow{[Pd/SiO_2]} \quad n\text{-}C_{17}H_{36} \quad + CO_2$$

Stearic acid   n-heptadecane
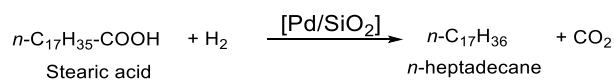
Equation 8   Hydrodeoxygenation of carboxylic acid to alkane:

$$n\text{-}C_{17}H_{35}\text{-}COOH \quad + 3 H_2 \quad \xrightarrow{[Pd/NbOPO_4]} \quad n\text{-}C_{17}H_{36} \quad + 2 H_2O$$

Stearic acid   n-heptadecane
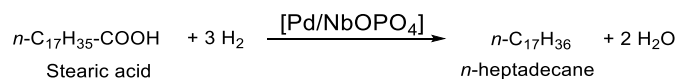
1.3 ZrO₂ – a multifunctional catalyst support

1.3.1 General properties of ZrO₂

Among other disciplines, ZrO_2 is highly appreciated especially in heterogeneous catalysis *inter alia* due to its excellent mechanical properties, porosity, low thermal conductivity, stable surface area at high temperature, high resistance to corrosion and high melting point (2680 °C).[39] Additionally, ZrO_2 uniquely possesses acid- and base sites as well as oxidizing and reducing properties.[40]

1.3.2 Crystal phases of ZrO₂

Zirconia occurs in four polymorphs,[41] *i.e. monoclinic* (*m-*) at ambient temperature until 1170 °C, *tetragonal* (*t-*) between 1170 and 2370 °C, *cubic* (*c-*) until the melting point (2370-2680 °C) and orthorhombic forming only at elevated pressures (**Scheme 1-3**).[42] At ambient conditions, *monoclinic* is the predominant phase and represented by the mineral Baddeleyite in nature. *Tetragonal*-phase, however, has the highest mechanical strength and is more suitable for ceramic applications.[42d, 43] Ideally, the crystal structure of *c*-ZrO_2 is based on a CaF_2 lattice type,[44] where Zr is eightfold coordinated with oxygen and every O is tetrahedrally coordinated by Zr. In *t*-ZrO_2, the crystal lattice shows only small deviations from the ideal CaF_2-structure and still an eightfold coordination of Zr.[45] In contrast to that, *m*-ZrO_2 is considerably more distorted with respect to the ideal CaF_2-structure and the Zr^{4+} cation is sevenfold coordinated with oxygen, whereas O is either trigonally or tetrahedrally coordinated by Zr. Detailed crystallographic structures are extensively discussed and visualized in literature.[44-46]

$$\textit{monoclinic } ZrO_2 \underset{950\ °C}{\overset{1170\ °C}{\rightleftharpoons}} \textit{tetragonal } ZrO_2 \overset{2370\ °C}{\rightleftharpoons} \textit{cubic } ZrO_2 \overset{2680\ °C}{\rightleftharpoons} ZrO_2 \text{ (liquid)}$$
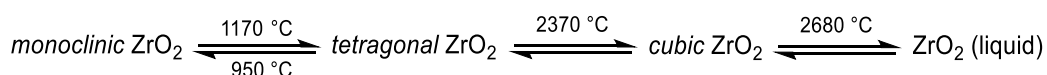
Scheme 1-3. Phase transition of ZrO_2 as a function of temperature.

1.3.3 Generation of Lewis- and Brønsted acid sites on the surface of ZrO₂

Pure ZrO_2 almost exclusively shows Lewis acidic properties, as it was shown by IR spectroscopy of adsorbed pyridine that is coordinately bound to the surface of ZrO_2, whereas Brønsted acid sites are absent.[47] By mixing with another oxide, Brønsted acid sites can be generated on ZrO_2. According to **Thomas' model**, a cation of a metal that is isomorphously substituted into a metal oxide structure comprised of a cation with higher charge (*e.g.* Al^{3+} into SiO_2), would need a balancing charge, which is most likely a proton.[48] That means, Al adapts the tetrahedral coordination of oxygen and the resulting charge deficit has to be compensated by a proton associated with it. This proton is acidic (**Scheme 1-4**).
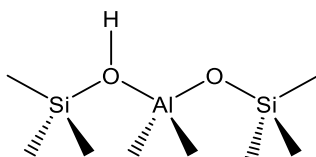
Scheme 1-4. Schematic representation for the generation/formation of an acidic proton in a mixed SiO_2-Al_2O_3 oxide.[49]

However, this model does not explain the generation of acidity for binary metal oxides (chemically bonded), when both cations have the same charge (*e.g.* SiO_2-ZrO_2). **Tanabe** *et al.* elaborated the model, stated above, taking into account the coordination numbers CN of the oxygen anion and both of the cations.[50] It is based on two fundamental assumptions:

i)   They hypothesized that in a model structure, the coordination number of each metal cation is maintained as in its pure oxide.

ii) On the contrary, all oxygen anions of a binary metal oxide retain the coordination number of the major (oxide) component.

A charge imbalance formed by this is generating either LAS or BAS. A positive excess charge is generating a LAS, whereas a negative excess charge is the reason for a BAS. The example SiO_2-ZrO_2 is shown in **Scheme 1-5**. For ZrO_2-rich mixed oxides, the four positive charges of Si are distributed to four bonds (+4/4) and two negative charges of an oxygen anion are shared by four bonds (-2/4), *i.e.* the coordination of oxygen in ZrO_2, according to assumption i) in Tanabe's hypothesis. The charge difference for one bond is $+1 - \frac{1}{2} = +\frac{1}{2}$

and $4 \cdot \left(+\frac{1}{2} \right) = +2$ for the whole valence unit (**Scheme 1-5, A**). Therefore, Lewis acidity is predicted (electron acceptor), which is in agreement with experimental observations.[51] If the major part of the binary oxide is SiO_2 (**Scheme 1-5, B**), four positive charges of Zr are distributed among eight bonds $\left(+\frac{4}{8} \right)$, while two negative charges are shared between two bonds $\left(-\frac{2}{2} \right)$. The result for the whole valence unit is $8 \cdot \left(+\frac{1}{2} - 1 \right) = -4$. Negative excess charge requires a proton to balance it and thus imparts Brønsted acidity.[52]
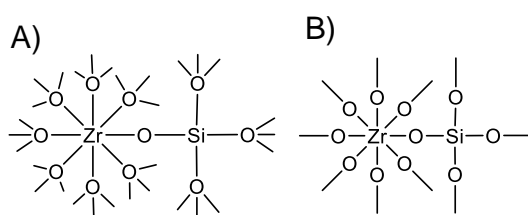
Scheme 1-5. Model structure of SiO_2-ZrO_2 mixed oxide unit considering assumptions i) and ii). **A)** ZrO_2-rich binary oxide (containing LAS), **B)** SiO_2 is the major component (containing BAS).

However, this model is lacking an explanation for the simultaneous presence of both BAS and LAS at the same material in most of the binary oxides. This can be explained by the concept of micro-regions,[53] where inhomogeneities of the mixed oxides being responsbile for either of the oxide beeing the major or minor part, respectively. Nevertheless, they are assuming that the coordination number of the cation is not changing in the mixed oxide.[50, 53] This is not the case for SiO_2-TiO_2, as demonstrated experimentally by EXAFS and XRD.[54] Miller and Ko are generally following Tanabe's model explaining the generation of BAS and LAS and mention the heterolinkage Si-O-Zr as the acid site. Additionally, they point out that Zr enters the SiO_2-network maintaining its coordination number of 7 or 8.[52]

Kataoka and Dumesic also use valence and coordination of the cation to explain the generation of acidity in binary metal oxides, derived from Paulings electrostatic valence rule.[55] Different valence and coordination number of the cations generate undersaturated oxygen, that are compensated by Si-O-Zr bridges bearing a formal negative charge as in the case of SiO_2-Al_2O_3.[56] Therefore, an acidic proton, located at the Si-O-Zr bond, is necessary to compensate the neative charge at the bridging oxygen.[56] Formally, this can be imagined like Thomas' model (**Scheme 1-4**, page 10).

1.4 Bimetallic catalysts for hydrodeoxygenation

In the previous chapter 1.2 (page 3), sulfur free catalysts were presented for the hydrodeoxygenation of triglycerides and fatty acids. Unfortunately, the most active and selective metals (*i.e.* Pd and Pt) are precious metals and rather expensive. Base metals (*e.g.* Ni, Co, Cu, Fe, Mo), as a more economic alternative, suffer from lower activity, stability, recyclability and selectivity, especially under the circumstances of biomass feeds with high chemical complexity.[57] Therefore, the combination of two active metals is a promising option to optimize such catalysts in terms of catalytic parameters, mechanical properties and economic feasibility.

Combinations of Pt, Pd and Ru with Ni, Co, Cu, Fe and Mo are successfully investigated in the de-functionalization of sugar monomers and polysaccharides (especially cellulose), glycerol, hemicellulose, furfural, fatty acid esters, carboxylic acids, lignin and derivatives thereof.[58]

The advantageous effect of the second metal is that it helps reducing the first one or keep it reduced.[59] Further, there are geometric effects altering the geometry of the active site, electronic effects by electron transfer between metals,[58d, 60] stabilizing effects (preventing particles to sinter or the deposition of coke), synergistic effects (both metals interact forming intermediates and transitions states) or bi-functional effects (*i.e.* both metal species contribute with different catalytic functions).[57] The beneficial effect of the bimetallic catalysts is often related to the formation of an alloy.[61] The properties of such an alloy are distinct from those of the individual metals.[62] Ni particles alloyed with Pt for example are smaller and stronger bound to the support.[59, 63] Also the higher activity of Ni-Pt-catalysts for hydrogenation of propanal is related to lower binding energy of propanal on the Ni-Pt-Ni(111) subsurface as it is characterized by TPD and DFT calculations.[64] In a very recent contribution, Ni catalysts were promoted with Cu, Au, Ag, Ru, Rh, Pd, Ir, Fe, Co, Ni, and Sn in order to investigate the hydrogenolysis of lignin. Here, especially Au improves the activity due to smaller Ni-particle size and higher dispersion.[65] Nevertheless, it is costly to use noble metals like Au, Pd, and Pt to form the bimetallic species.

Besides the emerging popularity of research on bimetallic catalysts and the advances made, there is still a lack of knowledge on the mechanism responsible for these improvements, and more studies are required to establish correlations between results and catalyst modifications at the molecular level [57].

1.5 Scope of the thesis

The aim of this thesis is to further understand and develop active catalysts for the hydrodeoxygenation of stearic acid working at mild conditions based on Ni/ZrO_2. Therefore, supported metal catalysts were independently investigated by the impact of the support on the one hand side and the effect of the active metal species on the other hand side. The influence of the support on activity and selectivity will be pointed out. It was investigated in two aspects: First, the impact of the crystal phase of ZrO_2 was examined, that synergistically enhances the catalyst activity and providing a higher concentration of oxygen vacancies. Therefore, pure phases of *monoclinic* and *tetragonal* ZrO_2 were synthesized and examined *inter alia* by means of EDX-TEM, XAS and isotopic exchange experiments. Second, ZrO_2 was modified with a hydrothermal synthesis or an impregnation with SiO_2, introducing a novel morphology, increasing the specific surface area and changing the acid-base-properties by the introduction of Brønsted acid sites, shown by high resolution SEM and IR of adsorbed pyridine. This further increases the activity and shifts the selectivity. Moreover, the effect of the metal site was examined. Ni was mixed with Cu that is also an economic metal and reported to be highly active in hydrogenation of carboxylic acid. Physical mixtures with close proximity of Ni and Cu are compared with a Ni_xCu_{1-x}-alloy obtained by co-impregnation. This promotes the hydrodeoxygenation of stearic acid by faster conversion of the substrate and a more rapid formation of long chain alkane in the diesel range (*n*-heptadecane).

1.6 References

1. NASDAQ, Crude Oil Brent. http://www.nasdaq.com/markets/crude-oil-brent.aspx (accessed 20.01.2016).
2. Armaroli, N.; Balzani, V., The future of energy supply: challenges and opportunities. *Angew. Chem., Int. Ed.* **2007,** *46*, 52-66.
3. European Union, Smarter, greener, more inclusive? Indicators to support the Europe 2020 strategy. http://ec.europa.eu/eurostat/documents/3217494/6655013/KS-EZ-14-001-EN-N.pdf/a5452f6e-8190-4f30-8996-41b1306f7367 (accessed 13.03.2016).
4. UN, Paris Agreement. http://unfccc.int/files/essential_background/convention/application/pdf/english_paris_agreement.pdf (accessed 02.10.2016).

5. Huber, G. W.; Iborra, S.; Corma, A., Synthesis of Transportation Fuels from Biomass: Chemistry, Catalysts, and Engineering. *Chem. Rev.* **2006,** *106*, 4044-4098.

6. Umweltbundesamt, Jährliche Treibhausgas-Emissionen in Deutschland. http://www.umweltbundesamt.de/themen/klima-energie/klimaschutz-energiepolitik-in-deutschland/treibhausgas-emissionen/emissionsquellen (accessed 02.10.2016).

7. Ragauskas, A. J.; Williams, C. K.; Davison, B. H.; Britovsek, G.; Cairney, J.; Eckert, C. A.; Frederick, W. J., Jr.; Hallett, J. P.; Leak, D. J.; Liotta, C. L.; Mielenz, J. R.; Murphy, R.; Templer, R.; Tschaplinski, T., The path forward for biofuels and biomaterials. *Science (Washington, DC, U. S.)* **2006,** *311*, 484-489.

8. Cherubini, F.; Peters, G. P.; Berntsen, T.; Strømman, A. H.; Hertwich, E., CO_2 emissions from biomass combustion for bioenergy: atmospheric decay and contribution to global warming. *GCB Bioenergy* **2011,** *3*, 413-426.

9. (a) Chen, Y.; Wu, Y.; Hua, D.; Li, C.; Harold, M. P.; Wang, J.; Yang, M., Thermochemical conversion of low-lipid microalgae for the production of liquid fuels: challenges and opportunities. *RSC Adv.* **2015,** *5*, 18673-18701; (b) Zhao, C.; Bruck, T.; Lercher, J. A., Catalytic deoxygenation of microalgae oil to green hydrocarbons. *Green Chem.* **2013,** *15*, 1720-1739.

10. Mata, T. M.; Martins, A. A.; Caetano, N. S., Microalgae for biodiesel production and other applications: A review. *Renewable Sustainable Energy Rev.* **2010,** *14*, 217-232.

11. Babich, I. V.; van der Hulst, M.; Lefferts, L.; Moulijn, J. A.; O'Connor, P.; Seshan, K., Catalytic pyrolysis of microalgae to high-quality liquid bio-fuels. *Biomass Bioenergy* **2011,** *35*, 3199-3207.

12. Metting, F. B., Biodiversity and application of microalgae. *J. Ind. Microbiol. 17*, 477-489.

13. Borowitzka, M. A.; Moheimani, N. R., *Algae for Biofuels and Energy*. Springer: Heidelberg New York London, 2013.

14. Brennan, L.; Owende, P., Biofuels from microalgae – A review of technologies for production, processing, and extractions of biofuels and co-products. *Renewable Sustainable Energy Rev.* **2010,** *14*, 557-577.

15. Pulz, O.; Gross, W., Valuable products from biotechnology of microalgae. *Appl. Microbiol. Biotechnol.* **2004,** *65*, 635-648.

16. Sharma, K. K.; Schuhmann, H.; Schenk, P. M., High lipid induction in microalgae for biodiesel production. *Energies* **2012,** *5*, 1532-1553.

17. (a) Halim, R.; Harun, R.; Danquah, M. K.; Webley, P. A., Microalgal cell disruption for biofuel development. *Appl. Energy* **2012,** *91*, 116-121; (b) Lee, J.-Y.; Yoo, C.; Jun, S.-Y.; Ahn, C.-Y.; Oh, H.-M., Comparison of several methods for effective lipid extraction from microalgae. *Bioresour. Technol.* **2010,** *101*, S75-S77; (c) Mercer, P.;

Armenta, R. E., Developments in oil extraction from microalgae. *Eur. J. Lipid Sci. Technol.* **2011,** *113*, 539-547.

18. Šimáček, P.; Kubička, D.; Šebor, G.; Pospíšil, M., Hydroprocessed rapeseed oil as a source of hydrocarbon-based biodiesel. *Fuel* **2009,** *88*, 456-460.

19. Benjumea, P.; Agudelo, J.; Agudelo, A., Basic properties of palm oil biodiesel–diesel blends. *Fuel* **2008,** *87*, 2069-2075.

20. (a) Silva, L. N.; Fortes, I. C. P.; de Sousa, F. P.; Pasa, V. M. D., Biokerosene and green diesel from macauba oils via catalytic deoxygenation over Pd/C. *Fuel* **2016,** *164*, 329-338; (b) Haseeb, A. S. M. A.; Fazal, M. A.; Jahirul, M. I.; Masjuki, H. H., Compatibility of automotive materials in biodiesel: A review. *Fuel* **2011,** *90*, 922-931.

21. Li, G.; Li, N.; Yang, J.; Li, L.; Wang, A.; Wang, X.; Cong, Y.; Zhang, T., Synthesis of renewable diesel range alkanes by hydrodeoxygenation of furans over Ni/Hβ under mild conditions. *Green Chem.* **2014,** *16*, 594-599.

22. (a) Kubička, D.; Horáček, J., Deactivation of HDS catalysts in deoxygenation of vegetable oils. *Appl. Catal., A* **2011,** *394*, 9-17; (b) Kubička, D.; Kaluža, L., Deoxygenation of vegetable oils over sulfided Ni, Mo and NiMo catalysts. *Appl. Catal., A* **2010,** *372*, 199-208.

23. Bezergianni, S.; Dimitriadis, A.; Meletidis, G., Effectiveness of CoMo and NiMo catalysts on co-hydroprocessing of heavy atmospheric gas oil–waste cooking oil mixtures. *Fuel* **2014,** *125*, 129-136.

24. (a) Veriansyah, B.; Han, J. Y.; Kim, S. K.; Hong, S.-A.; Kim, Y. J.; Lim, J. S.; Shu, Y.-W.; Oh, S.-G.; Kim, J., Production of renewable diesel by hydroprocessing of soybean oil: Effect of catalysts. *Fuel* **2012,** *94*, 578-585; (b) Jakkula, J.; Niemi, V.; Nikkonen, J.; Purola, V.-M.; Myllyoja, J.; Aalto, P.; Lehtonen, J.; Alopaeus, V. Process for producing a hydrocarbon component of biological origin. EP1396531A2, 2004.

25. Sotelo-Boyas, R.; Liu, Y.; Minowa, T., Renewable diesel production from the hydrotreating of rapeseed oil with Pt/Zeolite and NiMo/Al$_2$O$_3$ catalysts. *Ind. Eng. Chem. Res.* **2011,** *50*, 2791-2799.

26. Kalnes, T.; Marker, T.; Shonnard, D. R., Green Diesel: A Second Generation Biofuel. *Int. J. Chem. React. Eng.* **2007,** *5 (A48)*, 1-9.

27. (a) Furimsky, E., Chemistry of Catalytic Hydrodeoxygenation. *Catal. Rev.* **1983,** *25*, 421-458; (b) Viljava, T. R.; Komulainen, R. S.; Krause, A. O. I., Effect of H$_2$S on the stability of CoMo/Al$_2$O$_3$ catalysts during hydrodeoxygenation. *Catal. Today* **2000,** *60*, 83-92.

28. (a) Snåre, M.; Kubičková, I.; Mäki-Arvela, P.; Eränen, K.; Murzin, D. Y., Heterogeneous Catalytic Deoxygenation of Stearic Acid for Production of Biodiesel. *Ind. Eng. Chem. Res.* **2006,** *45*, 5708-5715; (b) Murata, K.; Liu, Y.; Inaba, M.;

Takahara, I., Production of Synthetic Diesel by Hydrotreatment of Jatropha Oils Using Pt−Re/H-ZSM-5 Catalyst. *Energy Fuels* **2010,** *24*, 2404-2409.

29. Snåre, M.; Kubičková, I.; Mäki-Arvela, P.; Chichova, D.; Eränen, K.; Murzin, D. Y., Catalytic deoxygenation of unsaturated renewable feedstocks for production of diesel fuel hydrocarbons. *Fuel* **2008,** *87*, 933-945.

30. Peng, B.; Yuan, X.; Zhao, C.; Lercher, J. A., Stabilizing Catalytic Pathways via Redundancy: Selective Reduction of Microalgae Oil to Alkanes. *J. Am. Chem. Soc.* **2012,** *134*, 9400-9405.

31. Peng, B.; Yao, Y.; Zhao, C.; Lercher, J. A., Towards Quantitative Conversion of Microalgae Oil to Diesel-Range Alkanes with Bifunctional Catalysts. *Angew. Chem., Int. Ed.* **2012,** *51*, 2072-2075.

32. (a) Huber, G. W.; O'Connor, P.; Corma, A., Processing biomass in conventional oil refineries: Production of high quality diesel by hydrotreating vegetable oils in heavy vacuum oil mixtures. *Appl. Catal., A* **2007,** *329*, 120-129; (b) Maier, W. F.; Roth, W.; Thies, I.; Schleyer, P. v. R., Gas phase decarboxylation of carboxylic acids. *Chem. Ber.* **1982,** *115*, 808-812; (c) Xia, Q.; Zhuang, X.; Li, M. M.-J.; Peng, Y.-K.; Liu, G.; Wu, T.-S.; Soo, Y.-L.; Gong, X.-Q.; Wang, Y.; Tsang, S. C. E., Cooperative catalysis for the direct hydrodeoxygenation of vegetable oils into diesel-range alkanes over Pd/NbOPO₄. *Chem. Commun.* **2016,** *52*, 5160-5163.

33. Choudhary, T. V.; Phillips, C. B., Renewable fuels via catalytic hydrodeoxygenation. *Appl. Catal., A* **2011,** *397*, 1-12.

34. Kordulis, C.; Bourikas, K.; Gousi, M.; Kordouli, E.; Lycourghiotis, A., Development of nickel based catalysts for the transformation of natural triglycerides and related compounds into green diesel: a critical review. *Appl. Catal., B* **2016,** *181*, 156-196.

35. Pestman, R.; Koster, R. M.; Pieterse, J. A. Z.; Ponec, V., Reactions of carboxylic acids on oxides. 1. Selective hydrogenation of acetic acid to acetaldehyde. *J. Catal.* **1997,** *168*, 255-264.

36. (a) Pestman, R.; Koster, R. M.; van Duijne, A.; Pieterse, J. A. Z.; Ponec, V., Reactions of Carboxylic Acids on Oxides: 2. Bimolecular Reaction of Aliphatic Acids to Ketones. *J. Catal.* **1997,** *168*, 265-272; (b) Rajadurai, S., Pathways for Carboxylic Acid Decomposition on Transition Metal Oxides. *Catal. Rev.: Sci. Eng.* **1994,** *36*, 385-403; (c) Pestman, R.; van Duijne, A.; Pieterse, J. A. Z.; Ponec, V., The formation of ketones and aldehydes from carboxylic acids, structure-activity relationship for two competitive reactions. *J. Mol. Catal. A: Chem.* **1995,** *103*, 175-180.

37. (a) Peng, B.; Zhao, C.; Kasakov, S.; Foraita, S.; Lercher, J. A., Manipulating Catalytic Pathways: Deoxygenation of Palmitic Acid on Multifunctional Catalysts. *Chem. - Eur. J.* **2013,** *19*, 4732-4741; (b) Grootendorst, E. J.; Pestman, R.; Koster,

R. M.; Ponec, V., Selective reduction of acetic acid to acetaldehyde on iron oxides. *J. Catal.* **1994,** *148*, 261-9.

38. Pestman, R.; Koster, R. M.; Boellaard, E.; van der Kraan, A. M.; Ponec, V., Identification of the Active Sites in the Selective Hydrogenation of Acetic Acid to Acetaldehyde on Iron Oxide Catalysts. *J. Catal.* **1998,** *174*, 142-152.

39. (a) Foster, A. S.; Sulimov, V. B.; Lopez, G. F.; Shluger, A. L.; Nieminen, R. M., Structure and electrical levels of point defects in monoclinic zirconia. *Phys. Rev. B: Condens. Matter Mater. Phys.* **2001,** *64*, 224108/1-224108/10; (b) Bachiller-Baeza, B.; Rodriguez-Ramos, I.; Guerrero-Ruiz, A., Interaction of Carbon Dioxide with the Surface of Zirconia Polymorphs. *Langmuir* **1998,** *14*, 3556-3564; (c) Garvie, R. C.; Hannink, R. H.; Pascoe, R. T., Ceramic steel? *Nature* **1975,** *258*, 703-704.

40. Tanabe, K., Surface and catalytic properties of ZrO_2. *Mater. Chem. Phys.* **1985,** *13*, 347-364.

41. Li, P.; Chen, I. W.; Penner-Hahn, J. E., X-ray absorption studies of zirconia polymorphs. I. Characteristic local structures. *Phys. Rev. B: Condens. Matter* **1993,** *48*, 10063-73.

42. (a) Bondars, B.; Heidemane, G.; Grabis, J.; Laschke, K.; Boysen, H.; Schneider, J.; Frey, F., Powder diffraction investigations of plasma sprayed zirconia. *J. Mater. Sci.* **1995,** *30*, 1621-1625; (b) Barker, W. W.; Bailey, F. P.; Garrett, W., A high-temperature neutron diffraction study of pure and scandia-stabilized zirconia. *J. Solid State Chem.* **1973,** *7*, 448-453; (c) Karapetrova, E.; Platzer, R.; Gardner, J. A.; Torne, E.; Sommers, J. A.; Evenson, W. E., Oxygen vacancies in pure tetragonal zirconia powders: dependence on the presence of chlorine during processing. *J. Am. Ceram. Soc.* **2001,** *84*, 65-70; (d) Bocanegra-Bernal, M. H.; de la Torre, S. D., Phase transitions in zirconium dioxide and related materials for high performance engineering ceramics. *J. Mater. Sci.* **2002,** *37*, 4947-4971.

43. Gupta, T. K.; Lange, F. F.; Bechtold, J. H., Effect of stress-induced phase transformation on the properties of polycrystalline zirconia containing metastable tetragonal phase. *J. Mater. Sci.* **1978,** *13*, 1464-1470.

44. Smith, D. K.; Newkirk, H. W., The Crystal Structure of Baddeleyite (Monoclinic ZrO_2) and its Relation to the Polymorphism of ZrO_2. *Acta Crystallogr.* **1965,** *18*, 983-91.

45. Jacob, K. H.; Knoezinger, E.; Benier, S., Adsorption sites on polymorphic zirconia. *J. Mater. Chem.* **1993,** *3*, 651-7.

46. (a) McCullough, J. D.; Trueblood, K. N., The crystal structure of baddeleyite (monoclinic ZrO_2). *Acta Crystallogr.* **1959,** *12*, 507-11; (b) Finnis, M. W.; Paxton, A. T.; Methfessel, M.; van Schilfgaarde, M., Crystal Structures of Zirconia from First Principles and Self-Consistent Tight Binding. *Phys. Rev. Lett.* **1998,** *81*, 5149-5152; (c) Onyestyák, G.; Harnos, S.; Kalló, D., Improving the catalytic behavior of

Ni/Al$_2$O$_3$ by indium in reduction of carboxylic acid to alcohol. *Catal. Commun.* **2011,** *16*, 184-188.

47. Nakano, Y.; Iizuka, T.; Hattori, H.; Tanabe, K., Surface properties of zirconium oxide and its catalytic activity for isomerization of 1-butene. *J. Catal.* **1979,** *57*, 1-10.

48. Thomas, C. L., Chemistry of Cracking Catalysts. *Ind. Eng. Chem.* **1949,** *41*, 2564-2573.

49. (a) Jacobs, P. A.; Von Ballmoos, R., Framework hydroxyl groups of H-ZSM-5 zeolites. *J. Phys. Chem.* **1982,** *86*, 3050-3052; (b) Boronat, M.; Corma, A., Factors Controlling the Acidity of Zeolites. *Catal. Lett.* **2015,** *145*, 162-172; (c) Knözinger, H.; Huber, S., IR spectroscopy of small and weakly interacting molecular probes for acidic and basic zeolites. *J. Chem. Soc., Faraday Trans.* **1998,** *94*, 2047-2059.

50. Tanabe, K.; Sumiyoshi, T.; Shibata, K.; Kiyoura, T.; Kitagawa, J., New hypothesis regarding the surface acidity of binary metal oxides. *Bull. Chem. Soc. Jpn.* **1974,** *47*, 1064-6.

51. Anderson, J. A.; Fergusson, C.; Rodríguez-Ramos, I.; Guerrero-Ruiz, A., Influence of Si/Zr ratio on the formation of surface acidity in silica-zirconia aerogels. *J. Catal.* **2000,** *192*, 344-354.

52. Miller, J. B.; Ko, E. I., Acidic Properties of Silica-Containing Mixed Oxide Aerogels:Preparation and Characterization of Zirconia–Silica and Comparison to Titania–Silica. *J. Catal.* **1996,** *159*, 58-68.

53. Shen, Y., A new hypothesis of micro-region acid sites regarding the surface acidity of binary oxides. *RSC Adv.* **2012,** *2*, 5957-5960.

54. (a) Sandstrom, D. R.; Lytle, F. W.; Wei, P. S. P.; Greegor, R. B.; Wong, J.; Schultz, P., Coordination of titanium in titanium dioxide-silicon dioxide glass by x-ray absorption spectroscopy. *J. Non-Cryst. Solids* **1980,** *41*, 201-7; (b) Evans, D. L., Glass structure: the bridge between the molten and crystalline states. *J. Non-Cryst. Solids* **1982,** *52*, 115-28.

55. (a) Pauling, L., *The nature of the chemical bond and the structure of molecules and crystals*. 3rd ed.; Cornell University Press: Ithaca, New York, 1960; (b) Kataoka, T.; Dumesic, J. A., Acidity of unsupported and silica-supported vanadia, molybdena, and titania as studied by pyridine adsorption. *J. Catal.* **1988,** *112*, 66-79.

56. Gao, X.; Wachs, I. E., Titania–silica as catalysts: molecular structural characteristics and physico-chemical properties. *Catal. Today* **1999,** *51*, 233-254.

57. Alonso, D. M.; Wettstein, S. G.; Dumesic, J. A., Bimetallic catalysts for upgrading of biomass to fuels and chemicals. *Chem. Soc. Rev.* **2012,** *41*, 8075-8098.

58. (a) Sitthisa, S.; An, W.; Resasco, D. E., Selective conversion of furfural to methylfuran over silica-supported NiFe bimetallic catalysts. *J. Catal.* **2011,** *284*, 90-101; (b) Besson, M.; Gallezot, P.; Pinel, C., Conversion of Biomass into Chemicals over Metal Catalysts. *Chem. Rev.* **2013,** *114*, 1827-1870; (c) Lee, J.; Kim, Y. T.;

Huber, G. W., Aqueous-phase hydrogenation and hydrodeoxygenation of biomass-derived oxygenates with bimetallic catalysts. *Green Chem.* **2014,** *16*, 708-718; (d) Chen, L.; Zhu, Y.; Zheng, H.; Zhang, C.; Li, Y., Aqueous-phase hydrodeoxygenation of propanoic acid over the Ru/ZrO$_2$ and Ru–Mo/ZrO$_2$ catalysts. *Appl. Catal., A* **2012,** *411–412*, 95-104; (e) Brands, D. S.; Poels, E. K.; Bliek, A., Ester hydrogenolysis over promoted Cu/SiO$_2$ catalysts. *Appl. Catal., A* **1999,** *184*, 279-289; (f) Sitthisa, S.; Pham, T.; Prasomsri, T.; Sooknoi, T.; Mallinson, R. G.; Resasco, D. E., Conversion of furfural and 2-methylpentanal on Pd/SiO$_2$ and Pd–Cu/SiO$_2$ catalysts. *J. Catal.* **2011,** *280*, 17-27; (g) Kukushkin, R. G.; Bulavchenko, O. A.; Kaichev, V. V.; Yakovlev, V. A., Influence of Mo on catalytic activity of Ni-based catalysts in hydrodeoxygenation of esters. *Appl. Catal., B* **2015,** *163*, 531-538; (h) Yakovlev, V. A.; Khromova, S. A.; Sherstyuk, O. V.; Dundich, V. O.; Ermakov, D. Y.; Novopashina, V. M.; Lebedev, M. Y.; Bulavchenko, O.; Parmon, V. N., Development of new catalytic systems for upgraded bio-fuels production from bio-crude-oil and biodiesel. *Catal. Today* **2009,** *144*, 362-366.

59. Malyala, R. V.; Rode, C. V.; Arai, M.; Hegde, S. G.; Chaudhari, R. V., Activity, selectivity and stability of Ni and bimetallic Ni-Pt supported on zeolite Y catalysts for hydrogenation of acetophenone and its substituted derivatives. *Appl. Catal., A* **2000,** *193*, 71-86.

60. Khromova, S. A.; Smirnov, A. A.; Bulavchenko, O. A.; Saraev, A. A.; Kaichev, V. V.; Reshetnikov, S. I.; Yakovlev, V. A., Anisole hydrodeoxygenation over Ni–Cu bimetallic catalysts: The effect of Ni/Cu ratio on selectivity. *Appl. Catal., A* **2014,** *470*, 261-270.

61. Kitla, A.; Safonova, O. V.; Foettinger, K., Infrared studies on bimetallic copper/nickel catalysts supported on zirconia and ceria/zirconia. *Catal. Lett.* **2013,** *143*, 517-530.

62. Ferrando, R.; Jellinek, J.; Johnston, R. L., Nanoalloys: From Theory to Applications of Alloy Clusters and Nanoparticles. *Chem. Rev.* **2008,** *108*, 845-910.

63. Sankar, M.; Dimitratos, N.; Miedziak, P. J.; Wells, P. P.; Kiely, C. J.; Hutchings, G. J., Designing bimetallic catalysts for a green and sustainable future. *Chem. Soc. Rev.* **2012,** *41*, 8099-8139.

64. Zheng, R.; Humbert, M. P.; Zhu, Y.; Chen, J. G., Low-temperature hydrogenation of the C=O bond of propanal over Ni-Pt bimetallic catalysts: from model surfaces to supported catalysts. *Catal. Sci. Technol.* **2011,** *1*, 638-643.

65. (a) Yan, N.; Zhang, J. In *Nickel based bimetallic catalysts for lignin hydrogenolysis into aromatic chemicals*; American Chemical Society Washington, D.C.: 247th ACS National Meeting & Exposition, Dallas, TX, USA, March 16-20, 2014; (b) Zhang, J.; Asakura, H.; van Rijn, J.; Yang, J.; Duchesne, P.; Zhang, B.; Chen, X.; Zhang, P.;

Saeys, M.; Yan, N., Highly efficient, NiAu-catalyzed hydrogenolysis of lignin into phenolic chemicals. *Green Chem.* **2014,** *16*, 2432-2437.

Chapter 2

Impact of the Oxygen Defects and the Hydrogen Concentration on the Surface of *Tetragonal* and *Monoclinic* ZrO$_2$ on the Reduction Rates of Stearic Acid on Ni/ZrO$_2$

This chapter is based on the following publication:

Three different Ni/ZrO$_2$ catalysts have been tested with regard to their efficiency in the hydrogenation reaction of stearic acid. The Ni/*m*-ZrO$_2$ catalyst was found to be the best one. A higher concentration of active oxygen defects present in this combination was identified to be responsible for the superiority of this catalyst over the other systems.
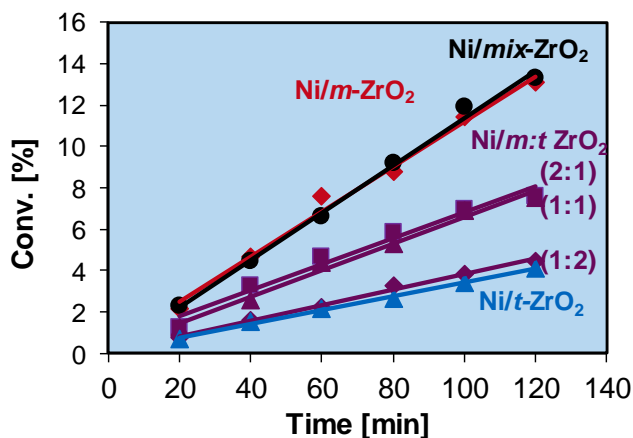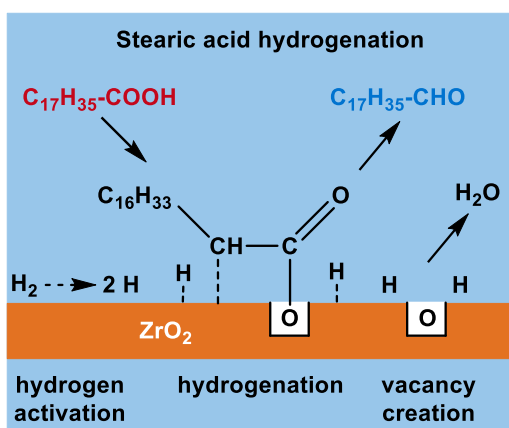
2.1 Abstract

The role of the specific physicochemical properties of ZrO_2 phases on Ni/ZrO_2 has been explored with respect to stearic acid reduction. Conversion on pure *m*-ZrO_2 is 1.3 times more active than on *t*-ZrO_2, while Ni/*m*-ZrO_2 is three times more active than Ni/*t*-ZrO_2. While the hydrodeoxygenation of stearic acid can be catalyzed solely by Ni, the synergistic interaction between Ni and the ZrO_2 support causes the variations in rates. Adsorption of the carboxylic acid group on an oxygen vacancy of ZrO_2 and the abstraction of the α-H with the elimination of the O atom to produce ketene is the key to enhance the overall rate. The hydrogenated intermediate 1-octadecanol is in turn decarbonylated to *n*-heptadecane with identical rates on all catalysts. Decarbonylation of 1-octadecanol is concluded to be limited by the competitive adsorption of reactants and intermediate. The substantially higher adsorption of propionic acid demonstrated by IR spectroscopy and the higher reactivity to O_2 exchange reactions with the more active catalyst indicate that the higher concentration of active oxygen defects on *m*-ZrO_2 compared to *t*-ZrO_2 causes the higher activity of Ni/*m*-ZrO_2.

2.2 Introduction

Microalgae are seen as ideal basis for third-generation biofuels, because of their high growth rates and oil contents as well as the independence of fresh water and arable lands.[1] Their high content of triglycerides makes them a promising resource for liquid transportation fuels. The traditional hydrotreating using sulfided NiMo/Al_2O_3 catalysts has been commercially realized, *i.e.*, the NExBTL process (Neste Oil, Porvoo, 340 kt·a^{-1}).[2] Although the process for hydrotreating of triglycerides can use the existing infrastructure and requires moderate capital investment, the sulfide catalysts are not ideal for the conversion of a nearly sulfur-free triglycerides feedstock, because they deactivate *via* sulfur elimination and contaminate the product stream with organic sulfides.[3]

As sulfur-free supported metal catalysts would be attractive alternatives, two types of novel Ni based catalysts to directly convert crude microalgae oil quantitatively to diesel-range hydrocarbons at mild conditions of 260 °C and 40 bar H_2 were developed.[4] The catalysts used are stable, economic, and scalable. The conversion of the representative model compound stearic acid on Ni/ZrO_2 in presence of H_2 shows that it undergoes reduction of fatty acid solely by Ni and synergistically by Ni and the ZrO_2 support. In the presence of Ni,

the acid is hydrogenated to the aldehyde, followed by decarbonylation of the aldehyde to an alkane. The oxygen vacancies of the ZrO$_2$ support facilitate the concerted adsorption of fatty acid and the activation of H$_2$. The α-H abstraction and elimination of H$_2$O leads to ketene that is formed as a relatively stable intermediate, which has been directly monitored by *in situ* IR spectroscopy.[5] In the following step, the ketene is hydrogenated to the corresponding aldehyde, which is in turn hydrodeoxygenated to the corresponding alkane *via* decarbonylation. The redundancy of the two catalytic sites increases the overall rate.

The best results are obtained by combining an appropriate concentration of the oxygen defect sites with the metal providing the required dissociated hydrogen. It should be noted in passing that much higher rates of the hydrogenation of CO to methanol were observed for Cu/*m*-ZrO$_2$ than for Cu/*t*-ZrO$_2$,[6] the higher apparent first order rate constant for Cu/*m*-ZrO$_2$ than for Cu/*t*-ZrO$_2$ being attributed to the higher concentration of H on the surface of *m*-ZrO$_2$. The difference in the properties of the lattice oxygen of the two ZrO$_2$ phases was speculated to be related to the specific adsorption properties for H and CO. As the properties of oxygen vacancies of supports are critical elements for the hydrodeoxygenation of fatty acids, the effect of *m*-, *t*-, and *mix*- phases of ZrO$_2$ on the hydrodeoxygenation of stearic acid and 1-octadecanol was explored in the liquid phase. The relation between the physicochemical properties of the support, as well as its influence on the properties of the supported Ni particles for catalytic activity and selectivity are explored in the quest to find more active and selective catalysts for fuel synthesis from biomass.

2.3   Results and Discussion

2.3.1   Catalyst characterization

The two phases of *m*- and *t*-ZrO$_2$ were synthesized by the solvothermal method using water and methanol as solvents, respectively. The XRD patterns for the three ZrO$_2$ supports are displayed in the appendix of this chapter (page 49). The diffractogram of *monoclinic* ZrO$_2$ showed the typical characteristic 2 θ reflections at 24.5, 28.3, 31.6, and 34.5° (JCPDS card No. 37-1484). The crystal phase of pure *t*-ZrO$_2$ was confirmed by XRD diffraction peaks at 2 θ of 30.4 and 35.1° (JCPDS card No. 17-0923), without peaks from *m*-ZrO$_2$. Mixed-phase ZrO$_2$ from calcination of Zr(OH)$_4$ showed both, characteristic reflections from

m- and *t*-ZrO_2, and the specific sample consisted of 83% *monoclinic* and 17% *tetragonal* phase as derived from **Equation 2-6** (Experimental Section – Materials and Methods, page 44).

The N_2 sorption showed that the specific BET surface areas of three ZrO_2 supports varied between 117 and 160 $m^2 \cdot g^{-1}$ (**Table 2-1**). After Ni incorporation and further thermal treatment by calcination and reduction, the specific BET surface areas decreased to approximately 70 $m^2 \cdot g^{-1}$ for the three Ni/ZrO_2 catalysts (**Table 2-2**). The concentration of acid and base sites of the parent ZrO_2 and Ni/ZrO_2 were determined from the temperature-programmed desorption (TPD) of NH_3 and CO_2, respectively. The concentrations of Lewis acid and base sites of three ZrO_2 supports were almost identical at 0.30 and 0.04 $m$mol·g^{-1}, respectively. Normalized to the specific surface areas, Lewis acidity and basicity of the supports were 2.0 and 0.3 μmol·m^{-2}, which demonstrates that the acid and base properties are very similar. With Ni deposited, the acid site concentrations of the three Ni/ZrO_2 samples decreased by 50% to 0.11-0.14 $m$mol·g^{-1}, while the concentrations of base sites were almost unchanged (0.04 $m$mol·g^{-1}). This suggests that deposited Ni (metal, oxide or hydroxide) particles interact with and block Lewis acid sites. The surface areas as well as the concentration and strength of acid and base sites for three ZrO_2 and Ni/ZrO_2 samples are shown to be very similar; therefore, the influence from these factors is expected to be minimal.

Table 2-1. Physicochemical properties of ZrO_2 supports.

Support	S_{BET}	Concentration of acid sites [a]		Concentration of basic sites [b]	
	[$m^2 \cdot g^{-1}$]	[$m$mol·g^{-1}]	[μmol·m^{-2}]	[$m$mol·g^{-1}]	[μmol·m^{-2}]
mix-ZrO_2	162	0.33	2.0	0.06	0.37
m-ZrO_2	117	0.30	2.5	0.04	0.36
t-ZrO_2	149	0.30	1.9	0.04	0.27

[a] Determined by TPD of NH_3. [b] Determined by TPD of CO_2.

Table 2-2. Physicochemical properties of Ni incorporated ZrO$_2$ catalysts.

Catalyst	Ni loading [a]	S_{BET}	$d_{Ni(111)}$ [b]	Concentration of acid sites [c]		Concentration of basic sites [d]	
	[wt%]	[m^2·g^{-1}]	[nm]	[mmol·g^{-1}]	[µmol·m^{-2}]	[mmol·g^{-1}]	[µmol·m^{-2}]
Ni/*mix*-ZrO$_2$	9.7	75	12	0.14	1.8	0.05	0.69
Ni/*m*-ZrO$_2$	9.7	69	13	0.11	1.6	0.04	0.58
Ni/*t*-ZrO$_2$	10	70	12	0.11	1.5	0.04	0.54

[a] Determined by Ni-AAS. [b] Calculated from XRD by Scherrer equation. [c] Determined by TPD of NH$_3$. [d] Determined by TPD of CO$_2$.

A) EDX-TEM images

B) Particle size distribution
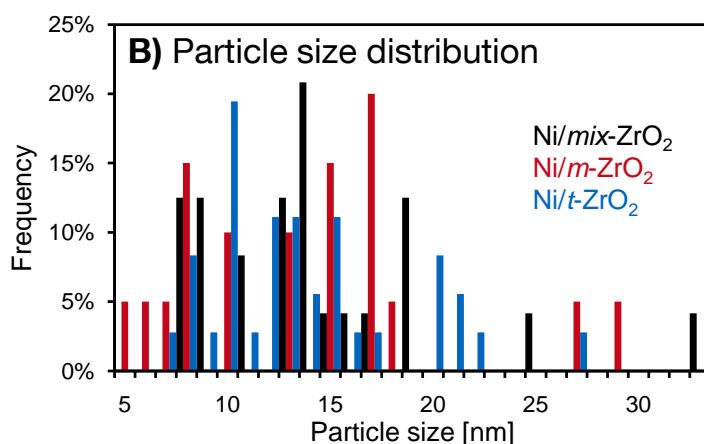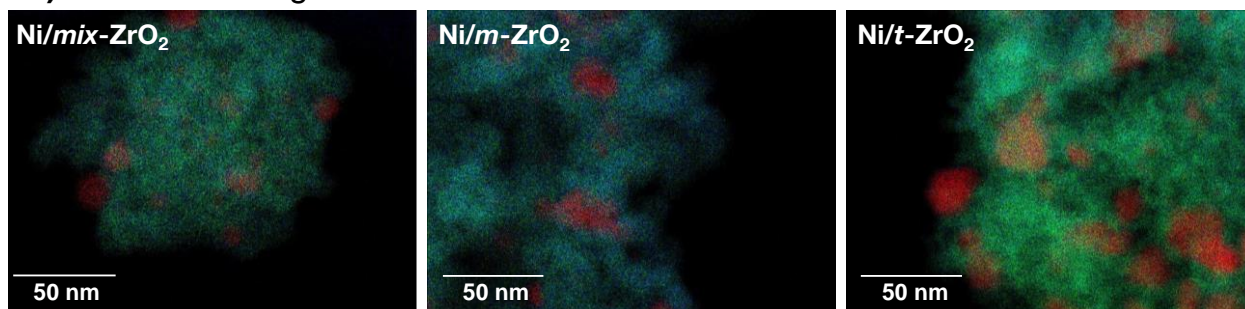
Figure 2-1. A) TEM images with Energy-dispersive X-ray spectroscopy (EDX) mapping (Ni in red, Zr in green, O in blue) and **B)** corresponding Ni particle size distribution of three Ni/ZrO$_2$ catalysts.

The characteristic diffraction peaks for *m*- and *t*-ZrO$_2$ for the three Ni/ZrO$_2$ (**Figure A 2-1, B, Appendix**) samples were in good agreement with the diffractogram of parent supports (**Figure A 2-1, A**), suggesting that the synthesized phases are very stable

against phase transformation during impregnation, calcination, and reduction. The distinctive peaks at 2 θ of 44.6° and 51.9° are assigned to Ni(111) and Ni(200), respectively. Based on the Scherrer equation, the average particle diameter, $d_{Ni(111)}$, of Ni/*mix*-ZrO_2, Ni/*m*-ZrO_2, and Ni/*t*-ZrO_2 were 12, 13, and 12 nm, respectively.

Apart from XRD measurement on determining the Ni-particle size, TEM images with Energy-dispersive X-ray spectroscopy (EDX) mapping of Ni on ZrO_2 (**Figure 2-1, A**) and the corresponding particle size distributions (**Figure 2-1, B**) are also shown. Note that the TEM images of ZrO_2 supported Ni particles are difficult to interpret because of the low metal/support contrast.[7] Therefore, element sensitive EDX-technique was applied to differentiate between metal species and the support. It shows Ni particles in contact with ZrO_2. From TEM micrographs spherically shaped Ni particles with a heterogeneous size distribution, typically for wetness impregnation technique, and an average diameter of 14-15 nm were detected, *i.e.*, larger in size than the average size determined from XRD. This is attributed to the fact that TEM counts the size of visible Ni^0 particles, while XRD accounts also for particles with too low contrast to be determined by TEM measures.[8] Generally, Ni particles show comparable sizes and distributions and shapes on three ZrO_2 supports determined from both XRD patterns and TEM images.
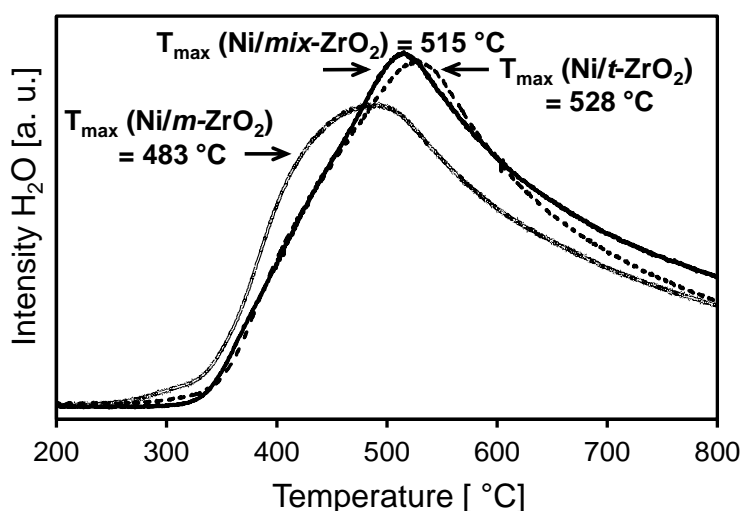
Figure 2-2. Temperature programmed reduction with H_2 on Ni/*mix*-ZrO_2, Ni/*m*-ZrO_2, and Ni/*t*-ZrO_2.

The state of Ni on ZrO$_2$ was probed by TPR of three calcined Ni/ZrO$_2$ catalysts using H$_2$ (**Figure 2-2**). TPR showed that the maximum rates of reduction (monitored by H$_2$O formation) appeared between 483 °C and 528 °C. The maximum reduction rate for Ni/*m*-ZrO$_2$ occurred at 483 °C, whereas for Ni/*mix*-ZrO$_2$ and Ni/*t*-ZrO$_2$, the reduction rates peaked at somewhat higher temperatures, 515 and 528 °C, respectively. Bulk NiO is usually reduced at 400 °C,[9] and the higher temperature observed here is tentatively attributed to the reduction of small nickel oxide crystallites interacting strongly with ZrO$_2$.[8] Reducing the three calcined Ni/ZrO$_2$ catalysts at 500, 550, 600 °C showed that the Ni particles gradually grew as a function of the reduction temperature, leading to particles with 13, 14, and 19 nm diameter, respectively (determined by Scherrer Equation from XRD patterns, **Table A 2-1**). The catalytic activities for stearic acid hydrogenation decreased in the order of 2.6, 2.0, and 1.0 *m*mol·g^{-1}·h^{-1}, indicating that the specific rates of hydrogenation decreased in accordance with the increasing size of the Ni particles. To achieve a high hydrodeoxygenation rate, the calcined Ni/ZrO$_2$ sample were reduced at 500 °C for all samples discussed here.

2.3.2 States of Ni and the ZrO₂ polymorphic phases by XAFS

The states of Ni and Zr in the three different Ni/ZrO$_2$ catalysts are analyzed by Ni- and Zr-K edge XAFS. The Ni K-edge XANES spectra demonstrate that Ni/*m*-ZrO$_2$, Ni/*t*-ZrO$_2$, and Ni/*mix*-ZrO$_2$ catalysts contained a higher concentration of Ni^0 than Ni^{II} (**Figure 2-3, A**). The Fourier transformed Ni K-edge EXAFS spectra were quite similar for the three Ni/ZrO$_2$ catalysts, which is in good agreement with the other results discussed. The fractions of Ni^0 and Ni^{II}, analyzed by a linear combination from XANES, are compiled in **Table A 2-2**. The three Ni/ZrO$_2$ catalysts contained approximately 70-79% metallic Ni^0 and 21-30% Ni^{II} before reaction. The Ni-Ni distances and coordination numbers (**Figure 2-3, B**) are identical to that of bulk Ni. After reaction in presence of H$_2$, the fraction of metallic Ni^0 increased to 84-86%. Fitting the EXAFS using a theoretical standard (**Figure A 2-2**) showed that also for these experiments the coordination number of the first Ni-Ni shell was identical to that for a bulk metal. This is consistent with Ni nanoparticle diameters that are greater than about 5 nm as shown also by TEM (**Figure 2-1, B**). No indication of Ni-Zr scattering, that would be present as a result of a separate, atomically dispersed Ni phase, was observed. The Ni EXAFS structure for Ni/*m*-ZrO$_2$ and for Ni/*t*-ZrO$_2$ were nearly identical up to

R = 8 Å and hence the observed higher reactivity of Ni/*m*-ZrO$_2$ (described below) does not appear to be related to differences in the Ni nanostructures.
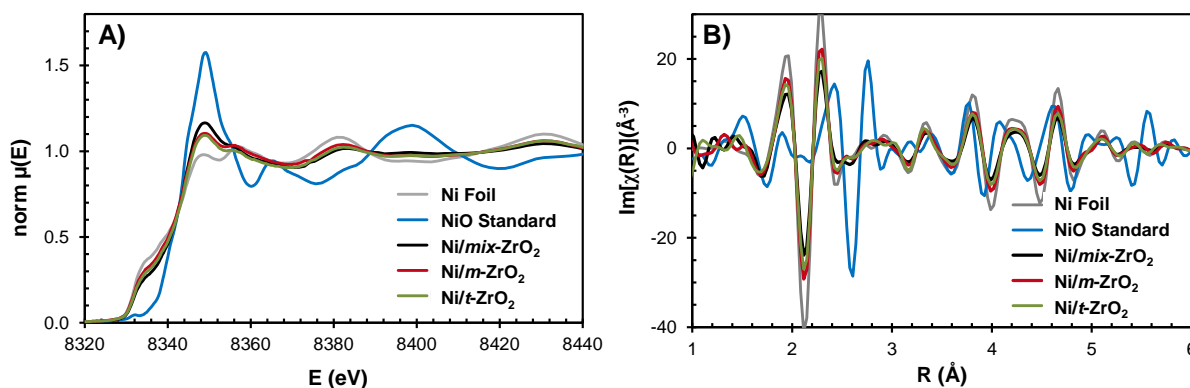
Figure 2-3. **A)** Ni *K*-edge XANES spectra, and **B)** Ni *K*-edge EXAFS Fourier transforms (FTs) Im[χ(R)](Å^{-3}) spectra of Ni-standards (Ni^0 foil, NiO) and Ni/ZrO$_2$ catalysts (Ni/*mix*-ZrO$_2$, Ni/*m*-ZrO$_2$, Ni/*t*-ZrO$_2$) at ambient temperature.

The XAS of the Zr K-edge of the three ZrO$_2$ (**Figure 2-4, A**) shows that the XANES of *mix*-ZrO$_2$, *m*-ZrO$_2$, and *t*-ZrO$_2$ indicate profound differences for *t*-ZrO$_2$ in comparison to *m*-ZrO$_2$ including the stronger 1s → 4d shoulder at 18000 eV, the apparent white line doublet at 18020 eV and the scattering peak at 18045 eV. A more subtle feature is the shoulder on the leading edge of the white line at 18015 eV, which appeared also for the pure *t*-ZrO$_2$. All features are consistent with published values of ZrO$_2$.[10] Using the XANES to differentiate *t*-ZrO$_2$ and *m*-ZrO$_2$, a linear combination fit to the *mix*-ZrO$_2$ yields a ratio of 25% *t*-ZrO$_2$ and 75% *m*-ZrO$_2$ (**Table A 2-3**), which is in good agreement with the XRD results in **Figure A 2-1**. After deposition of Ni, the structure of ZrO$_2$ was hardly changed (**Figure A 2-3**). Calcination and reduction steps, however, alter the ZrO$_2$ phase distribution of *t*-ZrO$_2$ and *mix*-ZrO$_2$. In both instances, *t*-ZrO$_2$ is partially converted to *m*-ZrO$_2$ phase. The *t*-ZrO$_2$ is converted to about 38% *m*-ZrO$_2$ while *mix*-ZrO$_2$ is converted to about 94% *m*-ZrO$_2$.
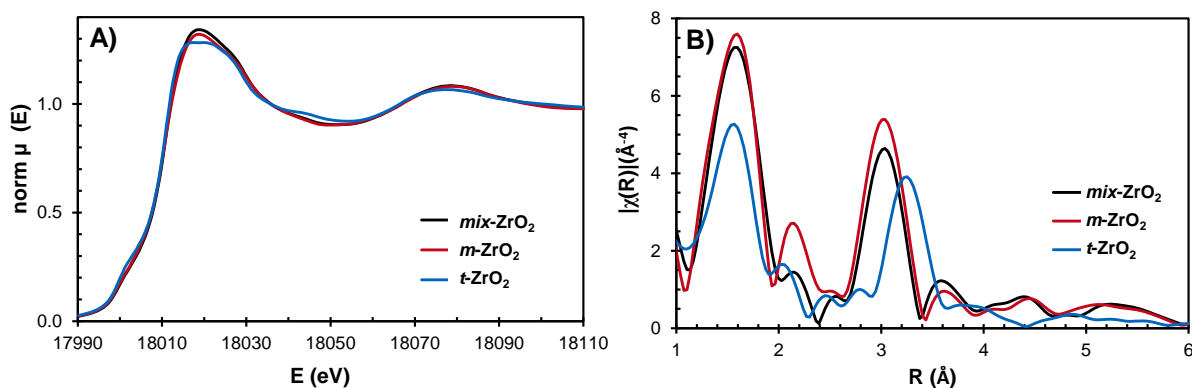
Figure 2-4. **A)** Zr *K*-edge XANES spectra and **B)** Zr *K*-edge EXAFS spectra Fourier transforms
(FTs) Im[χ(R)]($\mathring{A}^{-4}$) spectra of *mix*-ZrO₂, *m*-ZrO₂, and *t*-ZrO₂ at ambient temperature.

In line with the XRD patterns, the Fourier transformed Zr EXAFS (**Figure 2-4, B**)
showed high similarity between *mix*-ZrO₂ and *m*-ZrO₂. The first maximum at 1.5 Å is as-
signed to the nearest shell (O), while the second peak at 3.0-3.3 Å is attributed to the next
nearest shell (Zr) around the Zr central atom.[11] The shift of the peak at 3.3 Å for *t*-ZrO₂
(compared to 3.0 Å for *m*-ZrO₂) in the FT imaginary χ(R) plot (**Figure 2-4, B**) is attributed
to the fact that the Zr-O bond distance is different in *m*-ZrO₂ (Zr-O$_I$, trigonal and Zr-O$_{II}$,
tetrahedral) and *t*-ZrO₂ (Zr-O$_{II}$, tetrahedral).[12] This peak shift from 3.3 to 3.0 Å is also related
to a decreasing symmetry as varying from *tetragonal* to *monoclinic* phase.[11a]

2.3.3   Hydrogenation of stearic acid over ZrO₂

To investigate the effect of ZrO₂ morphologies, stearic acid was converted first on
the bare supports. The three supports led to similar distributions of product after 6 h
(**Figure 2-5, B**). The major products were the aldehyde (selectivity: 60-75%) and dihepta-
decyl ketone (selectivity: 18-27%), as well as small concentrations of *n*-heptadecane
(selectivity: 6-13%).

The reduction and ketonization of the carboxylic acid has been reported to be cata-
lyzed by modestly redox active oxides such as ZrO₂, CeO₂, Cr₂O₃, Fe₂O₃, ZnO, and TiO₂ at
300-400 °C.[13] The catalyzed reaction involves the adsorption of the acid on oxygen defect
sites of the metal oxides to form a carboxylate. The carboxylates are assumed to be adsorbed
parallel to the oxide surface because of the strong interaction of the α-H with the surface.
Ketene and H₂O are formed through abstraction by one of the α-H. Subsequently, a nearby

carboxylate reacts with the activated H (**Scheme 2-1, A**) atoms to form the aldehyde or with
adsorbed ketene to form the ketone by eliminating CO_2 (**Scheme 2-1, B**).
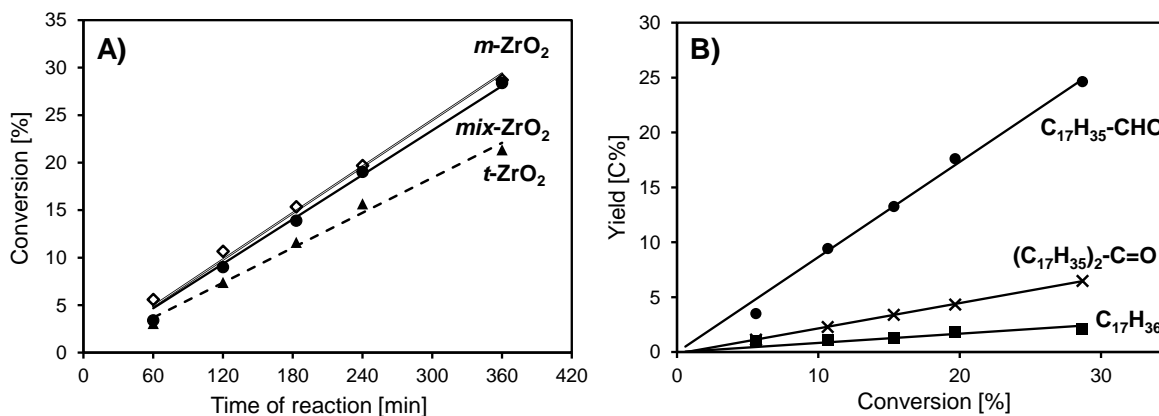
Figure 2-5. A) Conversion of stearic acid over *m*-ZrO_2, *mix*-ZrO_2 and *t*-ZrO_2 as a function of time.
B) Yields of octadecanal, diheptadecyl ketone, and *n*-heptadecane over *m*-ZrO_2 as a function of
stearic acid conversion. Reaction conditions: stearic acid (0.5 g), ZrO_2 (0.5 g), dodecane (100 mL),
260 °C, $p(H_2) = 40$ bar, stirring at 600 rpm. Reproducibility of the rates has been better than ± 5%.
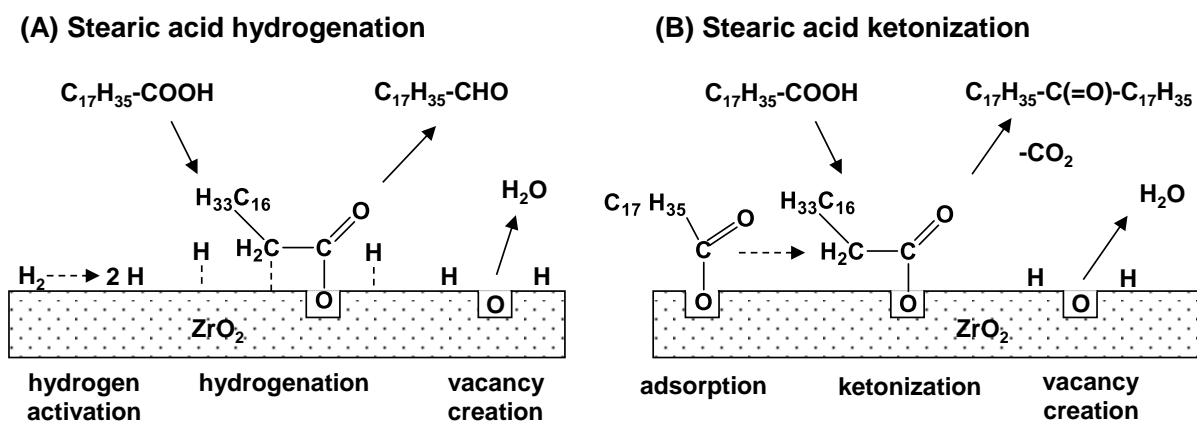
Scheme 2-1. Mechanisms for (**A**) hydrogenation and (**B**) ketonization of stearic acid on the surface
of ZrO_2.

The rates of stearic acid conversion on *mix*- and *m*-ZrO_2 were similar at 28% and
29% after 6 h corresponding to rates of 0.017 and 0.016 $m$mol·g^{-1}·h^{-1}, respectively. The rate
on *t*-ZrO_2 was 20% lower (**Table 2-3**). The *mix*-ZrO_2 consisted of a majority of 83% *m*-ZrO_2
evidenced by the XRD patterns. This demonstrates that the *monoclinic* phase of ZrO_2 is more
active for stearic acid reduction even in the absence of metal sites.

Table 2-3. Comparison of stearic acid conversion over ZrO_2 supports.[a]

Catalyst	Rate	Conv.	Selectivity [C%]		
	[$m$mol·g^{-1}·h^{-1}]	[%]	C_{17}	C_{17}-CHO	$(C_{17}H_{35})_2$C=O
mix-ZrO_2	0.017	28	13	60	27
m-ZrO_2	0.016	29	6.9	75	18
t-ZrO_2	0.013	21	6.0	72	22

[a] Reaction conditions: stearic acid (0.5 g), ZrO_2 (0.5 g), dodecane (100 mL), 260 °C, $p(H_2)$ = 40 bar, 6 h, stirring at 600 rpm. Reproducibility of the rates has been better than ± 5%.

2.3.4 Hydrogenation of stearic acid with Ni/ZrO_2

The results of the conversion of stearic acid on Ni supported on *m*-, *t*-, and *mix*-ZrO_2 are shown in **Figure A 2-4, A**. The primary initial product was the hydrogenated alcohol with a selectivity of 86-94%, and further decarbonylated C_{17} and hydrodeoxygenated C_{18} hydrocarbons were obtained in minor quantities (total selectivity: 5-10%) (**Figure A 2-4, B**). With Ni/ZrO_2 ketonization was eliminated. In addition, the hydrogenation rate on Ni/*m*-ZrO_2 (2.6 $m$mol·g^{-1}·h^{-1}) was two orders of magnitude higher than that on *m*-ZrO_2 (0.017 $m$mol·g^{-1}·h^{-1}). This is attributed to the fact that Ni aided the dissociation of H_2, dramatically enhancing the rate of formation and consequently increasing the number of oxygen vacancies on the ZrO_2 support, thereby substantially increasing the rate of ketene formation by the support. Additionally, in presence of H_2, the direct Ni catalyzed hydrogenation of stearic acid dominates the overall catalytic chemistry. The facile availability of H essentially eliminates the much slower ketonization route.

Comparison of the three different Ni/ZrO_2 catalysts shows that the rate of conversion of stearic acid over Ni/*m*-ZrO_2 (2.6 $m$mol·g^{-1}·h^{-1}) was almost three times higher than that over Ni/*t*-ZrO_2 (0.9 $m$mol·g^{-1}·h^{-1}) (**Table 2-4**). The catalytic activities of Ni/*mix*-ZrO_2 and Ni/*m*-ZrO_2 for producing 1-octadecanol were quite similar with rates of 2.5 and 2.6 $m$mol·g^{-1}·h^{-1}, respectively. To further verify such a phase effect, Ni supported on physical mixtures of *m*-ZrO_2 and *t*-ZrO_2 (**Figure A 2-4, A**) were used to reduce stearic acid under otherwise identical conditions. The hydrogenation rates followed the sequence of 1.7, 1.5, and 1.0 $m$mol·g^{-1}·h^{-1} for the 1:2, 1:1, and 2:1 ratios of and Ni/*m:t*-ZrO_2 samples (**Table 2-4**).

The rates with the physically mixed supports were expectedly between the rates of pure Ni/m-ZrO_2 (2.6 $m$mol·g^{-1}·h^{-1}) and Ni/t-ZrO_2 samples (0.9 $m$mol·g^{-1}·h^{-1}). These results show that the rate of reduction is directly correlated with the concentration of m-ZrO_2 (**Figure 2-6**).

Table 2-4. Comparison of stearic acid conversion over different Ni/ZrO_2 catalysts.[a]

Catalyst	Rate	Conv.	Selectivity [C%]		
	[$m$mol·g^{-1}·h^{-1}]	[%]	C_{17}	C_{18}	C_{18}-OH
Ni/*mix*-ZrO_2	2.5	13.3	5.5	0.4	94
Ni/m-ZrO_2	2.6	12.7	6.3	0.5	93
Ni/2:1 *m:t*-ZrO_2	1.7	7.1	11	2.0	87
Ni/1:1 *m:t*-ZrO_2	1.5	7.3	9.4	1.6	89
Ni/1:2 *m:t*-ZrO_2	1.0	4.4	12	2.0	86
Ni/t-ZrO_2	0.9	4.1	7.8	0.2	92

[a] Reaction conditions: stearic acid (1.0 g), Ni/ZrO_2 (10 wt%, 0.10 g), dodecane (100 mL), 260 °C, $p(H_2)$ = 40 bar, 2 h, stirring at 600 rpm. Reproducibility of the rates has been better than ± 5%.
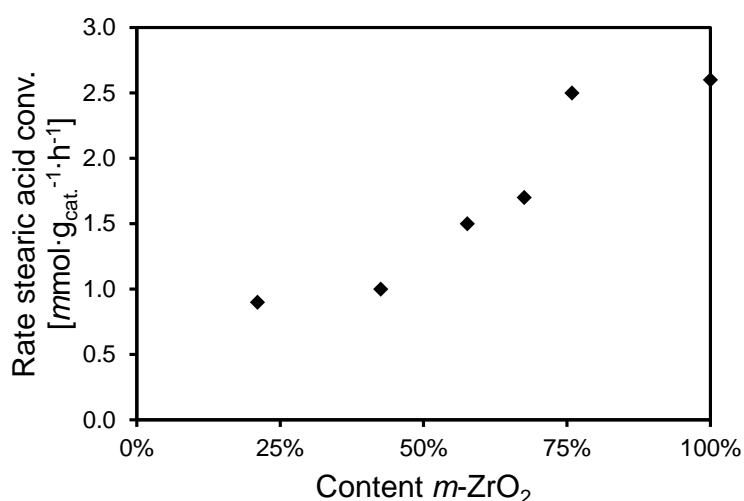
Figure 2-6. Rates for the conversion of stearic acid depending on the content of *monoclinic* ZrO_2 in a Ni/ZrO_2 catalyst. Reaction conditions: stearic acid (1.0 g), Ni/ZrO_2 (10 wt%, 0.1 g), dodecane (100 mL), 260 °C, $p(H_2)$ = 40 bar, stirring at 600 rpm.

2.3.5 Decarbonylation of 1-octadecanol over Ni/ZrO$_2$

The hydrodeoxygenation of stearic acid on Ni/ZrO$_2$ proceeded with hydrogenation to 1-octadecanol as the apparent primary product (**Figure A 2-4, B**). To better understand the kinetic sequence, 1-octadecanol conversion was studied in separate experiments (**Figure 2-7**). Selectivities of 95% *n*-heptadecane (C$_{17}$) and 5% *n*-octadecane (C$_{18}$) were observed at 36% conversion after 2 h for all samples. This shows that direct decarbonylation (-CO) of the aldehyde, formed *via* the dehydrogenation of the alcohol took place. The minor concentration of *n*-octadecane is concluded to be catalyzed by the sequential dehydration-hydrogenation of the alcohol on acid sites of Ni/ZrO$_2$. The rate of decarbonylation of 1-octadecanol (6.3 $m$mol·g^{-1}·h^{-1}) was identical on all Ni/ZrO$_2$ catalysts (**Figure 2-7** and **Table 2-5**), and such rate was 3-7 times higher than that of stearic acid hydrogenation (2.6 and 0.9 $m$mol·g^{-1}·h^{-1}) on Ni/*m*-ZrO$_2$ and Ni/*t*-ZrO$_2$ catalysts. This suggests that the rate-determining step is related to the reductive deoxygenation of the fatty acid. The result also implies that the decarbonylation of 1-octadecanol is not sensitive with respect to the ZrO$_2$ phases, and that the active sites of Ni particles convert 1-octadecanol with identical rates.
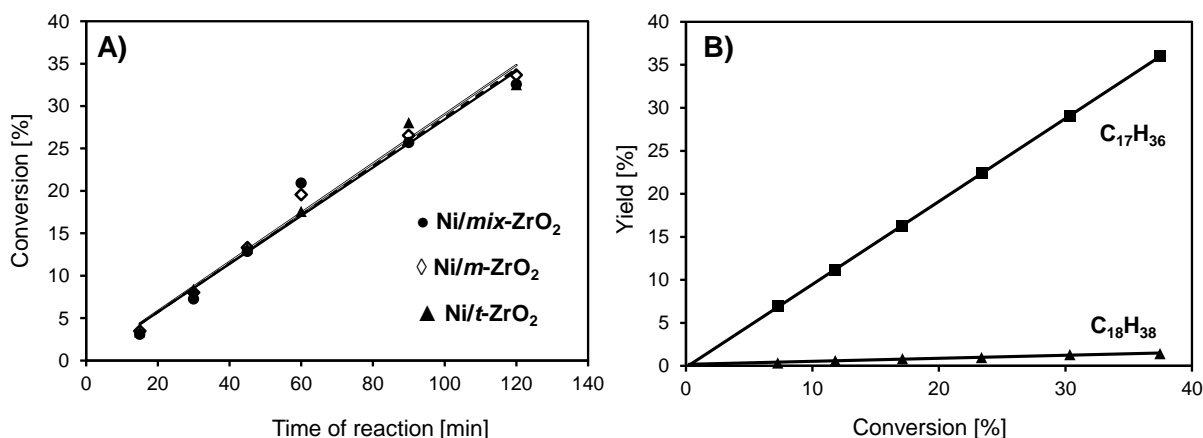
Figure 2-7. A) Conversion of 1-octadecanol as a function of time. **B)** Yield of *n*-heptadecane and *n*-octadecane over Ni/*m*-ZrO$_2$ as a function of 1-octadecanol conversion. Reaction conditions: 1-octadecanol (1.0 g), Ni/ZrO$_2$ (10 wt%, 0.10 g), dodecane (100 mL), 260 °C, p(H$_2$) = 40 bar, stirring at 600 rpm. Reproducibility of the rates has been better than ± 5%.

Table 2-5. Comparison of 1-octadecanol conversion over three Ni/ZrO_2 catalysts.[a]

Catalyst	Rate	Conv.	Selectivity [C%]	
	[$m$mol·g^{-1}·h^{-1}]	[%]	C$_{17}$	C$_{18}$
Ni/*mix*-ZrO_2	6.3	33	95	5.0
Ni/*m*-ZrO_2	6.3	33	96	4.0
Ni/*t*-ZrO_2	6.2	32	97	3.0

[a] Reaction conditions: 1-octadecanol (1.0 g), Ni/ZrO_2 (10 wt%, 0.10 g), dodecane (100 mL), 260 °C, p(H$_2$) = 40 bar, 2 h, stirring at 600 rpm. Reproducibility of the rates has been better than ± 5%.

2.3.6 Overall hydrodeoxygenation of stearic acid to *n*-heptadecane over Ni/ZrO_2

The kinetics of overall hydrodeoxygenation of stearic acid to *n*-heptadecane over Ni/*m*-ZrO_2 and Ni/*t*-ZrO_2 at 260 °C is shown in **Figure 2-8**. 1-Octadecanol is the initial product, being formed in yields of 60-80%, although the final product is primarily *n*-heptadecane. Octadecanal and 1-octadecanol being in equilibrium *via* facile Ni-catalyzed hydrogenation/dehydrogenation reactions account for this conversion of 1-octadecanol to *n*-heptadecane. At the high H$_2$ pressure (40 bar), the concentration of aldehyde is too low to be observed. Nevertheless, the intermediate octadecanal is slowly and irreversibly decarbonylated to *n*-heptadecane, effectively converting 1-octadecanol into *n*-heptadecane. 1-Octadecanol also underwent esterification with stearic acid to form stearyl stearate (reversible reaction) as well as dehydration/hydrogenation to *n*-octadecane as side-products. Ni/*m*-ZrO_2 achieved a much higher rate for reduction of stearic acid forming 1-octadecanol as well as overall hydrodeoxygenation rates for producing *n*-heptadecane from stearic acid (**Figure 2-8**), which is fitted with the results from kinetic measurements of individual steps.
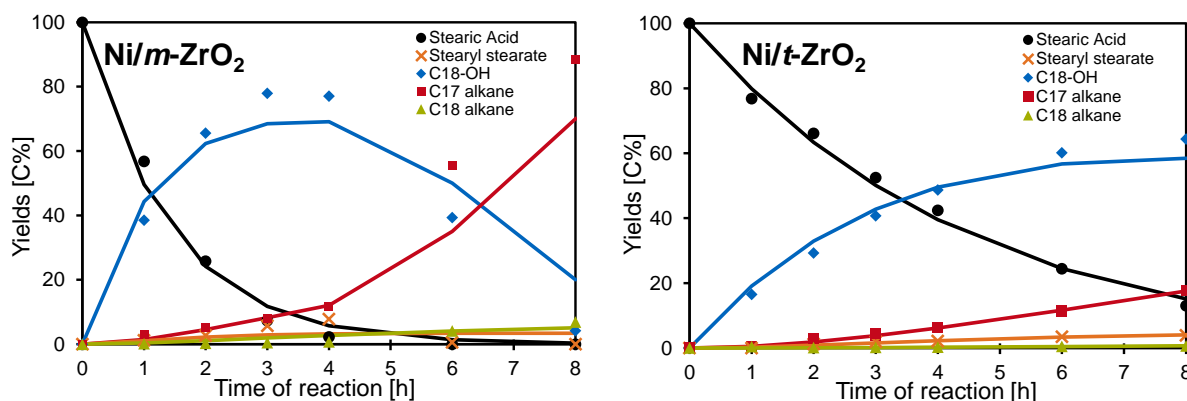
Figure 2-8. Fitting data for hydrodeoxygenation of stearic acid using Ni/*m*-ZrO$_2$ and Ni/*t*-ZrO$_2$ as a function of time (solid point: experimental data, line: fitted data). Reaction conditions: stearic acid (0.5 g), Ni/ZrO$_2$ (10 wt%, 0.2 g), dodecane (100 mL), 260 °C, *p*(H$_2$) = 40 bar, stirring at 600 rpm.
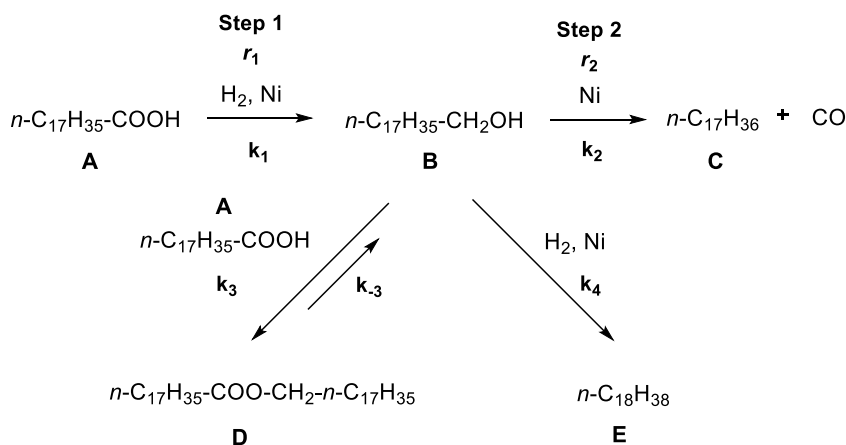
Scheme 2-2. Proposed elementary steps for hydrodeoxygenation of stearic acid to *n*-heptadecane (C$_{17}$).

     A simplified network for hydrodeoxygenation of stearic acid over Ni/ZrO$_2$ catalysts is displayed in **Scheme 2-2**. The elementary steps include hydrogenation of stearic acid (A) to 1-octadecanol (B), then 1-octadecanol (B) is decarbonylated to *n*-heptadecane (C). In addition, dehydration/hydrogenation of 1-octadecanol (B) forms *n*-octadecane without carbon loss, and esterification of stearic acid (A) and 1-octadecanol (B) produces stearyl stearate ester (D). The latter esterification reaction is in equilibrium. The H$_2$ partial pressure before and after reaction was 40 bar. Assuming first-order reaction steps, the elementary rate equations are listed as follows (**Equation 2-1** to **Equation 2-5**):

Equation 2-1

$$\frac{dc(A)}{dt} = -k_1 c(A) - k_3 c(A) c(B) + k_{-3} c(D)$$

Equation 2-2

$$\frac{dc(B)}{dt} = k_1 c(A) - k_2 c(B) - k_3 c(B) c(A) + k_{-3} c(D) - k_4 c(B)$$

Equation 2-3

$$\frac{dc(C)}{dt} = k_2 c(B)$$

Equation 2-4

$$\frac{dc(D)}{dt} = k_3 c(A) c(B) - k_{-3} c(D)$$

Equation 2-5

$$\frac{dc(E)}{dt} = k_4 c(B)$$

The rate **Equation 2-1** to **Equation 2-5** were numerically integrated and fit by least squares to the kinetic data for hydrodeoxygenation of stearic acid over Ni/*m*-ZrO_2 and Ni/*t*-ZrO_2 (**Figure 2-8**). The fitted rate constant ($k_1 = 2.7 \times 10^{-3}$ min^{-1}) for stearic acid hydrogenation over Ni/*m*-ZrO_2 was almost identical to the value ($k_1 = 2.2 \times 10^{-3}$ min^{-1}) from individual reaction step measurement (**Table 2-6**). However, the reaction rates for alcohol decarbonylation were not consistent between the fitted data ($k_2 = 2.4 \times 10^{-4}$ min^{-1}) and calculated individual measurement ($k_2 = 7.5 \times 10^{-3}$ min^{-1}). The rate constants of the side-reactions k_3 ($k_3 = 5.0 \times 10^{-6}$ min^{-1}) for esterification as well as k_4 for dehydration/hydrogenation towards *n*-octadecane ($k_4 = 1.2 \times 10^{-5}$ min^{-1}) were two orders of magnitude lower than k_1 ($k_1 = 2.7 \times 10^{-3}$ min^{-1}). The substantially lower rate constant k_2 in the fitted overall hydrodeoxygenation is attributed to either competition of stearic acid and 1-octadecanol in the conversion (major part), or to side reactions such as esterification and dehydration of 1-octadecanol (a very minor part). Meanwhile, the apparent esterification rate constant k_3 (5.0×10^{-6} min^{-1}) was five magnitudes higher than its reverse rate k_{-3} (1.9×10^{-11} min^{-1}). Therefore, the forward reaction of esterification is concluded to be more favored in the tested time period. Note that as 1-octadecanol and stearic acid are consumed continuously along the reaction time, the equilibrium would be shifted to the reverse reaction for cleavage the C−O bond of stearyl stearate. Compared to Ni/*m*-ZrO_2 ($k_1 = 2.7 \times 10^{-3}$ min^{-1}), Ni/*t*-ZrO_2 showed

three times lower hydrogenation rate ($k_1 = 9.2 \times 10^{-4}$ min^{-1}) for hydrogenation of stearic acid (**Table 2-6, B**), which was identical to the rate comparison in the individual steps measurement (**Table 2-6, A**). The rate of 1-octadecanol decarbonylation on Ni/*t*-ZrO$_2$ ($k_2 = 2.1 \times 10^{-4}$ min^{-1}) was identical to that on Ni/*m*-ZrO$_2$ ($k_2 = 2.4 \times 10^{-4}$ min^{-1}) in the overall hydrodeoxygenation of stearic acid (**Table 2-6, B**), which is in agreement with the rate comparison in the individual measurements ($k_2 = 7.4$ and 7.5×10^{-3} min^{-1}, respectively, **Table 2-6, A**). The lower rate of 1-octadecanol decarbonylation in the overall hydrodeoxygenation process compared to individual steps is majorly attributed to the competition in species adsorption with stearic acid onto the active Ni sites. For the reversible esterification (k_3 and k_{-3}) and dehydration (k_4) of 1-octadecanol, the rates were comparable on Ni/*m*-ZrO$_2$ and Ni/*t*-ZrO$_2$ catalysts (**Table 2-6, B**) probably because of their similar acidity and basicity. In addition, the rate constants of the side reactions (k_3, k_{-3}, and k_4) were magnitudes lower than the major reaction steps of stearic acid hydrogenation (k_1) and decarbonylation of 1-octadecanol (k_2), implying the influence of side reactions is minimal compared to the overall hydrodeoxygenation.

Table 2-6. A) Rate constants in the individual steps and **B)** fitted rate constants in the overall hydrodeoxygenation of stearic acid with Ni/*m*-ZrO$_2$ and Ni/*t*-ZrO$_2$ (normalized to conditions: stearic acid 1.0 g, catalyst 0.1 g, 260 °C, $p(H_2) = 40$ bar, stirring at 600 rpm).

A) Rate constants determined from individual steps

Catalyst	**Step 1**: Hydrogenation of stearic acid	**Step 2**: Decarbonylation/ hydrogenation of 1-octadecanol
	$r_1 = k_1\, c(C_{17}H_{35}COOH)$	$r_2 = k_2\, c(C_{17}H_{35}\text{-}CH_2OH)$
Ni/*m*-ZrO$_2$	$k_1 = 2.2 \times 10^{-3}$ min^{-1}	$k_2 = 7.5 \times 10^{-3}$ min^{-1}
Ni/*t*-ZrO$_2$	$k_1 = 7.9 \times 10^{-4}$ min^{-1}	$k_2 = 7.4 \times 10^{-3}$ min^{-1}

B) Fitted rate constants in the overall hydrodeoxygenation of stearic acid

	k_1 (min^{-1})	k_2 (min^{-1})	k_3 (min^{-1})	k_{-3} (min^{-1})	k_4 (min^{-1})
Ni/*m*-ZrO$_2$	2.7×10^{-3}	2.4×10^{-4}	5.0×10^{-6}	1.9×10^{-11}	1.2×10^{-5}
Ni/*t*-ZrO$_2$	9.2×10^{-4}	2.1×10^{-4}	1.5×10^{-6}	2.9×10^{-11}	8.5×10^{-6}

The mechanism for hydrodeoxygenation of stearic acid proceeds *via* two routes. The first relies on the Ni catalyzed reductive deoxygenation to octadecanal, which is equilibrated with 1-octadecanol. The aldehyde is in turn decarbonylated on Ni. The second pathway starts with the adsorption of stearic acid on the oxygen vacancies of ZrO$_2$ to form the carboxylate, and then through deoxygenation to aldehyde. The reductive deoxygenation on pure ZrO$_2$ support is quite low (0.016 $m$mol·g^{-1}·h^{-1}) presumably because H$_2$ dissociation – required to maintain oxygen vacancies through desorption of water – is slow (the HD formation, characteristic for H$_2$ dissociation was at least 10^2 times faster in presence of Ni than with ZrO$_2$ alone). The redundant catalytic pathways of Ni and ZrO$_2$ generate the appropriate combination enhancing the hydrogenation rate of stearic acid by 150 times (2.6 $m$mol·g^{-1}·h^{-1}) compared to m-ZrO$_2$ (0.016 $m$mol·g^{-1}·h^{-1}). The rate on Ni/ZrO$_2$ is much higher than that on other Ni based catalysts such as Ni/C, Ni/Al$_2$O$_3$, and Ni/SiO$_2$,[5] suggesting a strong support effect. In summary, it can be concluded that the major active sites are the Ni particles. The Ni particles on m- and t-ZrO$_2$ supports have been shown to be almost identical by TEM, XRD, TPR, EXAFS, and XANES, as well as by the rates of decarbonylation of 1-octadecanol. It should be emphasized at this point that the BET surface areas, the concentrations of acid and base sites on parent m- and t-ZrO$_2$ and Ni/ZrO$_2$ were nearly identical. Therefore, the rate differences of stearic acid hydrodeoxygenation on Ni/m-ZrO$_2$ and Ni/t-ZrO$_2$ are concluded to be related to differences in the adsorption and/or redox properties. These properties will be explored by spectroscopically characterizing variations in the sorption mode and strength of propionic acid as well as with the temperature programmed isotopic exchange (^{18}O-^{16}O) of m- and t-phases of ZrO$_2$.

2.3.7 Comparison of in situ IR spectroscopy of adsorbed propionic acid on *m*- and *t*-ZrO$_2$ in the gas phase

The IR spectra of free propionic acid in the gas phase and adsorbed propionic acid on m-ZrO$_2$ are shown in **Figure 2-9**. The absorbance bands at 3600-3700 cm^{-1} for propionic acid in the gas phase (**Table A 2-4**) are ascribed to the O−H stretching vibration of the carboxylic acid group. The C=O vibration of the carboxylic acid group is assigned to the doublet at 1700 and 1800 cm^{-1} and the C−O vibration to the band at 1150 cm^{-1}. The C−H stretching vibrations of −CH$_3$ and –CH$_2$ are assigned to the bands at 2945 and 2986 cm^{-1}. The in-plane bending vibration of C−H are assigned to the triplet bands between 1400-

1500 cm^{-1} and at 1080 cm^{-1}. When the carboxylic group of the propionic acid was adsorbed on the ZrO$_2$ surface, the ν(O−H) disappeared and the C=O vibrations at 1700-1800 cm^{-1} became indistinguishable. This is a primary indication that propionic acid adsorbs on the catalyst surface as bidentate *via* the carboxylic group (**Figure 2-10**).
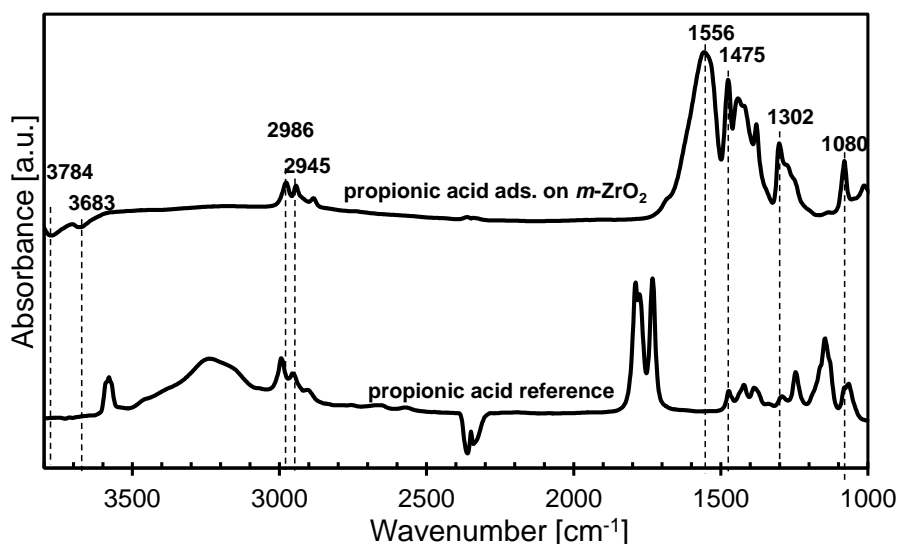
Figure 2-9. IR spectra of propionic acid (0.05 *m*bar) adsorbed on *m*-ZrO$_2$ at 40 °C and free propionic acid in vapor phase as reference.
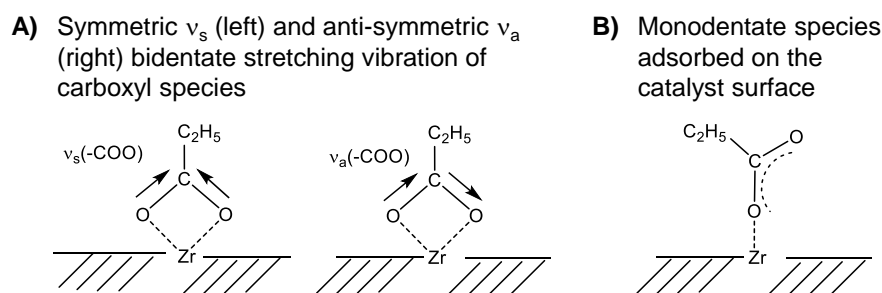
Figure 2-10. Adsorbed carboxyl species in **A)** bidentate and **B)** monodentate conformation on the surface of ZrO$_2$.

The bands at 1556 and 1419 cm^{-1} are attributed to the O−C−O anti-symmetric (ν_a) and symmetric (ν_s) vibrations (**Figure 2-10, A**), which suggest the presence of a symmetric bidentate species with two indistinguishable O atoms. The band at 1419 cm^{-1} (symmetric ν_s vibrations) may overlap with the more intense ν-CH$_3$ vibration as part of the C−H triplet

(1400-1500 cm^{-1}).[13c, 13d, 14] The bands for C−H vibrations remained unchanged at 2986 and 2945 cm^{-1} as well as the vibrations of triplet (1400-1500 cm^{-1}) and ν-CH$_3$ (1080 cm^{-1}). This leads to the conclusion that when propionic acid is adsorbed on ZrO$_2$, the C=O vibrations at 1800 and 1700 cm^{-1} and the C−O vibration at 1150 cm^{-1} in free propionic acid disappear due to the formation of a surface carboxylate (**Figure 2-10, A**).

Figure 2-11 shows the IR spectra of propionic acid adsorbed on *m*-ZrO$_2$ and *t*-ZrO$_2$ at partial pressures 0.02-0.05 *m*bar and temperatures of 100-250 °C. The spectra are obtained by subtracting the activated ZrO$_2$ sample. With increasing pressure of propionic acid at 40 °C, the intensity of the characteristic bands on *m*-ZrO$_2$ (ν$_a$, ν$_s$, ν$_{C-H}$, δ-CH$_3$, ρ-CH$_3$) increased (**Figure 2-11, A**), while the intensity of the ZrO−H vibration decreased. The concentration of Zr−OH groups on the surface decreased as the acid adsorbed on the ZrO$_2$ surface. At the highest dosing pressure of 0.05 *m*bar, the peak at 1556 cm^{-1} of propionic acid was split into two bands at 1583 and 1525 cm^{-1}. This suggests that propionate partially adsorbs in a monodentate configuration (**Figure 2-10, B**) which is characterized by a much larger splitting of the ν$_a$(COO) and ν$_s$(COO) carboxylate stretching frequencies.[15] These adsorbate molecules are competing for the active sites of ZrO$_2$, monodentate dominates over bidentate at high pressures due to its lower space requirement. Near the reaction temperature of 250 °C (**Figure 2-11, B**), only ν$_a$(COO) and ν$_s$(COO) decreased markedly in intensity. At the elevated temperatures, more molecules were desorbed, lessening the surface coverage and competition by carboxylic acid for the actives sites (*i.e.* oxygen vacancies). Accordingly, the splitting and difference of symmetric and asymmetric carboxylate stretching frequencies decreased, consistent with the bidentate configuration being dominant over the monodentate one. For propionic acid adsorbing on *t*-ZrO$_2$, principally the same species and vibration bands were observed. On increasing the pressure of propionic acid to 0.05 *m*bar at 40 °C (**Figure 2-11, C**), the intensity of the characteristic bands increased, indicating an increasing amounts of adsorbed molecules. Increasing the temperature caused the concentration of adsorbate to decrease (**Figure 2-11, D**).

The Ni/*m*-ZrO$_2$ and Ni/*t*-ZrO$_2$ catalysts showed the same trend upon adsorption of propionic acid as the bare supports, but the concentrations of adsorbed propionic acid was lower (**Figure A 2-5, A-D**). This is consistent with observations that the lower BET surface areas as well as the concentrations of acid sites for Ni/ZrO$_2$ are lower in comparison to the

bare ZrO_2 supports. The concentration of propionic acid adsorbed on the ZrO_2 and Ni/ZrO_2 catalyst surface was quantified *via* the peak area at 1080 cm^{-1} ($\rho(CH_3)$). As shown in **Figure 2-12**, the coverage of propionic acid was generally much higher for the bare ZrO_2 supports than Ni/ZrO_2 samples. The adsorbed amount increased linearly as a function of the partial pressure of propionic acid from 0.02 to 0.05 *m*bar (**Figure 2-12, A**). The results also suggest that *m*-ZrO_2 adsorbed 1.5 times more propionic acid than *t*-ZrO_2 at 0.05 *m*bar and 40 °C, which in both cases expectedly decreased exponentially with temperature (**Figure 2-12, B**). The amount of propionic acid adsorbed on *m*-ZrO_2 and Ni/*m*-ZrO_2 was always more than that on *t*-ZrO_2 and Ni/*t*-ZrO_2, respectively. Due to this higher coverage and surface concentration, *m*-ZrO_2 is concluded to be the more active support for converting stearic acid, because the reaction order is positive in the reactant concentration. This is in good agreement with the experimental results above showing *m*-ZrO_2 to have the higher activity than *t*-ZrO_2.
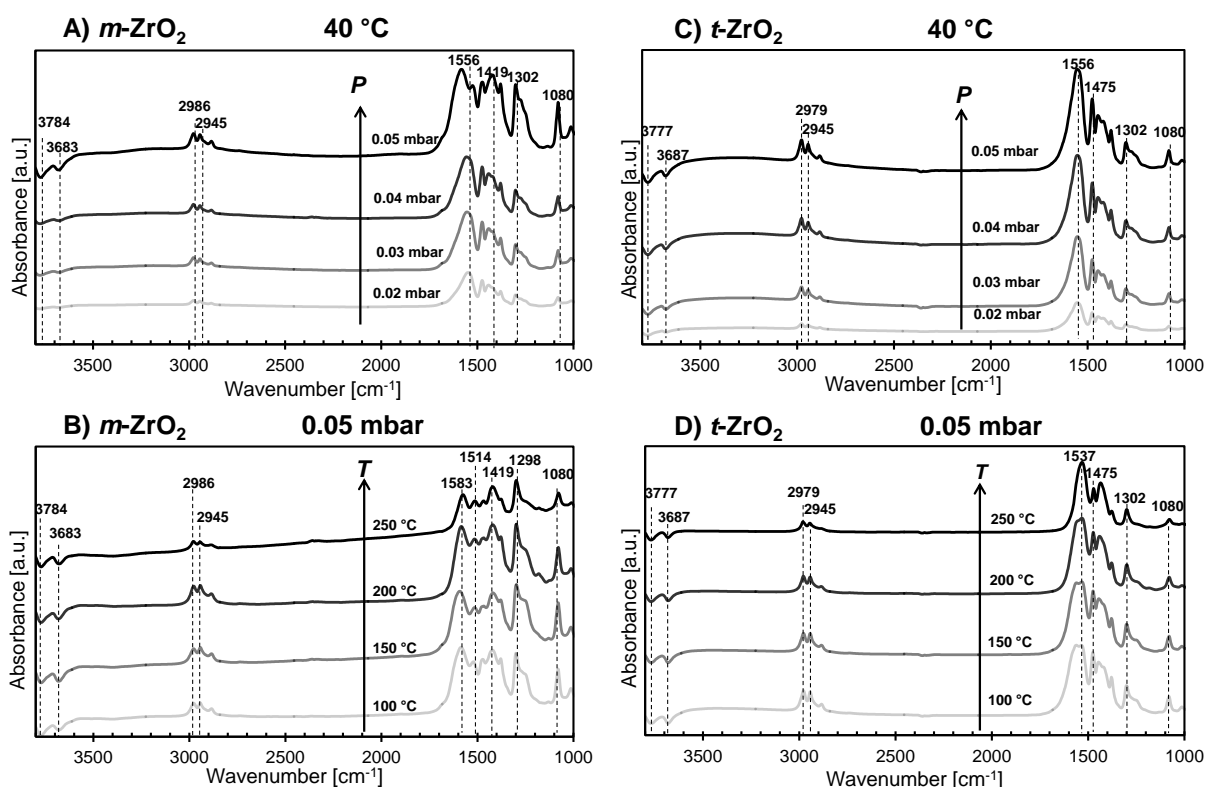
Figure 2-11. IR spectra of adsorbed propionic acid on *m*-ZrO_2 and *t*-ZrO_2, (**A** and **C**) with increasing pressures from 0.02 to 0.05 *m*bar at 40 °C, and (**B** and **D**) with increasing temperatures from 100 °C to 250 °C at 0.05 *m*bar pressure.
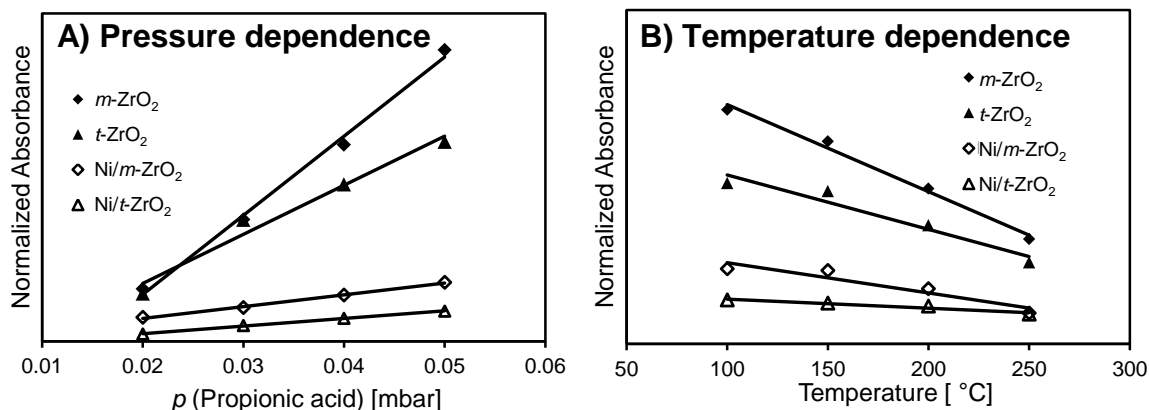
Figure 2-12. Adsorption of propionic acid on *m*-ZrO$_2$, *t*-ZrO$_2$, Ni/*m*-ZrO$_2$, and Ni/*t*-ZrO$_2$ as a function of **A)** partial pressure, and **B)** temperature determined by IR spectroscopy, shown as specific amount (peak area at $\nu = 1080$ cm^{-1}) normalized by specimen mass.

2.3.8 Temperature programmed isotopic exchange (^{16}O-^{18}O) of *m*- and *t*-ZrO$_2$

Figure 2-13 shows the TPIE profiles for *m*-ZrO$_2$ and *t*-ZrO$_2$, respectively, where the mol% of ^{16}O$_2$ (M32), ^{18}O-^{16}O (M34), and ^{18}O$_2$ (M36) are presented as a function of temperature. The signal of ^{18}O$_2$ with *m*-ZrO$_2$ (**Figure 2-13, A**) decreased from 2.5 to 1.0 mol%. This conversion on *m*-ZrO$_2$ is obviously much faster compared to *t*-ZrO$_2$ (**Figure 2-13, B**), which showed a small decrease of the ^{18}O$_2$ signal from 2.5-2.0 mol%. Consistent with this, the concentration of ^{18}O^{16}O increased much faster with *m*-ZrO$_2$. The consumption and exchange of ^{18}O$_2$ (M36) at *m*-ZrO$_2$ ($\Delta = 1.5$ mol%) was three times higher than on *t*-ZrO$_2$ ($\Delta = 0.5$ mol%), which parallels the difference in rates of stearic acid conversion on Ni/*m*-ZrO$_2$ and on Ni/*t*-ZrO$_2$. In summary, *m*-ZrO$_2$ shows higher activity towards ^{18}O$_2$ exchange due to its higher concentrations of defect sites.[16] Therefore, carboxylic acid adsorbs at the exchange sites of the catalyst to a much higher extent, as shown by IR spectroscopy, hence, leading to higher reactivity in the reduction of stearic acid.
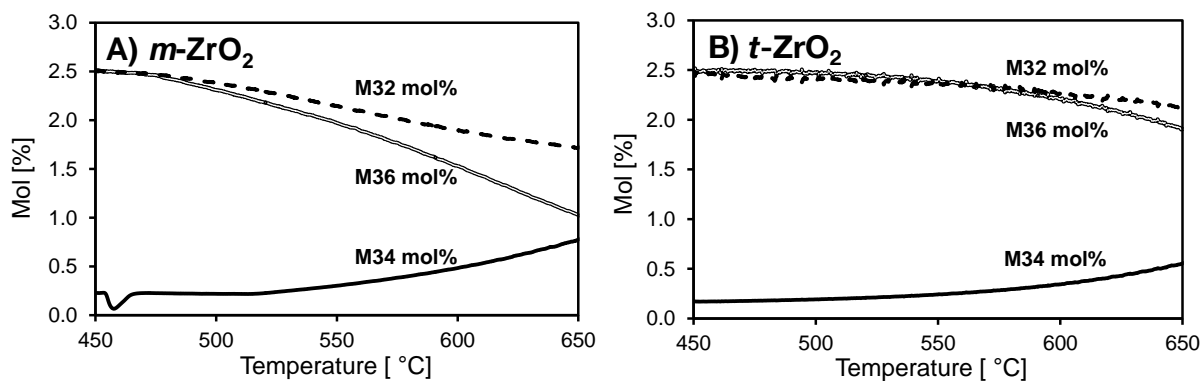
Figure 2-13. Temperature programmed isotopic exchange of ^{18}O-^{16}O with m-ZrO$_2$ **A)** and t-ZrO$_2$ **B)**. Mol% of M32 ($^{16}O_2$), M34 (^{18}O-^{16}O), and M36 ($^{18}O_2$) as a function of temperature from 450 °C to 650 °C with a temperature increase interval of 5 °C·min^{-1}.

2.4   Conclusions

The ZrO$_2$ morphology of m-, t-, and mix-phases affects markedly the hydrodeoxy-genation of stearic acid over Ni/ZrO$_2$ (with identical Ni particle sizes and distribution, as well as BET surface areas and acid and base site concentration) in dodecane. Ni/m-ZrO$_2$ has a three times higher activity towards stearic acid hydrogenation than Ni/t-ZrO$_2$ both selec-tively forming 1-octadecanol at low conversions. Surprisingly, this ratio agrees well with the ratio found for hydrogenation on bare m- and t-ZrO$_2$. Rate constants for Ni/ZrO$_2$ catalyzed stearic acid hydrogenation are comparable in the fitted and calculated individual measure-ment indicating very similar adsorption constants for reactants, intermediates, and products. The much lower (fitted) rate constant for decarbonylation of 1-octadecanol in the overall stearic acid hydrodeoxygenation is attributed primarily to competition of reactant and inter-mediates for sites in the conversion. The positive effect of m-ZrO$_2$ is concluded to be related to the substantially higher adsorbed concentration of the acid (concluded from the higher concentration of adsorbed propionic acid) on m-ZrO$_2$ compared to t-ZrO$_2$. The higher con-centration of adsorbed reactants is related to the higher concentration of defect sites on the ZrO$_2$-surface as detected by the higher oxygen exchange ability of m-ZrO$_2$ support (quanti-fied in the temperature programmed isotope exchange experiment). The results show that it is possible to enhance reactivity for the reductive conversion of fatty acids by maximizing the concentration of oxygen defects sites.

2.5 Experimental Section – Materials and Methods

2.5.1 Chemicals

All chemicals, *i.e.*, Zr(OH)$_4$ × H$_2$O (XZO 1247/01, MEL Chemicals), ZrO(NO$_3$)$_2$ × x H$_2$O (Sigma-Aldrich, 99%), methanol (Sigma-Aldrich, 99%), urea (Grünning, 99.5%), Ni(NO$_3$)$_2$·6 H$_2$O (Acros Organics, ≥98.5%), stearic acid (Sigma-Aldrich, ≥99.5% analytical standard), 1-octadecanol (Sigma-Aldrich, ≥99.5% Selectophore^{TM}), *n*-octadecane (Sigma-Aldrich, 99%), *n*-heptadecane (Sigma-Aldrich, 99%), dodecane (Sigma-Aldrich, ≥99%, *ReagentPlus*), propionic acid (Sigma-Aldrich, ACS grade ≥99.5%) were purchased commercially and were not further purified.

2.5.2 Catalyst preparation

Three types of ZrO$_2$ supports were synthesized. Mix-phase ZrO$_2$ was prepared by calcination of Zr(OH)$_4$•H$_2$O at 400 °C in ambient air for 4 h. *Monoclinic-* and *tetragonal*-ZrO$_2$ were prepared by the solvothermal method by mixing ZrO(NO$_3$)$_2$ with water and methanol, respectively.[17] An aqueous or methanolic solution of ZrO(NO$_3$)$_2$ (0.6 mol·L^{-1}) was added with urea (urea/Zr = 10:1). The solvothermal reaction was performed in a stainless-steel autoclave with Teflon® liner at 160 °C and autogenous pressure for 21 h. After washing five times the precipitate with H$_2$O or MeOH, it was dried over night at 110 °C and then ground and calcined in air at 400 °C for 4 h at a heating rate of 2 °C·min^{-1} (flow rate: 100 mL·min^{-1}).

The 10 wt% Ni/ZrO$_2$ catalysts were prepared by impregnation. Ni(NO$_3$)$_2$·6 H$_2$O (3.30 g) was dissolved in deionized H$_2$O (5.0 g), and the resulting solution was added dropwise to the support under stirring in ambient air. The slurry was further stirred for 4 h, followed by drying at 110 °C overnight. Subsequently, the ground solid was calcined in synthetic air (flow rate: 100 mL·min^{-1}) at 450 °C for 4 h (heating rate: 2 °C·min^{-1}) and reduced in H$_2$ flow (flow rate: 100 mL·min^{-1}) at 500 °C for 4 h (heating rate: 2 °C·min^{-1}).

2.5.3 Catalyst characterization

X-ray powder diffraction (XRD) was performed on Philips X'Pert Pro System equipped with a Cu Kα radiation source (40 kV/45 mA) with 1.08 ° min^{-1} in the 2 θ range of 5-70 °. The ratio of *monoclinic* and *tetragonal* phases in *mix*-ZrO₂ was determined by **Equation 2-6** using the integrated intensities of the (111) and (11-1) reflecting *monoclinic* and *tetragonal* XRD patterns, respectively.[18] The (111)$_m$ and (11-1)$_m$ reflections for the *monoclinic* phase are at 2 θ of 31.4 ° and 28.3 °, respectively, while the (111)$_t$ reflection from *tetragonal* phase is at 2 θ of 30.4 °. Accordingly, the actual ratio of *monoclinic* to *tetragonal* ZrO₂ in the physically mixed Ni/*m:t*-ZrO₂ was determined using **Equation 2-6** after fitting and integrating the corresponding peaks from the XRD (**Figure A 2-1, B** and **Figure A 2-6**).

Equation 2-6

$$x_m = \frac{I\left(11\bar{1}\right)_m + I(111)_m}{I\left(11\bar{1}\right)_m + I(111)_m + I(111)_t}$$

Atomic absorption spectroscopy (AAS) was used to determine the Ni content of the catalysts with a UNICAM 939 AA-Spectrometer. Prior to measurement, the sample was dissolved in boiling concentrated hydrofluoric acid.

The **BET** surface area was determined by adsorption-desorption with nitrogen at -196 °C using a Sorptomatic 1990 series instrument. The sample was activated in vacuum at 250 °C for 2 h before measurement.

The **EDX** mappings were obtained using a JEM-ARM200CF operated at 200 kV with an integrated probe aberration (Cs) corrector and a cold-field emission gun (CFEG) electron source After reduction the finely ground powdered catalyst samples were stored and mounted under Ar atmosphere.

Temperature programmed desorption (TPD) of ammonia and carbon dioxide was carried out in a 6-fold parallel reactor system. The pressed samples (500-710 µm) were firstly activated in He at 500 °C for 1 h and loaded with the adsorbent NH₃ or CO₂ at a partial pressure of 1 *m*bar and 100 °C or 40 °C, respectively. The samples were then purged with

He for 1 h in order to remove physisorbed species. After activation, the six samples were heated from 100-770 °C with a rate of 10 °C·min⁻¹ to desorb NH_3 and from 40 to 700 °C to remove CO_2, and the signals were detected by a Balzers QME 200 mass spectrometer.

Temperature programmed reaction (TPR) with H_2 was performed in a packed bed flow reactor equipped with a mass spectrometer. First, 100 mg calcined Ni/ZrO_2 catalyst (250-400 µm) was activated in He at 200 °C (heating rate 10 °C·min⁻¹) for 30 min. and cooled to ambient temperature. The reduction was carried out from ambient temperature to 800 °C (heating rate: 10 °C·min⁻¹) and maintaining 800 °C for 30 min in 10% H_2/He mixture gas (2 mL·min⁻¹ H_2/18 mL·min⁻¹ He). The amount of water produced in the reaction was determined by an online mass spectrometer.

IR spectroscopy of adsorbed propionic acid was performed on a Bruker VERTEX 70 spectrometer at a resolution of 2 cm⁻¹ with 128 scans in the range of 400-4000 cm⁻¹. For the measurements, the samples were pressed into self-supporting wafers and mounted in the sample holder. The ZrO_2 samples were activated in vacuum ($p = 10^{-7}$ *m*bar) at 300 °C for 1 h. The Ni/ZrO_2 catalysts were activated in H_2 at 400 °C for 1 h, and then subsequently outgassed under vacuum ($p = 10^{-7}$ *m*bar) to remove H_2 while cooling to 40 °C. The adsorption of propionic acid was performed from 0.01 to 0.05 *m*bar until equilibrium was reached. In addition, the effect of temperature was investigated by heating the cell stepwise up to 250 °C. The IR spectra of adsorbed propionic acid were obtained by subtracting the activated sample, and then were normalized by the weight of sample wafer.

The **near-edge structure (XANES)** and extended **X-ray absorption fine-structure (EXAFS)** measurements were performed in transmission mode at the Pacific Northwest Consortium/X-ray Science Division (PNC/XSD) bending-magnet beamline at Sector 20 of the Advanced Photon Source (APS) at Argonne National Laboratory (ANL). Both Ni (8331.5 eV) and Zr (17995.88 eV) K-edge spectra were acquired. A combination of monochromator detuning (10%) and a harmonic rejection mirror placed upstream of the I_0 detector reduced contributions from higher harmonics. A Ni or Zr foil was placed downstream of the sample cell as a reference to calibrate the photon energy of each spectrum. Typically, two 15 min scans (Ni-edge spectra) and four 15 min scans (Zr-edge spectra) were averaged to generate the spectra. The catalyst samples were ground and mixed with boron nitride (catalyst:boron nitride, 20:80 wt%, 5:95 wt% for Ni- and Zr-edges, respectively), then pressed into 5 × 12 mm pellets (80 mg) and mounted onto a multiple sample holder.

ATHENA software package[19] was used to remove the background from the χ(k) oscillations. The Fourier transform of the *k*-space EXAFS data (both real and imaginary parts of $\chi(R)$) were fitted to a theoretical model (FEFF9) calculated using the ARTEMIS software package. A starting point for evaluating the nanoparticle structure was the measurement of reference standards including bulk (fcc) NiO, bulk (hcp) α-Ni(OH)$_2$, and bulk (fcc) Ni using literature values for their lattice parameters.[20] A combination of different single and multiple photo-electron scattering paths were used to fit the first 5 shells of the NiO, α-Ni(OH)$_2$, and Ni nanoparticles.[21] For samples containing both oxidation states, the structural parameters were constrained and then the percentage of each phase was fitted. As a starting point for modeling the ZrO$_2$ nanoparticles, crystalline *m*-ZrO$_2$ and bulk *t*-ZrO$_2$ structures derived from their lattice parameters were used.[22] Single scattering paths of Zr and O for the *monoclinic* and *tetragonal* phase were fitted according to Rush *et al.*[23]

For the **temperature programmed isotope (^{18}O$_2$ – ^{16}O$_2$) exchange** of *m*- and *t*-ZrO$_2$, 100 mg of the pelletized supports (500-710 µm) were diluted in 300 mg of SiC and packed into a fixed-bed reactor (inner diameter 4 mm). After outgassing the samples for 2 h at 450 °C in 10 mL·min^{-1} of He, ^{18}O$_2$ and ^{16}O$_2$ were fed simultaneously (each 2.5 mol%) while increasing the temperature to 650 °C (5 °C·min^{-1}). The atomic mass units of 32 (^{16}O$_2$), 34 (^{18}O^{16}O) and 36 (^{18}O$_2$) in the product stream were recorded as a function of time by a Pfeiffer OmniStarTM GSD 320 OC mass spectrometer.

2.5.4 Measurement of the catalytic activity

For a typical experiment to convert stearic acid or 1-octadecanol 1.0 g of the reactants and 0.1 g catalyst were mixed with 100 mL dodecane, loaded into the reactor (Parr, 300 mL), and then purged three times with H$_2$. The reaction was carried out at 260 °C in presence of 40 bar H$_2$ for 2 h at a stirring speed of 600 rpm. *In situ* sampling was performed every 20 min., and the liquid samples were analyzed by a Shimadzu 2010 GC-MS using a HP-5 capillary column (30 m, 0.32 mm inner diameter, 0.25 µm film) equipped with a flame ionization detector (FID). Reproducibility of the rates has been better than ± 5% for all experiments.

2.6 Acknowledgements

2.7 Contributions

Sebastian Foraita synthesized all samples, designed, performed and analyzed the experiments, maintained the reactor and the sample analysis (GC-MS) and prepared and edited

the manuscript. John L. Fulton and Donald M. Camaioni contributed by planning, the execution and analyzing the XAFS measurements, scientific discussions and correcting the manuscript. Zizwe A. Chase wrote the XAFS part of the publication. Aleksei Vjunov supported in carrying out the XAFS measurements. Pinghong Xu took EDX-TEM images. Eszter Baráth contributed by discussing the results and correcting the manuscript. Chen Zhao supported in planning the first experiments, scientifically discussing the results and correcting the manuscript. Johannes A. Lercher was supervising the whole research, discussing the results scientifically and correcting the manuscript.

2.8   Appendix
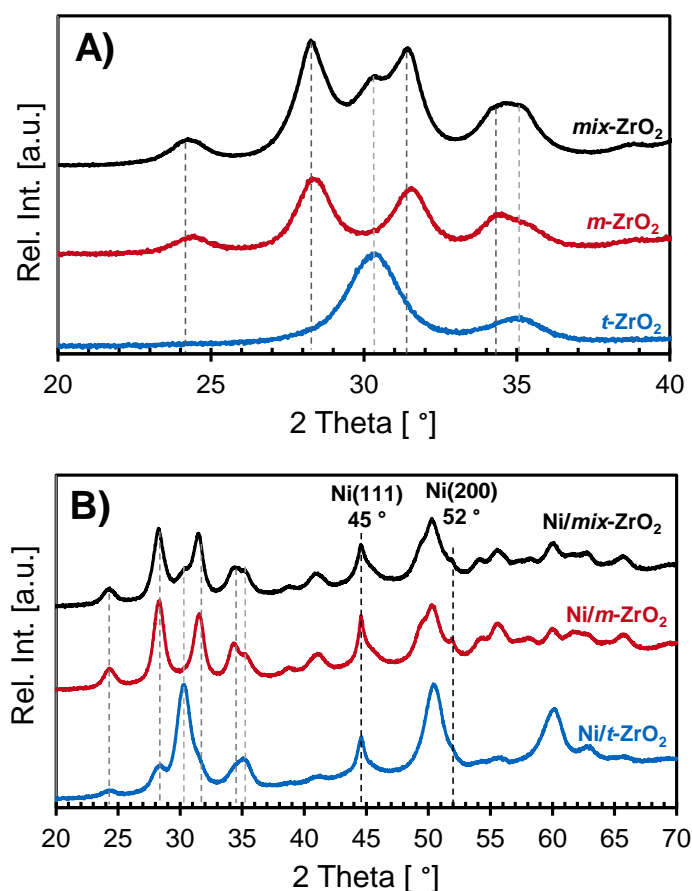
Figure A 2-1. XRD of **A)** mixed phase ZrO₂ (*mix*-ZrO₂), *monoclinic* ZrO₂ (*m*-ZrO₂), and *tetragonal* ZrO₂ (*t*-ZrO₂) and **B)** Ni incorporated Ni/*mix*-ZrO₂, Ni/*m*-ZrO₂, and Ni/*t*-ZrO₂.

Table A 2-1. Effect of the reduction temperature of $Ni/m\text{-}ZrO_2$ on stearic acid conversion and Ni-particle size.

Reduction temperature	Ni loading	Rate [a]	$d_{Ni\,(111)}$ [b]
[°C]	[wt%]	[$m$mol·$g_{cat.}^{-1}$·h^{-1}]	[nm]
500	9.7	2.6	13
550	9.7	2.0	14
600	9.7	1.0	19

[a] Reaction conditions: stearic acid (1.0 g), Ni/ZrO_2 (10 wt%, 0.1 g), dodecane (100 mL), 260 °C, $p(H_2) = 40$ bar, stirring at 600 rpm. [b] Determined by Scherrer Equation.

Table A 2-2. Ni-species of Ni/ZrO_2 catalysts determined by linear combination analysis from Ni-edge XANES.

Catalyst	Ni^0	Ni^{II}
	[%]	[%]
Ni/*mix*-ZrO_2 (before reaction)	70	30
Ni/*m*-ZrO_2 (b. rct.)	79	21
Ni/*t*-ZrO_2 (b. rct.)	77	23
Ni/*mix*-ZrO_2 (after reaction)	84	16
Ni/*m*-ZrO_2 (a. rct.)	85	15
Ni/*t*-ZrO_2 (a. rct.)	86	14
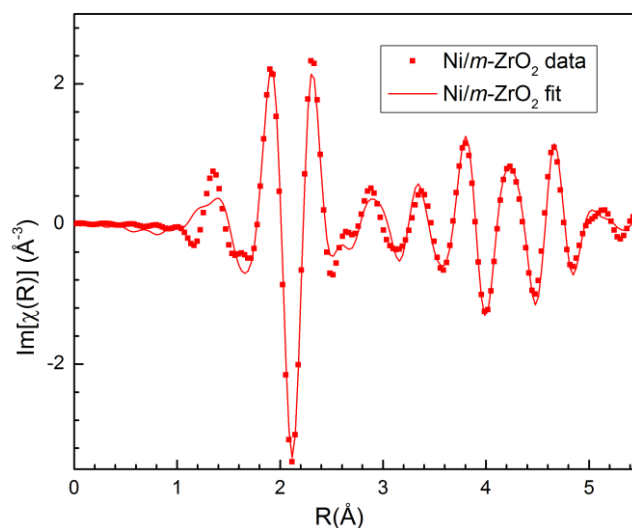
Figure A 2-2. Ni *K*-edge EXAFS spectra Fourier transforms (FTs) $Im[\chi(R)](Å^{-3})$ spectra of Ni/*m*-ZrO₂ and the corresponding fit (line).

Table A 2-3. ZrO₂ phase distributions in pure and Ni nanoparticle catalyst materials determined by linear combination analysis from Zr *K*-edge XANES.

Catalyst	*t*-ZrO₂ [%]	*m*-ZrO₂ [%]
mix-ZrO₂	25	75
m-ZrO₂	0	100
t-ZrO₂	100	0
Ni/*mix*-ZrO₂	6	94
Ni/*m*-ZrO₂	0	100
Ni/*t*-ZrO₂	62	38
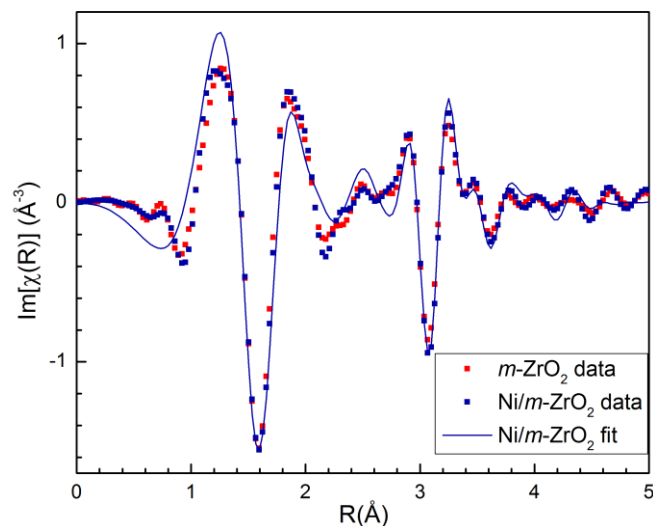
Figure A 2-3. Zr *K*-edge EXAFS spectra Fourier transforms (FTs) imaginary $\chi(R)$ plots of *m*-ZrO_2, and Ni/*m*-ZrO_2 at ambient temperature and the corresponding fit (line).
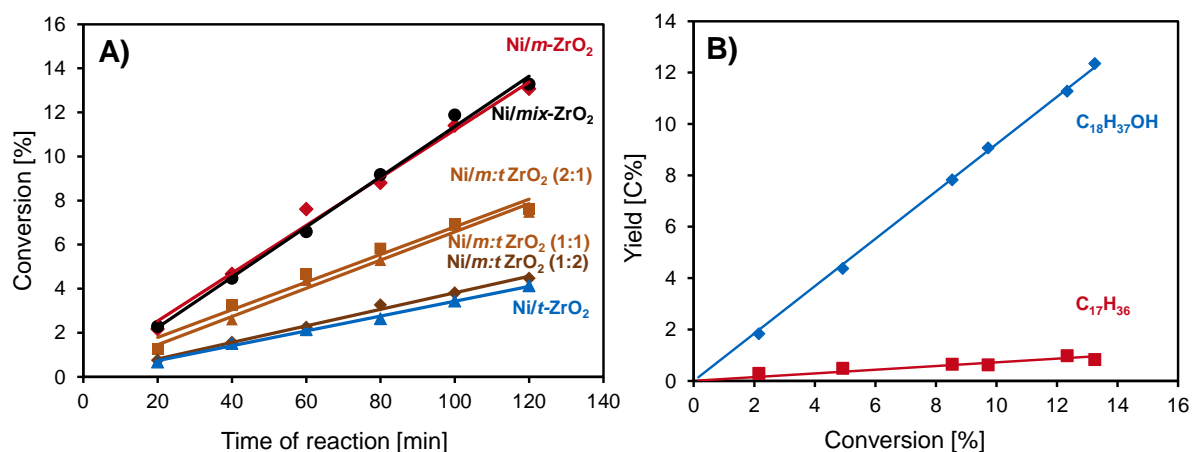
Figure A 2-4. A) Conversion of stearic acid as a function of time. **B)** Yields of 1-octadecanol and *n*-heptadecane over Ni/*m*-ZrO_2 as a function of stearic acid conversion. Reaction conditions: stearic acid (1.0 g), Ni/ZrO_2 (10 wt%, 0.1 g), dodecane (100 mL), 260 °C, $p(H_2) = 40$ bar, stirring at 600 rpm. Reproducibility of the rates has been better than ± 5%.

Table A 2-4. Infrared vibrational frequencies and band attributions for free propionic acid and adsorbed on ZrO_2 according to [15, 24].

Vibration mode	Free propionic acid	Adsorbed on ZrO_2
$\nu(ZrO-H)$ (doublet)		Negative 3774, 3668
$\nu(O-H)$	3600	/
$\nu(C-H\ sp^3)$	2986, 2945	2986, 2945
$\nu(C=O)$	1800, 1700 (doublet)	
$\nu_a(O-C-O)$		1556
$\nu_s(O-C-O)$		1419, 1475
C-O	1146	1302
$\delta(CH_3)$	Triplett 1500-1400	1475, 1419, 1379, 1302
$\rho(CH_3)$	1080	1080
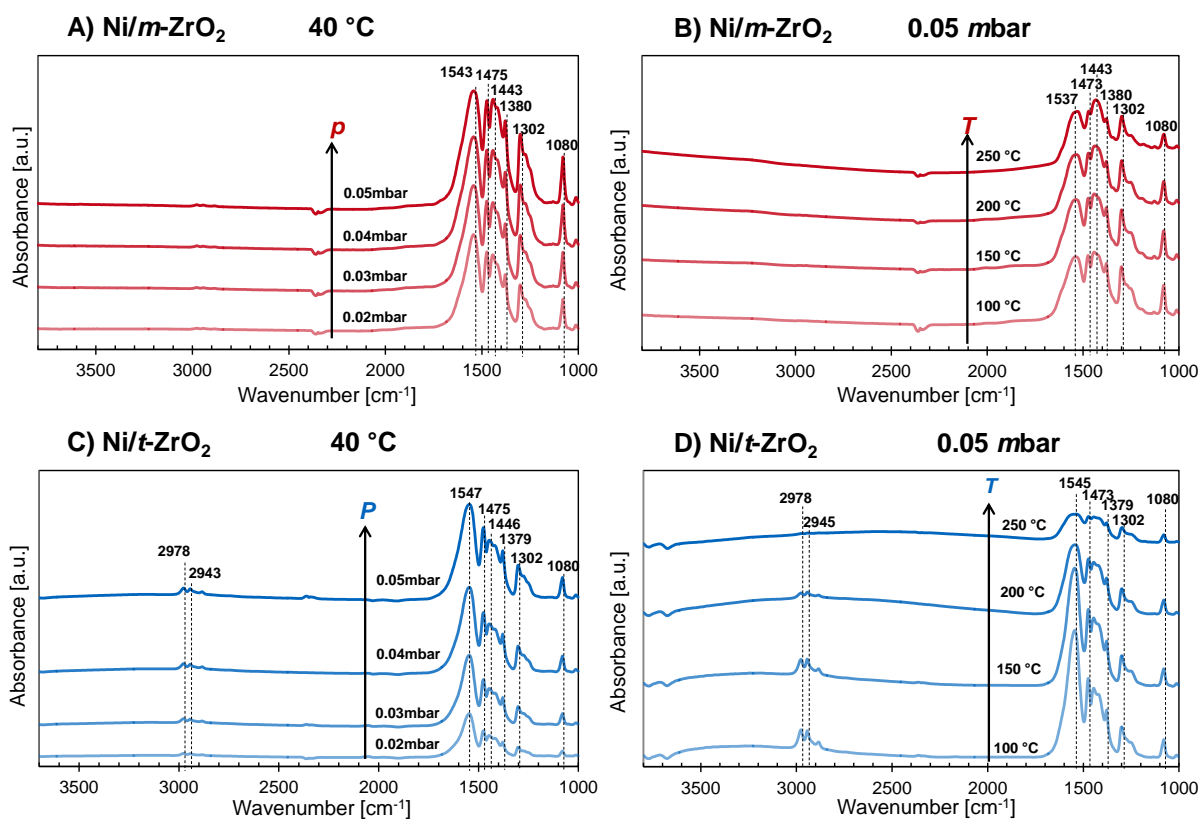
Figure A 2-5. IR spectra of adsorbed propionic acid on Ni/m-ZrO_2 and Ni/t-ZrO_2, with increasing pressures from 0.02 to 0.05 *m*bar at 40 °C (**A** and **C**), and with increasing temperatures from 100 °C to 250 °C at 0.05 *m*bar pressure (**B** and **D**).
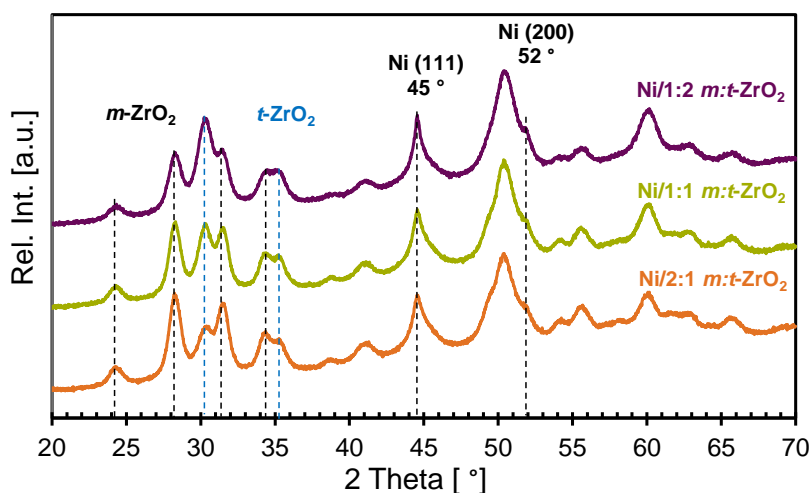
Figure A 2-6. XRD of Ni catalysts supported on 2:1-, 1:1-, 1:2-ratio mixture of *monoclinic* and *tetra-gonal* ZrO₂.

2.9   References

1. Huber, G. W.; Iborra, S.; Corma, A., Synthesis of Transportation Fuels from Biomass: Chemistry, Catalysts, and Engineering. *Chem. Rev.* **2006,** *106*, 4044-4098.

2. Jakkula, J.; Niemi, V.; Nikkonen, J.; Purola, V.-M.; Myllyoja, J.; Aalto, P.; Lehtonen, J.; Alopaeus, V. Process for producing a hydrocarbon component of biological origin. EP1396531A2, 2004.

3. (a) Zhao, C.; Bruck, T.; Lercher, J. A., Catalytic deoxygenation of microalgae oil to green hydrocarbons. *Green Chem.* **2013,** *15*, 1720-1739; (b) Furimsky, E., Chemistry of Catalytic Hydrodeoxygenation. *Catal. Rev.* **1983,** *25*, 421-458.

4. (a) Peng, B.; Yuan, X.; Zhao, C.; Lercher, J. A., Stabilizing Catalytic Pathways via Redundancy: Selective Reduction of Microalgae Oil to Alkanes. *J. Am. Chem. Soc.* **2012,** *134*, 9400-9405; (b) Peng, B.; Yao, Y.; Zhao, C.; Lercher, J. A., Towards Quantitative Conversion of Microalgae Oil to Diesel-Range Alkanes with Bifunctional Catalysts. *Angew. Chem., Int. Ed.* **2012,** *51*, 2072-2075.

5. Peng, B.; Zhao, C.; Kasakov, S.; Foraita, S.; Lercher, J. A., Manipulating Catalytic Pathways: Deoxygenation of Palmitic Acid on Multifunctional Catalysts. *Chem. - Eur. J.* **2013,** *19*, 4732-4741.

6. (a) Rhodes, M. D.; Bell, A. T., The effects of zirconia morphology on methanol synthesis from CO and over catalysts: Part I. Steady-state studies. *J. Catal.* **2005,** *233*, 198-209; (b) Rhodes, M. D.; Pokrovski, K. A.; Bell, A. T., The effects of zirconia morphology on

methanol synthesis from CO and H$_2$ over Cu/ZrO$_2$ catalysts: Part II. Transient-response infrared studies. *J. Catal.* **2005,** *233*, 210-220.

7. (a) Xu, B.-Q.; Wei, J.-M.; Yu, Y.-T.; Li, J.-L.; Zhu, Q.-M., Carbon Dioxide Reforming of Methane Over Nanocomposite Ni/ZrO$_2$ Catalysts. *Top. Catal.* **2003,** *22*, 77-85; (b) Tani, E.; Yoshimura, M.; Somiya, S., Formation of ultrafine tetragonal zirconia powder under hydrothermal conditions. *J. Am. Ceram. Soc.* **1983,** *66*, 11-14.

8. Zhao, C.; Yu, Y.; Jentys, A.; Lercher, J. A., Understanding the impact of aluminum oxide binder on Ni/HZSM-5 for phenol hydrodeoxygenation. *Appl. Catal., B* **2013,** *132–133*, 282-292.

9. (a) Hadjiivanov, K.; Mihaylov, M.; Klissurski, D.; Stefanov, P.; Abadjieva, N.; Vassileva, E.; Mintchev, L., Characterization of Ni/SiO$_2$ Catalysts Prepared by Successive Deposition and Reduction of Ni^{2+} Ions. *J. Catal.* **1999,** *185*, 314-323; (b) Song, W.; Zhao, C.; Lercher, J. A., Importance of Size and Distribution of Ni Nanoparticles for the Hydrodeoxygenation of Microalgae Oil. *Chem. - Eur. J.* **2013,** *19*, 9833-9842.

10. (a) Chenu, E.; Jacobs, G.; Crawford, A. C.; Keogh, R. A.; Patterson, P. M.; Sparks, D. E.; Davis, B. H., Water-gas shift: an examination of Pt promoted MgO and tetragonal and monoclinic ZrO$_2$ by in situ drifts. *Appl. Catal., B* **2005,** *59*, 45-56; (b) Li, P.; Chen, I. W.; Penner-Hahn, J. E., X-ray absorption studies of zirconia polymorphs. I. Characteristic local structures. *Phys. Rev. B: Condens. Matter* **1993,** *48*, 10063-73.

11. (a) Soo, Y. L.; Chen, P. J.; Huang, S. H.; Shiu, T. J.; Tsai, T. Y.; Chow, Y. H.; Lin, Y. C.; Weng, S. C.; Chang, S. L.; Wang, G.; Cheung, C. L.; Sabirianov, R. F.; Mei, W. N.; Namavar, F.; Haider, H.; Garvin, K. L.; Lee, J. F.; Lee, H. Y.; Chu, P. P., Local structures surrounding Zr in nanostructurally stabilized cubic zirconia: Structural origin of phase stability. *J. Appl. Phys.* **2008,** *104*, 113535-113535; (b) Acuna, L. M.; Lamas, D. G.; Fuentes, R. O.; Fabregas, I. O.; Fantini, M. C. A.; Craievich, A. F.; Prado, R. J., Local atomic structure in tetragonal pure ZrO$_2$ nanopowders. *J. Appl. Crystallogr.* **2010,** *43*, 227-236; (c) Yang, P.; Cai, X.; Xie, Y.; Xie, Y.; Hu, T.; Zhang, J.; Liu, T., Extended X-ray Absorption Fine Structure Studies on Mixed-Phase Zirconia. *J. Phys. Chem. B* **2003,** *107*, 6511-6513.

12. Thromat, N.; Noguera, C.; Gautier, M.; Jollet, F.; Duraud, J. P., Electronic structure and atomic arrangement around zirconium substituted for yttrium in yttrium sesquioxide. *Phys. Rev. B* **1991,** *44*, 7904-11.

13. (a) Pestman, R.; Koster, R. M.; Boellaard, E.; van der Kraan, A. M.; Ponec, V., Identification of the Active Sites in the Selective Hydrogenation of Acetic Acid to Acetaldehyde on Iron Oxide Catalysts. *J. Catal.* **1998,** *174*, 142-152; (b) Pestman, R.; Koster, R. M.; Pieterse, J. A. Z.; Ponec, V., Reactions of Carboxylic Acids on Oxides: 1. Selective Hydrogenation of Acetic Acid to Acetaldehyde. *J. Catal.* **1997,** *168*, 255-

264; (c) Pestman, R.; Koster, R. M.; van Duijne, A.; Pieterse, J. A. Z.; Ponec, V., Reactions of Carboxylic Acids on Oxides: 2. Bimolecular Reaction of Aliphatic Acids to Ketones. *J. Catal.* **1997,** *168*, 265-272; (d) Pestman, R.; van Duijne, A.; Pieterse, J. A. Z.; Ponec, V., The formation of ketones and aldehydes from carboxylic acids, structure-activity relationship for two competitive reactions. *J. Mol. Catal. A: Chem.* **1995,** *103*, 175-180.

14. (a) Pei, Z. F.; Ponec, V., On the intermediates of the acetic acid reactions on oxides: an IR study. *Appl. Surf. Sci.* **1996,** *103*, 171-182; (b) Jacob, K. H.; Knoezinger, E.; Benier, S., Adsorption sites on polymorphic zirconia. *J. Mater. Chem.* **1993,** *3*, 651-7.

15. (a) Chen, L.; Zhu, Y.; Zheng, H.; Zhang, C.; Li, Y., Aqueous-phase hydrodeoxygenation of propanoic acid over the Ru/ZrO_2 and Ru–Mo/ZrO_2 catalysts. *Appl. Catal., A* **2012,** *411–412*, 95-104; (b) Rachmady, W.; Vannice, M. A., Acetic Acid Reduction by H_2 over Supported Pt Catalysts: A DRIFTS and TPD/TPR Study. *J. Catal.* **2002,** *207*, 317-330.

16. Heracleous, E.; Lemonidou, A. A., Ni-Nb-O mixed oxides as highly active and selective catalysts for ethene production via ethane oxidative dehydrogenation. Part II: Mechanistic aspects and kinetic modeling. *J. Catal.* **2006,** *237*, 175-189.

17. Li, W.; Huang, H.; Li, H.; Zhang, W.; Liu, H., Facile Synthesis of Pure Monoclinic and Tetragonal Zirconia Nanoparticles and Their Phase Effects on the Behavior of Supported Molybdena Catalysts for Methanol-Selective Oxidation. *Langmuir* **2008,** *24*, 8358-8366.

18. Schmid, H. K., Quantitative Analysis of Polymorphic Mixes of Zirconia by X-ray Diffraction. *J. Am. Ceram. Soc.* **1987,** *70*, 367-376.

19. Ravel, B.; Newville, M., ATHENA, ARTEMIS, HEPHAESTUS: data analysis for x-ray absorption spectroscopy using IFEFFIT. *J. Synchrotron Radiat.* **2005,** *12*, 537-541.

20. (a) Smith, N., Structure of thin films of metallic oxides and hydrates. *J. Am. Chem. Soc.* **1936,** *58*, 173-9; (b) Bode, H.; Dehmelt, K.; Witte, J., Nickel hydroxide electrodes. I. Nickel(II) hydroxide hydrate. *Electrochim. Acta* **1966,** *11*, 1079-87.

21. Frenkel, A. I.; Hills, C. W.; Nuzzo, R. G., A View from the Inside: Complexity in the Atomic Scale Ordering of Supported Metal Nanoparticles. *J. Phys. Chem. B* **2001,** *105*, 12689-12703.

22. (a) Torres, F. J.; Amigó, J. M.; Alarcón, J., X-ray powder diffraction study of monoclinic V^{4+}-ZrO_2 solid solutions obtained from gels. *J. Solid State Chem.* **2003,** *173*, 40-44; (b) Barker, W. W.; Bailey, F. P.; Garrett, W., A high-temperature neutron diffraction study of pure and scandia-stabilized zirconia. *Journal of Solid State Chemistry* **1973,** *7*, 448-453.

23. Rush, G. E.; Chadwick, A. V.; Kosacki, I.; Anderson, H. U., An EXAFS Study of Nanocrystalline Yttrium Stabilized Cubic Zirconia Films and Pure Zirconia Powders. *J. Phys. Chem. B* **2000,** *104*, 9597-9606.

24. Bachiller-Baeza, B.; Rodriguez-Ramos, I.; Guerrero-Ruiz, A., Interaction of Carbon Dioxide with the Surface of Zirconia Polymorphs. *Langmuir* **1998,** *14*, 3556-3564.

Chapter 3

Controlling Hydrodeoxygenation of Stearic Acid to *n*-Heptadecane and *n*-Octadecane *via* Chemical Properties of Ni/SiO$_2$-ZrO$_2$

This chapter is based on the following publication:

Hydrothermally synthesized SiO$_2$-ZrO$_2$ mixed oxide has novel nano-layers possessing Brønsted acid sites and high specific surface area. Used as supports for Ni catalyst, they enhanced the activity for fatty acid reduction compared to Ni/ZrO$_2$.
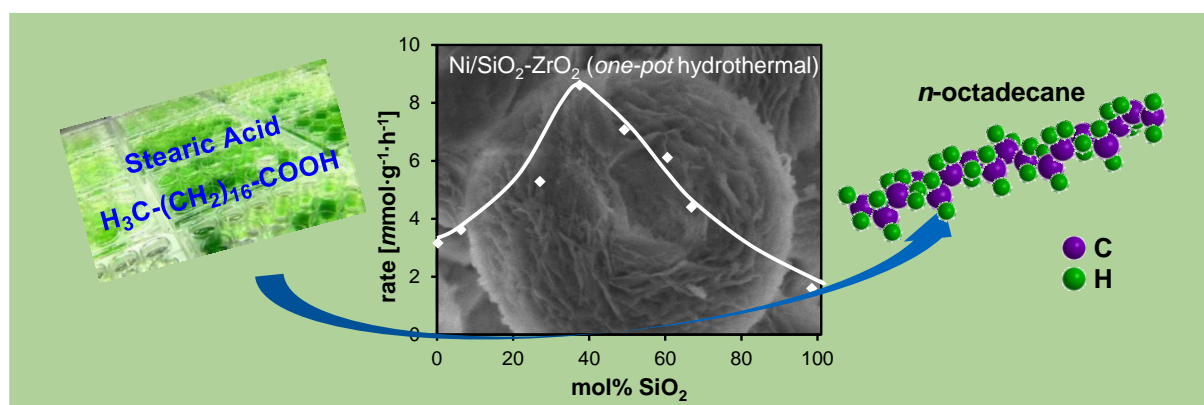
Keywords: Hydrodeoxygenation • Decarbonylation • SEM • IR Spectroscopy • SiO$_2$-ZrO$_2$ mixed Oxide

3.1 Abstract

A series of SiO$_2$-ZrO$_2$ mixed oxide with varying SiO$_2$ concentrations was hydrothermally synthesized and used as support for Ni in the hydrodeoxygenation of stearic acid. ZrO$_2$ provides a relatively low surface area and only Lewis acid sites, and Ni supported on ZrO$_2$ produces *n*-heptadecane from stearic acid *via* hydrogenation and decarbonylation. The SiO$_2$-ZrO$_2$ mixed oxides have a higher specific surface area as well as a novel spherical and nano-layer shaped morphology. Brønsted acid sites are created by incorporation of SiO$_2$ into ZrO$_2$ promoting the hydrodeoxygenation activity of Ni and specifically opening a new reaction route to *n*-octadecane *via* the dehydration of 1-octadecanol intermediate into 1-octadecene with subsequent hydrogenation.

3.2 Introduction

The high growth rates and oil content, as well as the independence from arable land make microalgae the ideal basis for third-generation biofuels.[1] The conversion of algae oil into hydrocarbon transportation fuel requires removing of oxygen from triglycerides. This can be achieved using commercially available sulfide catalysts, *e.g.* NiMoS/Al$_2$O$_3$, and existing hydrotreating infrastructure.[2] However, the sulfide catalysts are not ideal for the conversion of the nearly sulfur-free triglycerides, because they deactivate *via* sulfur elimination and contaminate the product stream with organic sulfides.[3]

Supported noble metal Ru, Pd and Pt catalysts overcome such disadvantages offering high activity and selectivity for hydrodeoxygenation of triglycerides and fatty acids, but are rather expensive.[4] A more economic alternative would be tungsten carbide based catalysts, however, their performance has not been able to reach the performance of commercial hydrotreating catalysts (NiMo/Al$_2$O$_3$).[5]

In order to directly convert microalgae oil to diesel-range hydrocarbons at 260 °C and 40 bar H$_2$, two types of novel sulfur-free Ni based catalysts were developed.[6] The catalytic process starts with fast hydrogenolysis into propane and fatty acids followed by slower hydrodeoxygenation of the fatty acids into alkanes.[6a] The conversion of fatty acids, *e.g.* stearic acid, on Ni/ZrO$_2$ occurs *via* two pathways, one catalyzed solely by Ni and one catalyzed synergistically by Ni and the ZrO$_2$ support, both leading to an alkane with one carbon

less than the fatty acid, *i.e.*, *n*-heptadecane (C$_{17}$) from stearic acid (C$_{18}$). On Ni, the fatty acid is hydrogenated to the aldehyde, followed by decarbonylation of the aldehyde to an alkane. On ZrO$_2$, α-H abstraction and elimination of H$_2$O from the fatty acid adsorbed on the oxygen vacancies leads to a ketene intermediate, which is further hydrogenated to an aldehyde that decarbonylates to an alkane on Ni.[7]

Generally, ZrO$_2$ is an excellent catalytic support, *inter alia* due to its high hydrothermal stability.[8] The relatively low specific surface area poses some drawbacks, as the sites involved in the hydrodeoxygenation pathway on ZrO$_2$ contribute markedly to the overall conversion. The incorporation of SiO$_2$ has been reported to enhance the specific surface area of ZrO$_2$ [9] through formation of a mixed oxide phase, and can additionally induce Brønsted acid sites.[10] It has been shown previously that the presence of Brønsted acid sites in proximity to Ni in zeolites enhances the hydrogenation activity.[11]

Therefore, the general applicability of the concept of rate enhancement by introducing Brønsted acid sites *via* SiO$_2$-ZrO$_2$ mixed oxides on the support for Ni with respect to the hydrodeoxygenation of stearic acid, one of the most abundant fatty acids from algae oil, was explored. It was hypothesized that the combination of the large pore Brønsted acid support with Ni as hydrogenation catalyst function may lead to high activity and high selectivity retaining all carbon atoms in the fatty acid.

3.3   Results and Discussion

The catalytic properties of two types of Ni catalysts, prepared by wet impregnation on hydrothermally synthesized and impregnated SiO$_2$-ZrO$_2$ supports are investigated. For details of the preparation procedure please see experimental part (page 74).

3.3.1   Catalyst characterization

The **X-ray powder diffractogram (XRD)** of the ZrO$_2$ samples, prepared by the hydrothermal synthesis (H), are presented in **Figure 3-1**. The diffractogram of unmodified *monoclinic* ZrO$_2$ (*m*-ZrO$_2$) with its characteristic diffraction pattern is shown as well for comparison. It shows the expected diffraction peaks at 24.5, 28.3, 31.6 and 34.5° with a

shoulder at 35.3° (JCPDS card No. 37-1484).[12] With increasing SiO$_2$-content, the peak intensity (6 SiO$_2$-ZrO$_2$ (H)) decreased, suggesting lower crystallinity. In parallel, the crystal phase of ZrO$_2$ changed from *monoclinic* to a new phase (27 SiO$_2$-ZrO$_2$ and 37 SiO$_2$-ZrO$_2$ (H)), which has been assigned to *tetragonal* ZrO$_2$ in literature.[12c, 12d] Above 40 wt% SiO$_2$, only broad signals characteristic for amorphous oxides[13] were observed, while diffraction peaks of either *monoclinic* or *tetragonal* ZrO$_2$ were absent, implying an amorphous structure of the resulting materials.[14] In line with that, the peak attributed to pure SiO$_2$ was lowered in intensity. Presumably, this is the result of atomic dispersion in mixed SiO$_2$-ZrO$_2$ where Zr-O units are alternating with SiO$_4$-tetrahedra. In contrast, the diffraction patterns remain identical when the ZrO$_2$ is modified by impregnation with SiO$_2$, indicating the crystal structure of ZrO$_2$ is not affected by SiO$_2$ (**Figure 3-2**).
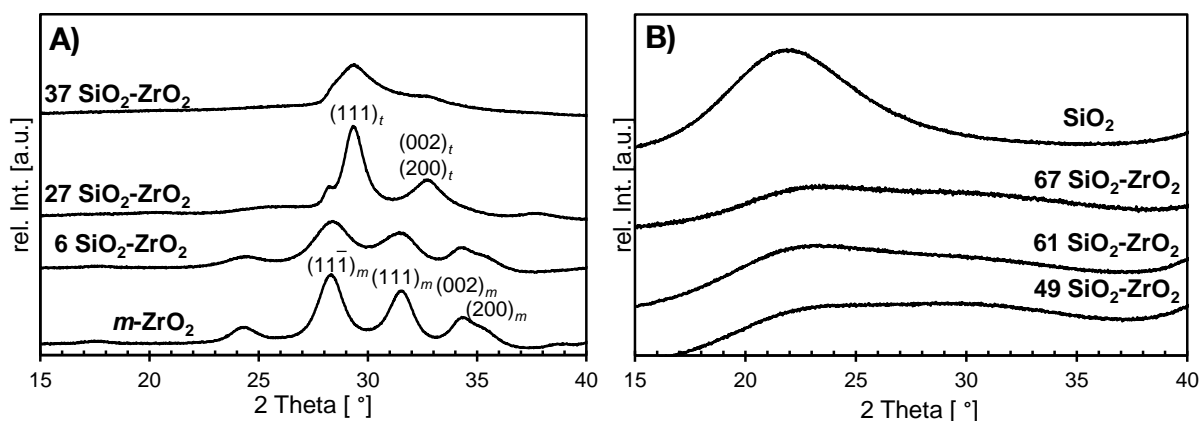
Figure 3-1. XRD patterns of ZrO$_2$ modified with increasing concentrations of SiO$_2$ by the hydrothermal method. **A)** 0-37 mol% SiO$_2$. **B)** 49-100 mol% SiO$_2$.
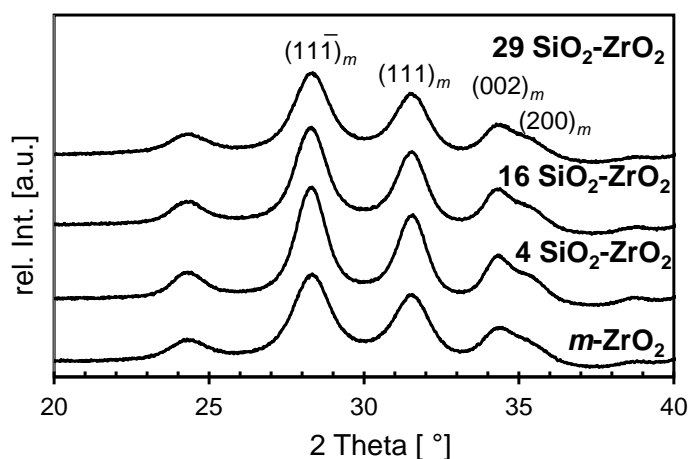
Figure 3-2. XRD patterns of ZrO$_2$ modified with increasing amount of SiO$_2$ by impregnation method (0-29 mol%).

High Resolution Scanning Electron Microscopy (HR-SEM)

The highly increased specific surface area of the materials prepared by the hydro-thermal method is also manifested in the HR-SEM micrographs. While unmodified ZrO$_2$ (**Figure 3-3**, upper left) showed particles with several micrometers in diameter, the surface of ZrO$_2$-SiO$_2$ is more facetted, forming nano-layers with increasing content of SiO$_2$. For 37 SiO$_2$-ZrO$_2$, highly organized structures with a primary particle size of 1 µm are formed. Nano layers arrange in a way that spheres with sponge like morphologies are formed. Similar structures were reported by Faria *et al.*[15] The 67 ZrO$_2$-SiO$_2$ had an extraordinary morphology, in which the excess SiO$_2$ not incorporated into ZrO$_2$ was deposited on the surface of the lamellar structure as SiO$_2$-nanoparticles with a size of 10 nm (**Figure 3-3**, bottom right). In contrast, the SiO$_2$ *impregnated* ZrO$_2$ samples did not show such a change in morphology and were comparable in shape to the reference material independent of the degree of the SiO$_2$ loading (**Figure 3-4**). The silica deposits are visible on the ZrO$_2$ surface.
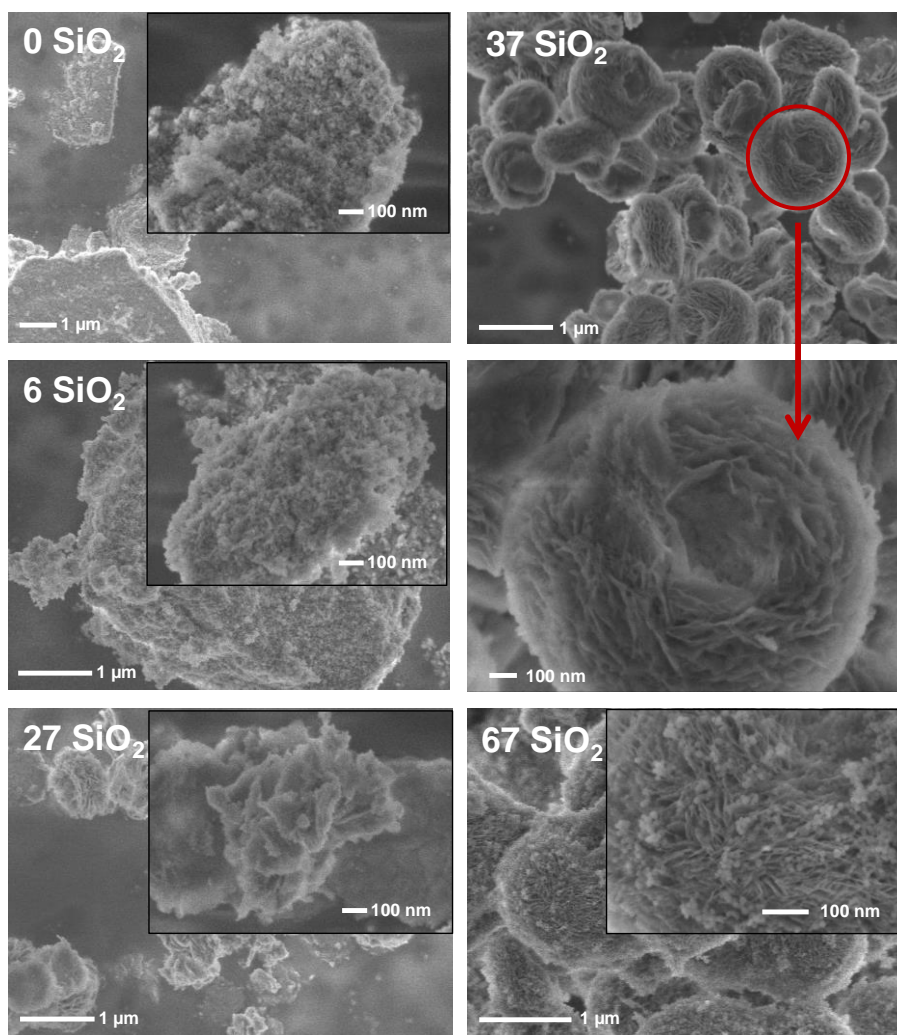
Figure 3-3. High resolution scanning electron microscopy (HR-SEM) images of untreated ZrO$_2$ (0 mol% SiO$_2$), 6 SiO$_2$-ZrO$_2$, 27 SiO$_2$-ZrO$_2$, 37 SiO$_2$-ZrO$_2$, 67 SiO$_2$-ZrO$_2$ prepared by *one-pot* hydrothermal method.
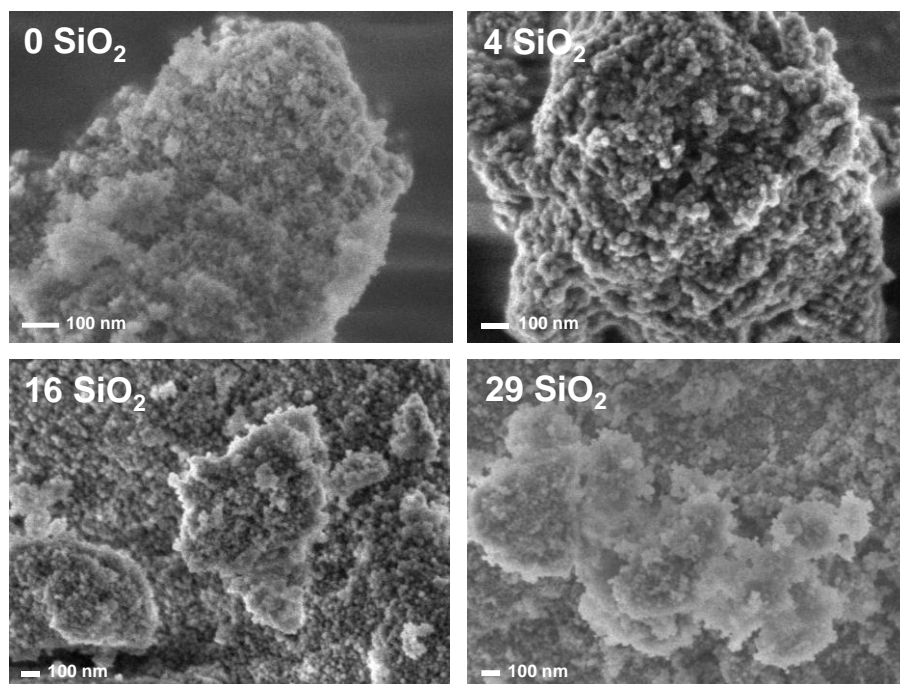
Figure 3-4. HR-SEM images of untreated ZrO$_2$ (0 mol% SiO$_2$) and ZrO$_2$ impregnated with SiO$_2$ at increasing loadings.

Physicochemical properties

As shown in **Table 3-1**, with the increase of SiO$_2$ concentration, the BET surface areas of the Ni/SiO$_2$-ZrO$_2$, determined by N$_2$ physisorption, increased from 72 m$^2 \cdot$g^{-1} for Ni/*m*-ZrO$_2$ to 193 m$^2 \cdot$g^{-1} for Ni/37 SiO$_2$-ZrO$_2$, significantly higher than reported before,[16] while it afterwards decreased to 67 m$^2 \cdot$g^{-1} for Ni/67 SiO$_2$-ZrO$_2$, which is close to the value for Ni/SiO$_2$. The high BET surface area for Ni/37 SiO$_2$-ZrO$_2$ (193 m$^2 \cdot$g^{-1}) is due to the small crystal size, which was only 2.5 nm compared to 7.1 nm of *m*-ZrO$_2$ (**Table A 3-1, Appendix,** page 79). In contrast, the catalysts prepared by the SiO$_2$-impregnation method only had specific surface areas between 71-97 m$^2 \cdot$g^{-1} (**Table 3-2**).

Table 3-1: Physicochemical properties of SiO$_2$ modified Ni/ZrO$_2$ catalysts (*one-pot* hydrothermal).

Catalyst [a]	S_{BET}	wt% Ni [b]	D [c]	D [c]	Concentration of acid sites [d]	Concentration of basic sites [e]
	[m^2·g^{-1}]	[%]	[%]	[nm]	[*m*mol·g^{-1}]	[*m*mol·g^{-1}]
Ni/ZrO$_2$	72	9.7	2.9	35	0.15	0.30
Ni/6 SiO$_2$-ZrO$_2$	122	9.4	2.5	41	0.23	0.25
Ni/27 SiO$_2$-ZrO$_2$	128	9.8	1.8	57	0.34	0.23
Ni/37 SiO$_2$-ZrO$_2$	193	10	1.7	61	0.28	0.12
Ni/49 SiO$_2$-ZrO$_2$	141	9.8	1.9	52	0.24	0.10
Ni/61 SiO$_2$-ZrO$_2$	111	9.8	2.1	49	0.19	0.09
Ni/67 SiO$_2$-ZrO$_2$	67	10	2.5	40	0.11	0.06
Ni/SiO$_2$	75	9.5	3.8	27	0	0

[a] Number in the label is mol% SiO$_2$. [b] Determined by Ni-AAS. [c] Dispersion (*D*) and particle size (*d*) were determined by H$_2$-Chemisorption. [d] Determined by TPD of NH$_3$. [e] Determined by TPD of CO$_2$.

Table 3-2: Physicochemical properties of SiO$_2$ impregnated Ni/ZrO$_2$ catalysts.

Catalyst [a]	S_{BET}	wt% Ni [b]	D [c]	d [c]	Concentration of acid sites [d]	Concentration of basic sites [e]
	[m^2·g^{-1}]	[%]	[%]	[nm]	[*m*mol·g^{-1}]	[*m*mol·g^{-1}]
Ni/ZrO$_2$	72	9.7	2.9	35	0.15	0.30
Ni/4 SiO$_2$-ZrO$_2$	71	10	3.0	33	0.16	0.19
Ni/16 SiO$_2$-ZrO$_2$	86	9.7	3.1	33	0.16	0.14
Ni/29 SiO$_2$-ZrO$_2$	97	9.9	3.6	28	0.16	0.10

[a] Number in the label is mol% SiO$_2$. [b] Determined by Ni-AAS. [c] Dispersion (*D*) and particle size (*d*) were determined by H$_2$-Chemisorption. [d] Determined by TPD of NH$_3$. [e] Determined by TPD of CO$_2$.

The concentration of acid sites were always lower for the Ni-impregnated catalysts than for the parent supports (compare **Table 3-1** with **Table A 3-1** and **Table 3-2** with

Table A 3-2). The acid site concentration increased from 0.15 to 0.34 *m*mol·g^{-1} for Ni/ZrO$_2$ to Ni/27 SiO$_2$-ZrO$_2$ (H) and decreased to 0 for Ni/SiO$_2$ (**Table 3-1**). The concentration of acid sites for the Ni-catalysts, modified by SiO$_2$-impregnation was constant at 0.16 *m*mol·g^{-1} (**Table 3-2**) and was lower than that of the corresponding parent support (**Table A 3-2**). This indicates that the ZrO$_2$ surface and its acid sites are partially blocked by SiO$_2$. With the increase of the SiO$_2$ content, the basic site concentration for the mixed oxides prepared with the hydrothermal method decreased from 0.25 to 0 *m*mol·g^{-1}, and that for the SiO$_2$ impregnated samples decreased from 0.19 to 0.10 *m*mol·g^{-1}, in line with similar studies on SiO$_2$-ZrO$_2$ mixed oxides by Yamaguchi *et al.*[17]

IR spectra of adsorbed pyridine

In **Figure 3-5** the IR spectra of adsorbed pyridine are shown for unmodified *monoclinic* ZrO$_2$, SiO$_2$-ZrO$_2$ (37 SiO$_2$-ZrO$_2$, H), SiO$_2$-impregnated ZrO$_2$ (29 SiO$_2$-ZrO$_2$, Imp.) and a pure SiO$_2$ reference. The ZrO$_2$ showed the bands of pyridine adsorbed on Lewis acid sites (LAS) at 1610 and 1448 cm^{-1} (**Figure 3-5, A**). SiO$_2$-ZrO$_2$ showed emerging peaks at 1630 and 1547 cm^{-1} attributed to pyridinium ions formed by adsorption on Brønsted acid sites (BAS). The band at 1462 cm^{-1} is attributed to pyridine coordinately adsorbed on Lewis acid sites (LAS), the band at 1491 cm^{-1} to pyridine adsorbed on both strong LAS and BAS.[18] **Table 3-3** shows the quantification of BAS and LAS for 27 SiO$_2$-ZrO$_2$ (H) and 37 SiO$_2$-ZrO$_2$ (H). 27 SiO$_2$-ZrO$_2$ (H) had the highest total concentration of acid sites (0.93 *m*mol·g^{-1}), and 37 SiO$_2$-ZrO$_2$ (H) has the highest concentration of BAS (0.36 *m*mol·g^{-1}). In contrast, the impregnated material (29 SiO$_2$-ZrO$_2$, Imp.) showed adsorption on identical sites as on ZrO$_2$, but in lower concentrations. This is attributed to the fact that ZrO$_2$ is partially covered by SiO$_2$, leading to fewer accessible Lewis acid sites. Finally, the pure SiO$_2$ reference did not adsorb significant concentrations of pyridine after evacuation at 150°C.

The broad peaks at 3774 and 3680 cm^{-1} (**Figure 3-5, B**) are assigned to the stretching vibrations of terminal and bridging surface OH groups of Zr, respectively, that disappear upon adsorption of pyridine and are visible as negative peaks in the difference spectra.[16b, 18d, 19] The band at 3735 cm^{-1} (37 SiO$_2$-ZrO$_2$ (H) and 29 SiO$_2$-ZrO$_2$ Imp.) is attributed to isolated SiOH groups.[18a, 20]
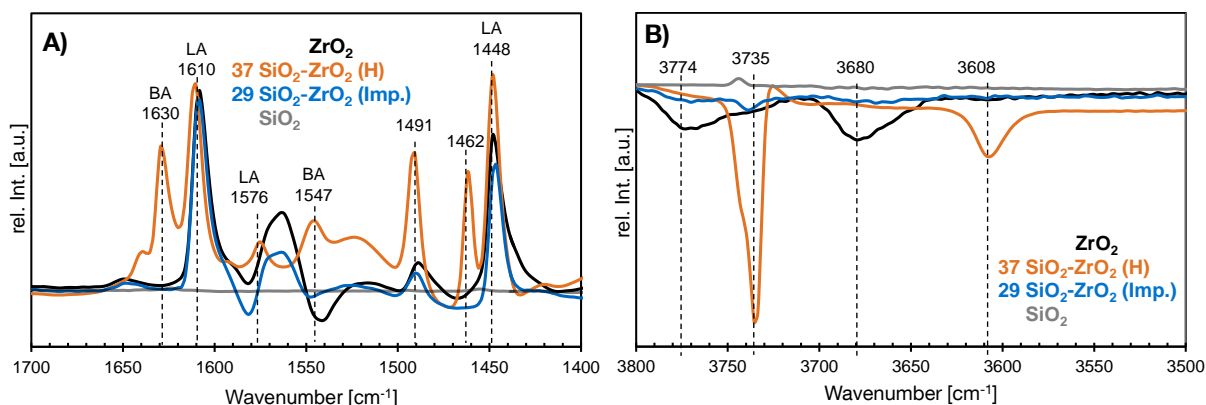
Figure 3-5. IR spectra of pyridine adsorbed on ZrO$_2$ (black), 37 SiO$_2$-ZrO$_2$ (*one-pot* hydrothermal synthesis) in orange, 29 SiO$_2$-ZrO$_2$ (Impregnation) in blue and SiO$_2$ reference (gray). **A)** Pyridine vibrations region (1700-1400 cm^{-1}) **B)** Surface Zr-OH and Si-OH stretching vibration region (3800-3500 cm^{-1}).

Table 3-3: Concentration of Brønsted and Lewis acid sites quantified by IR spectra of adsorbed pyridine.

Support/ modification	Total concentration of acid sites	Concentration of BAS	Concentration of LAS
	[µmol·g^{-1}]	[µmol·g^{-1}]	[µmol·g^{-1}]
Ni/27 SiO$_2$-ZrO$_2$	930	136	794
Ni/37 SiO$_2$-ZrO$_2$	730	356	374

The IR spectra of adsorbed pyridine for all samples prepared by the *one-pot* hydrothermal synthesis method with different SiO$_2$-contents are compared in **Figure 3-6, A**. As indicated in the previous paragraph, the spectrum of bare ZrO$_2$ and 6 SiO$_2$-ZrO$_2$ showed broad bands with low intensities at 3774 and 3680 cm^{-1} that are attributed to ZrOH groups (**Figure 3-6, B**). For higher contents of SiO$_2$ (27-61 mol%), bands at 3745-3735 cm^{-1} appeared that correspond to isolated SiOH groups. Like SiO$_2$, the mixed oxide with the highest SiO$_2$-content (69 SiO$_2$-ZrO$_2$) showed negligible adsorption of pyridine. The peak at 3608 cm^{-1} that only appeared for 27-SiO$_2$-ZrO$_2$ and 37 SiO$_2$-ZrO$_2$, should be highlighted, which also had the highest concentrations of BAS. This band at 3608 cm^{-1} is similar in wavenumber to the bridging OH groups in zeolites[21] responsible for the high Brønsted acid strength. Brønsted acid sites were suggested to be present in SiO$_2$-ZrO$_2$ as well (**Scheme 3-1, A**).[21c, 22] However, in a classic substitution model this would require a sufficient number of Zr^{3+}-cations[23], which are unlikely to be formed under the conditions employed.[24] Therefore,

a structure (**Scheme 3-1, B**) based on Pauling's electrostatic valence rule is tentatively proposed.[25] The coordination number (CN) of Zr in tetragonal ZrO$_2$, which is the dominating phase in the presence of SiO$_2$, is eight, whereas the CN(Si) = 4 in SiO$_2$. The incorporation of SiO$_2$ into the ZrO$_2$ structure and, thus, the formation of a mixed oxide lead to an under-coordination of the surface oxygen for ZrO$_2$ rich samples. This is hypothesized to be balanced by a proton, leading to an OH band at 3608 cm^{-1} accounting for the Brønsted acid site.[26] With increasing SiO$_2$-content, the incorporation cannot be stabilized, resulting in phase segregation and a lower concentration of BAS.
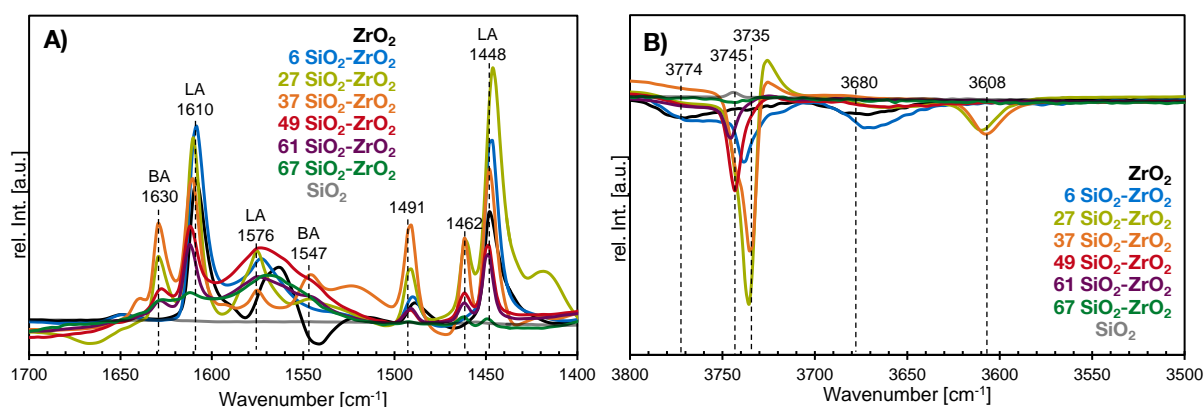
Figure 3-6. IR spectra of pyridine adsorbed on SiO$_2$-ZrO$_2$ (*one-pot* hydrothermal synthesis) with varying mol% SiO$_2$. **A)** Pyridine vibrations region (1700-1400 cm^{-1}) **B)** Surface Zr-OH and Si-OH stretching vibration region (3800-3500 cm^{-1}).
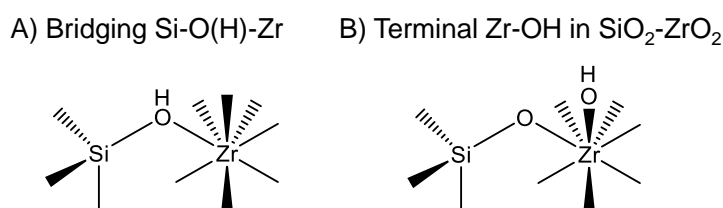
Scheme 3-1. Schematic representation of bridging OH and terminal OH group of Si-O-Zr in mixed oxide SiO$_2$-ZrO$_2$.

The model is derived from the considerations of Tanabe[10b], taking into account the coordination numbers of both cations and anions. According to this model, all oxygen anions are assumed to maintain the coordination number of the major oxide component. In contrast to that, the metal cations may retain the coordination number of their pure metal oxides for both major and minor component. This leads to an excess charge in a model structure. If the excess charge is negative, it has to be balanced by a proton generating a BAS. Accordingly,

a positive excess charge leads to the introduction of an oxygen vacancy, and hence to a LAS. The simultaneous occurrence of BAS and LAS, like here, may point to the existence of domains with varying concentrations of the constituents.[27] Note that such a model is in agreement with the Sanderson electronegativity concept[28] and the mixing rule.[29]

^{29}Si-NMR Spectroscopy
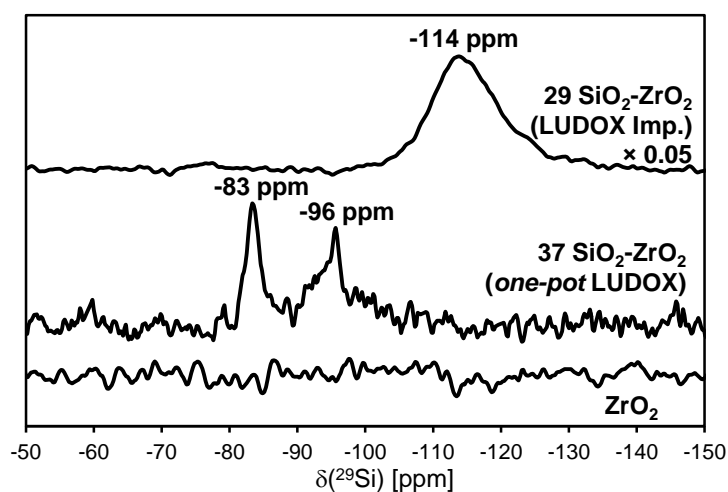
Figure 3-7. ^{29}Si-MAS-NMR spectra of ZrO$_2$, 37 SiO$_2$-ZrO$_2$ (*one-pot* hydrothermal) and 29 SiO$_2$-ZrO$_2$ (*Impregnation*).

The SiO$_2$-modified sample (**Figure 3-7**) prepared by the *one-pot* hydrothermal method (*e.g.* 37 SiO$_2$-ZrO$_2$ (H)) shows two peaks with chemical shifts of -83 ppm and -96 ppm, that represent a 2-fold (*Q2*) and 3-fold (*Q3*) coordination of Si-atoms as in Si(OSi)$_2$(OZr)$_2$ and Si(OSi)$_3$(OZr)$_1$ or Si(OSi)$_2$(OH)$_2$ and Si(OSi)$_3$(OH)$_1$, respectively.[14, 30] Si-O-H and Si-O-Zr bonds are not distinguishable in ^{29}Si-NMR.[22a] This allows us to conclude that SiO$_2$ and ZrO$_2$ exist in dispersed form in a mixed oxide. In contrast, the spectrum of the 29 SiO$_2$-ZrO$_2$ (Imp.) showed a broad signal at -114 ppm corresponding to *Q4*, the 4-fold coordination of siloxane bonds Si(OSi)$_4$. This point to the fact that the SiO$_2$ phase and the ZrO$_2$ phase are partially segregated. Thus, it is concluded that SiO$_2$ forms a mixed oxide phase with ZrO$_2$ through a hydrothermal synthesis, whereas it is only deposited onto the ZrO$_2$ support by the impregnation method. With increasing SiO$_2$ concentration, these peaks are shifted towards lower field, due to the coordination of Si with Si increases (**Figure A 3-1**).

3.3.2 Hydrodeoxygenation of stearic acid
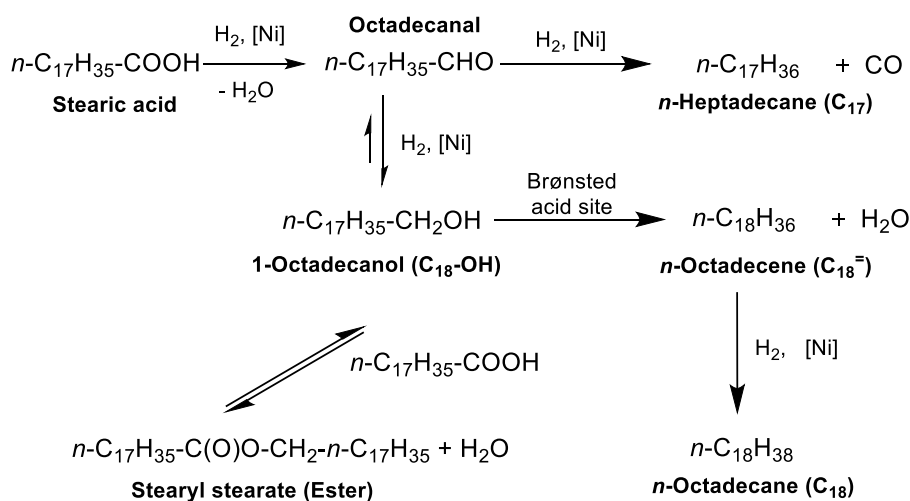
Scheme 3-2. Proposed reaction network for the hydrodeoxygenation of stearic acid, showing the decarbonylation route towards *n*-heptadecane (C$_{17}$), dehydration/hydrogenation to *n*-octadecane (C$_{18}$) and reversible esterification towards stearyl stearate.[6b, 7, 32]

Catalytic hydrodeoxygenation of stearic acid was carried out on the Ni/SiO$_2$-SiO$_2$ catalysts. As shown in **Figure 3-8**, the initial conversion of stearic acid on Ni/37 SiO$_2$-ZrO$_2$ (H) resulted in 1-octadecanol as primary product, formed by the hydrogenation of the fatty acid (**Figure 3-9, B**).[6a] Further conversion led to the appearance of secondary product, stearyl stearate ester, *n*-heptadecane (C$_{17}$) and *n*-octadecane (C$_{18}$). Stearyl stearate was formed through esterification of 1-octadecanol with stearic acid.[6b, 31] This reaction is reversible and stearyl stearate reached a maximum at 8 h and decayed afterwards until depletion after 20 h. Only alkane products, *n*-heptadecane and *n*-octadecane, remained after 24 h. *n*-Heptadecane was formed *via* dehydrogenation of the 1-octadecanol intermediate to octadecanal with subsequent decarbonylation, and *n*-octadecane was formed *via* dehydration of 1-octadecanol to 1-octadecene with subsequent hydrogenation (**Scheme 3-2**).
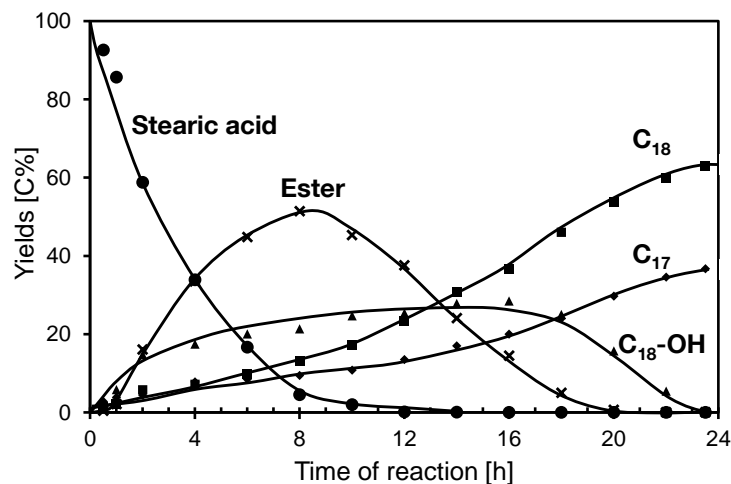
Figure 3-8. Product distribution for the hydrodeoxygenation of stearic acid over 10 wt% Ni/37 SiO$_2$-ZrO$_2$ (H) as a function of time, stearic acid (●), 1-octadecanol (▲), *n*-heptadecane (♦), *n*-octadecane (■) and stearyl stearate (×). Reaction conditions: stearic acid (0.5 g), 0.05 g 10 wt% Ni/37 SiO$_2$-ZrO$_2$ (H), dodecane (100 mL), 260 °C, p(H$_2$) = 40 bar, stirring at 600 rpm, 8 h.
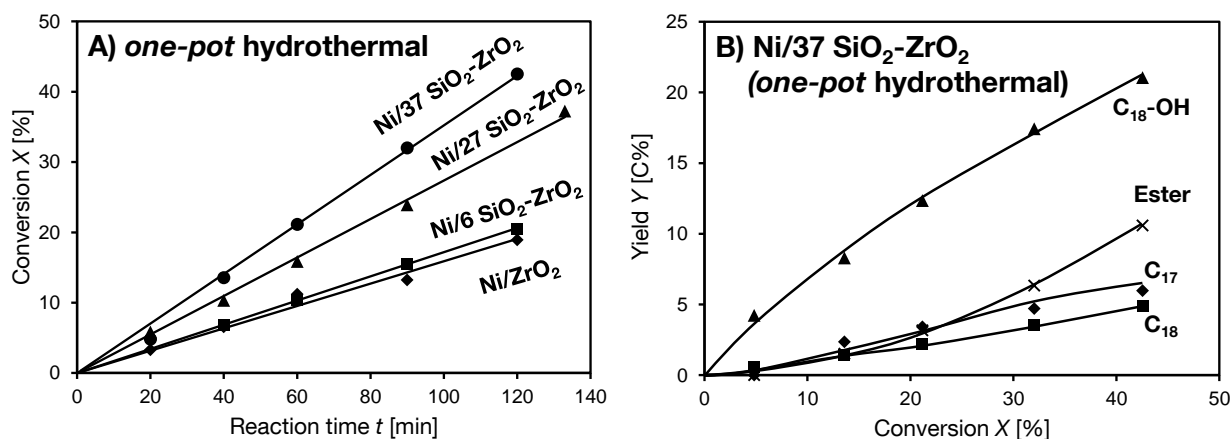
Figure 3-9. A) Conversion of stearic acid as a function of time. **B)** Yields of 1-octadecanol, stearyl stearate, *n*-heptadecane and *n*-octadecane over Ni/37 SiO$_2$-ZrO$_2$ (*one-pot* hydrothermal) as a function of stearic acid conversion. 1-octadecanol (▲), *n*-heptadecane (♦), *n*-octadecane (■) and stearyl stearate (×). Reaction conditions: stearic acid (0.5 g), Ni/SiO$_2$-ZrO$_2$ catalyst (10 wt% Ni, 0.05 g), dodecane (100 mL), 260 °C, p(H$_2$) = 40 bar, stirring at 600 rpm, 2 h.

Figure 3-10 shows the Turnover frequency (TOF) of stearic acid and the concentration of BAS as a function of SiO$_2$-content for Ni/ZrO$_2$–SiO$_2$ (H) catalysts. Ni/ZrO$_2$ has a TOF of 64 (conversion rate of 3.2 $m$mol·g$_{cat}^{-1}$·h^{-1}). With increasing SiO$_2$-content, the TOF increased. The TOF of 297 (conversion rate of 8.6 $m$mol·g$_{cat}^{-1}$·h^{-1}) for Ni/37 SiO$_2$-ZrO$_2$ (H) was the highest TOF (**Figure 3-9, A** and **Figure 3-10**), decreasing with further increasing SiO$_2$ content (**Table A 3-3**). This trend is in line with the variation of BAS concentrations

and the specific surface area of the catalysts. The conversion rate of stearic acid on Ni follows approximately the concentration of BAS from the SiO$_2$-ZrO$_2$ support (**Figure 3-10**), indicating a promotion of hydrogenation activity of Ni by close BAS. Similar observations were made for hydrodeoxygenation of phenolic substrates by Song *et al.*[11] Because the conversion of stearic acid can be synergistically enhanced by ZrO$_2$,[7] the markedly higher specific surface area may also contribute to the activity (**Figure A 3-2**). In contrast, hydrodeoxygenation of stearic acid over SiO$_2$-impregnated Ni/ZrO$_2$ catalysts showed a decrease of conversion rate with increasing SiO$_2$-content from 3.2 *m*mol·g$_{cat}^{-1}$·h^{-1} for Ni/ZrO$_2$ to 1.4 *m*mol·g$_{cat}^{-1}$·h^{-1} for Ni/29 SiO$_2$-ZrO$_2$ (Imp.) (**Figure A 3-3, A** and **Table A 3-4**). The products evolving with increasing stearic acid conversion is similar to that on Ni/ZrO$_2$. The decrease in activity is attributed to the SiO$_2$ partly covering ZrO$_2$, reducing so the accessible ZrO$_2$ surface.[6a, 7]
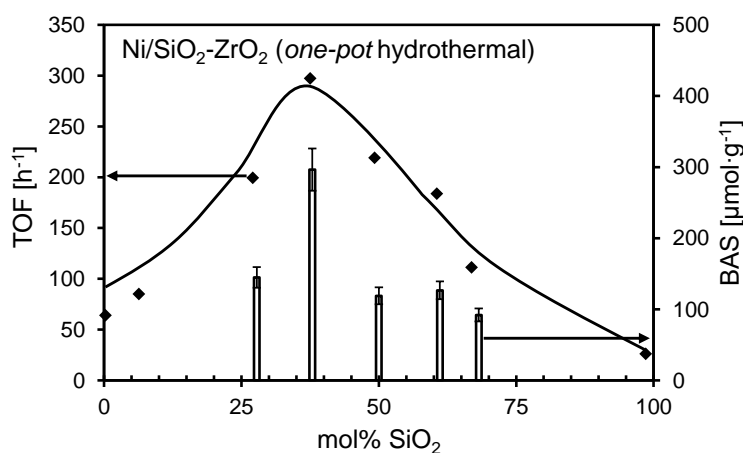
Figure 3-10. Turnover frequency (TOF) for the hydrodeoxygenation of stearic acid and concentration of Brønsted acid sites as a function of SiO$_2$-content in the Ni/SiO$_2$-ZrO$_2$ catalyst prepared by the hydrothermal method. Reaction conditions: stearic acid (0.5 g), Ni/SiO$_2$-ZrO$_2$ catalyst (10 wt% Ni, 0.05 g), dodecane (100 mL), 260 °C, *p*(H$_2$) = 40 bar, stirring at 600 rpm, 2 h.

It is noticeable that on Ni/ZrO$_2$ catalyst, *n*-heptadecane was the dominant hydrocarbon product at full conversion and the *n*-octadecane yield was negligible,[32] while on Ni/37 SiO$_2$-ZrO$_2$ (H), *n*-octadecane had a yield as high as 60%. Bare ZrO$_2$ only possesses LAS, whereas the presence of BAS in (H) catalysts enhanced the rate of 1-octadecanol dehydration, causing a shift in selectivity towards *n*-octadecane. This shift in product distribution from *n*-heptadecane to *n*-octadecane is advantageous from a carbon-economy point of view.[6a, 33] In **Figure 3-11** the rate constants for the dehydration of 1-octadecanol leading to

C_{18} and esterification of stearic acid with C_{18}-OH leading to stearyl stearate are shown. The rate constants for both reactions have a positive correlation with the BAS concentrations on the catalysts, indicating Brønsted acidic proton as the active site. Obviously, the conversion of stearic acid over Ni/37 SiO$_2$-ZrO$_2$ has the highest yield of *n*-octadecane, because it has the highest concentration of Brønsted acid sites.
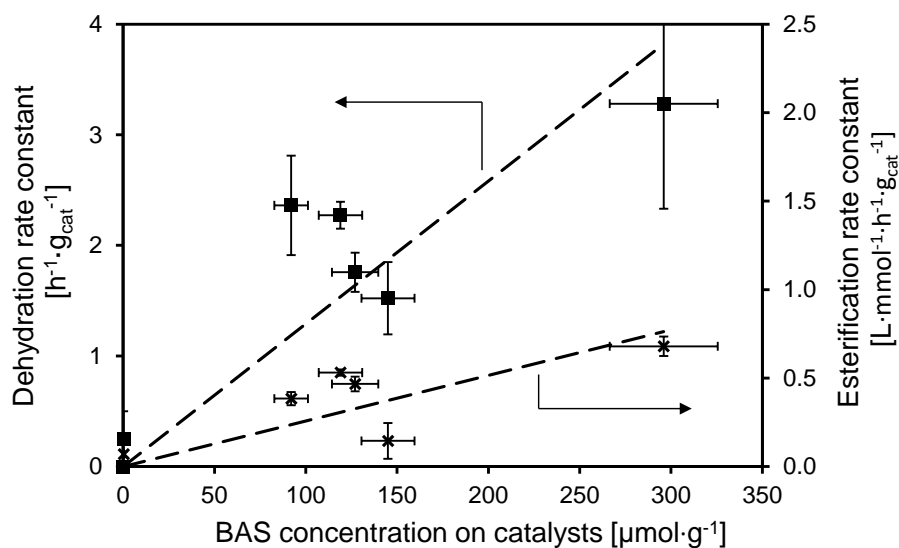
Figure 3-11. Rate constant for the dehydration of 1-octadecanol (■) and esterification of stearic acid and 1-octadecanol (×) normalized to catalyst weight as a function of concentration of BAS on Ni/SiO$_2$-ZrO$_2$ catalyst. Reaction conditions: stearic acid (0.5 g), Ni/SiO$_2$-ZrO$_2$ catalyst (10 wt% Ni, 0.05 g), dodecane (100 mL), 260 °C, p(H$_2$) = 40 bar, stirring at 600 rpm, 2 h.

3.4 Conclusions

Hydrothermal synthesis of SiO$_2$-ZrO$_2$ mixed oxides led to materials with a maximum in Brønsted acid site concentration at approximately 40 mol% of SiO$_2$ and 60 mol% ZrO$_2$. Brønsted acid sites are concluded to be induced by the substitution in oxide lattices differing in the coordination of the cations, Si^{4+} and Zr^{4+}. Differences in morphology resulted in high specific surface areas of these mixed oxides, having a spherical morphology with agglomerates of nano-layered materials. The higher concentration of Brønsted acid sites and higher specific surface area led to a maximum in the catalytic activity for stearic acid deoxygenation for Ni/37 SiO$_2$-ZrO$_2$. Remarkably, an increase in the rates of hydrogenation reactions by neighboring Brønsted acid sites and Ni particles was observed. While the high Brønsted acid

site concentration facilitates the dehydration of 1-octadecanol intermediate, which leads to an enhanced *n*-octadecane formation.

3.5 Experimental Section – Materials and Methods

3.5.1 Chemicals

All chemicals were purchased commercially: ZrO(NO$_3$)$_2$ × x H$_2$O (Sigma-Aldrich, 99%), urea (Sigma-Aldrich ACS reagent, 99.0-100.5%), LUDOX TM-40 (40 wt% SiO$_2$-suspension, Sigma-Aldrich), Ni(NO$_3$)$_2$·6 H$_2$O (Acros Organics, ≥98.5%), stearic acid (Sigma-Aldrich, ≥99.5% analytical standard), 1-octadecanol (Sigma-Aldrich, ≥99.5% Selectophore^{TM}), *n*-octadecane (Sigma-Aldrich, 99%), *n*-heptadecane (Sigma-Aldrich, 99%), dodecane (Sigma-Aldrich, ≥99%, *ReagentPlus*).

3.5.2 Catalyst preparation

Silica modified ZrO$_2$ supports with various SiO$_2$-content were prepared by two different methods (**Table 3-4**). For the first pathway, a hydrothermal synthesis route in the presence of ZrO$_2$ and a SiO$_2$ precursor was chosen. Various amount of LUDOX TM-40 (colloidal SiO$_2$-suspension), 44.4 g ZrO(NO$_3$)$_2$ • x H$_2$O and urea were dissolved in bi-distilled water according to **Table A 3-5** (**Appendix,** page 79). The solution was transferred to a stainless steel autoclave with a Teflon® liner. Herein, at 180 °C and autogenous pressure a precipitate was formed after 24 h. Therefore, this procedure is called *one-pot* hydrothermal method (H). After washing the precipitate with H$_2$O five times, it was dried overnight at 110 °C and then ground and calcined in synthetic air at 400 °C for 4 h at a heating rate of 2 °C·min^{-1} (flow rate: 100 mL·min^{-1}). The labeling of both catalysts as well as supports corresponds to the mol% of SiO$_2$, derived from Si elemental analysis by ICP-OES.

Table 3-4: Overview of all SiO$_2$-ZrO$_2$ supports prepared by two different methods.

Catalyst [a]	mol% SiO$_2$	mol% Si	mol% ZrO$_2$	mol% Zr
ZrO$_2$	<1	<1	100	33
6 SiO$_2$-ZrO$_2$ (H)	6	2.1	94	31
27 SiO$_2$-ZrO$_2$ (H)	27	9.0	73	24
37 SiO$_2$-ZrO$_2$ (H)	37	13	63	21
49 SiO$_2$-ZrO$_2$ (H)	49	16	51	17
61 SiO$_2$-ZrO$_2$ (H)	61	20	39	13
67 SiO$_2$-ZrO$_2$ (H)	67	22	33	11
SiO$_2$	99	33	<1	<1
4 SiO$_2$-ZrO$_2$ (Imp.)	4	1.4	96	32
16 SiO$_2$-ZrO$_2$ (Imp.)	16	5.5	83	28
29 SiO$_2$-ZrO$_2$ (Imp.)	29	9.7	71	24

[a] Number in the label is mol% SiO$_2$. (H) ≡ *one-pot* hydrothermal synthesis method; (Imp.) ≡ Impregnation method

For the second route, *monoclinic* ZrO$_2$ was impregnated with LUDOX TM-40 to prepare a mixed oxide enriched at the surface with SiO$_2$. For this, *monoclinic* ZrO$_2$ was prepared as shown previously [12a, 32] and LUDOX was added dropwise onto the powdered ZrO$_2$ with various amounts as shown in **Table A 3-6**. Subsequently, the SiO$_2$ *impregnated* ZrO$_2$ was suspended with water, stirred for 3 h at ambient temperature and dried overnight at 110 °C. This is called impregnation method (Imp.).

The 10 wt% supported Ni catalysts were prepared by the wet impregnation technique. The Ni metal precursor, Ni(NO$_3$)$_2$·6 H$_2$O (3.30 g), was dissolved in deionized H$_2$O, and the resultant solution was added dropwise into 6.0 g of the powdered support with stirring in ambient air. The slurry was further stirred for 4 h, followed by drying at 110 °C overnight. Subsequently, the ground solid was calcined in synthetic air (flow rate: 100 mL·min^{-1}) at 450 °C for 4 h (heating rate: 4 °C·min^{-1}) and reduced in H$_2$ flow (flow rate: 100 mL·min^{-1}) at 500 °C for 4 h (heating rate: 4 °C·min^{-1}).

3.5.3 Catalyst characterization

X-Ray powder diffraction (XRD) was performed on a Philips X'Pert Pro System equipped with a Cu Kα radiation source (40 kV/45 mA) with 1.08° min^{-1} in the 2 θ range of 5−70°. The crystal size of ZrO$_2$ was determined *via* Scherrer equation from full width at half maximum of the (111) diffraction peak of ZrO$_2$.[34]

N$_2$-sorption. The BET surface area was determined by adsorption-desorption with N$_2$ at -196 °C using the Sorptomatic 1990 series instrument. The sample was activated in vacuum at 250 °C for 2 h before measurement. In order to measure **H$_2$-chemisorption** in Thermo Scientific's Surfer instrument, the Ni based catalysts were reduced in H$_2$-flow at 450 °C for 1 h and then evacuated at 300 °C for 1 h. The H$_2$ adsorption isotherms accounting for both chemisorption and physisorption were measured at a pressure ranging from 9 to 400 *m*bar at 25 °C. Afterwards, the system was evacuated for 20 min to remove physisorbed H$_2$ and to obtain chemisorbed H$_2$ after subtraction. The concentration of chemisorbed hydrogen on the metal was determined by extrapolating the isotherm to zero H$_2$ pressure. The Ni dispersion was deduced by assuming an average surface Ni to H ratio of 1.

Temperature programmed desorption (TPD) of ammonia and carbon dioxide was carried out in a 6-fold parallel reactor system. The pressed samples (500-710 µm) were first activated in He at 500 °C for 1 h and loaded with the adsorbent NH$_3$ or CO$_2$ at a partial pressure of 1 *m*bar and 100 °C or 40 °C, respectively. The samples were then purged with He for 1 h in order to remove physisorbed species. After activation, the six samples were heated from 100-770 °C with a rate of 10 °C·min^{-1} to desorb NH$_3$ and from 40 to 700 °C to remove CO$_2$, and the signals were detected by a Balzers QME 200 mass spectrometer.

Atomic absorption spectroscopy (AAS) was used to determine the Ni content of the catalysts with a UNICAM 939 AA-Spectrometer. Prior to Ni determination, the catalysts were dissolved in boiling concentrated sulfuric acid. Si-content of the supports was obtained by **Inductively Coupled Plasma Optical Emission Spectrometry (ICP-OES)** using a HORIBA Jobin Yvon Ultima II spectrometer. In order to prepare the sample for measurement, the finely ground powder was digested in Merck's Spectromelt A14 (Li$_2$B$_4$O$_7$, LiBO$_2$).

High Resolution Scanning Electron Microscopy (HR-SEM) of the SiO$_2$ modified supports was performed with a JOEL JSM-7500F SEM. The finely ground samples were

mounted on a multi-sample-holder by standard preparation technique and measured with a secondary electron ionization detector (SEI).

IR spectroscopy of adsorbed pyridine (*py*-IR) was performed on a Thermo Fisher Nicolet 5700 IR spectrometer at a resolution of 4 cm^{-1} with 120 scans in the range of 1000-4000 cm^{-1} equipped with CaF$_2$ windows. For the adsorption measurements, the samples of ZrO$_2$ with various content of SiO$_2$ were pressed into a self-supporting disc (wafer) and mounted on the sample holder. The samples were activated under vacuum ($p = 10^{-6}$ *m*bar) at 450 °C for 1 h (heating ramp: 10 K·min^{-1}). As soon as the sample cooled to 150 °C, a spectrum of the activated sample was taken. Subsequently, adsorption of pyridine was performed at 0.1 *m*bar for 30 min until saturation/equilibration of the surface was reached and the peak area of the IR signal remained constant. After physisorbed pyridine was removed by evacuation ($p = 10^{-6}$ *m*bar) at 150 °C, another spectrum was recorded. Finally, a spectrum was taken after desorption at 450 °C for 30 min ($p = 10^{-6}$ *m*bar). The IR spectra of adsorbed pyridine were obtained by subtracting the spectrum of the activated sample, and then were normalized by the weight of the sample wafer. For quantification, the spectra were analyzed according to the procedure described earlier, using molar integral extinction coefficients of 0.73 cm·µmol^{-1} (BAS) and 0.96 cm·µmol^{-1} (LAS).[35]

Solid state ^{29}Si MAS NMR spectroscopy measurements (^{29}Si-NMR) of SiO$_2$-ZrO$_2$ samples were obtained using a Bruker Advance 300 MHz multinuclear FT spectrometer ($B = 7.05$ T) at the corresponding ^{29}Si resonance frequency of 59.6 MHz. The powdered samples were fully hydrated before packing them into a 4 mm ZrO$_2$ pencil type rotor. Spinning at a speed of 10 kHz, 7000-8000 scans were recorded using a single-pulse technique with a pulse length of 6 µs and a repetition time of 10 s. The external standard Si[Si(CH$_3$)$_3$]$_4$ with a chemical shift of 9.8 ppm for ^{29}Si (*versus* TMS) was used.

3.5.4 Measurement of the catalytic activity

In order to test the described catalyst systems, stearic acid (0.5 g) and the corresponding catalyst (0.05 g) were first loaded into the autoclave reactor (Parr, 300 mL) with dodecane (100 mL), and then purged three times with H$_2$. The reaction was carried out at 260 °C under 40 bar of H$_2$ for 2 h at a stirring speed of 600 rpm. *In situ* samples were drawn after 20, 40, 60, 90 and 120 min, and were analyzed by Agilent 7890B GC system, equipped

with a flame ionization detector (FID) and Agilent 5977 MS detector, using a HP-5 capillary column (30 m, 0.32 mm inner diameter, 0.25 µm film). Reproducibility of the rates was better than ±5% for all experiments.

Conversion = (weight of converted reactant / weight of the starting reactant) × 100%. Yield (C%) = (C atoms in each product / C atoms in the starting reactant) × 100%. Selectivity (C%) = (C atoms in each product/sum of C atoms in all the products) × 100%. Turnover frequency (TOF) is the reaction rate normalized by accessible surface Ni atoms, which were determined by chemisorption of hydrogen or concentration of BAS, which was determined by *py*-IR (where applicable). TOF = mole of converted reactant / mole of accessible Ni on the catalyst's surface or mole of converted reactant / concentration of BAS. Rate of dehydration = Δ yield of C$_{18}$ / Δ time). Rate constant of dehydration = rate of dehydration / concentration of 1-octadecanol.

3.6 Acknowledgements

3.7 Contributions

Sebastian Foraita planned the experiments, synthesized the catalysts, carried out the reactions, characterized the materials, analyzed the results and wrote the manuscript. Yue

3.8   Appendix

Table A 3-1. Physicochemical properties of SiO$_2$ modified ZrO$_2$ supports prepared by *one-pot* hydrothermal method.

Support/ modification	S_{BET} [m^2·g^{-1}]	mol% SiO$_2$ [a]	Grain size of ZrO$_2$ [b] [nm]	Concentration of acids sites [c] [*m*mol·g^{-1}]	Concentration of basic sites [d] [*m*mol·g^{-1}]
m-ZrO$_2$	123	0.2	7.1	0.23	0.091
One-pot hydrothermal					
6 SiO$_2$-ZrO$_2$	171	6.3	4.3	0.36	0.25
27 SiO$_2$-ZrO$_2$	176	27	8.7	0.93	0.05
37 SiO$_2$-ZrO$_2$	235	37	2.5	0.73	0.03
49 SiO$_2$-ZrO$_2$	175	49		0.44	0
61 SiO$_2$-ZrO$_2$	140	61		0.42	0
67 SiO$_2$-ZrO$_2$	130	67		0.34	0
SiO$_2$	81	99		0	0

[a] Derived from Si-ICP-OES analysis. [b] Determined from ZrO$_2$ (111) reflex *via* Scherrer equation. [c] Determined by TPD of NH$_3$. [d] Determined by TPD of CO$_2$.

Table A 3-2. Physicochemical properties of SiO$_2$ modified ZrO$_2$ supports (impregnation).

Support/ modification	S_{BET} [m^2·g^{-1}]	mol% SiO$_2$ [a]	Concentration of acids sites [b] [$m$mol·g^{-1}]	Concentration of basic sites [c] [$m$mol·g^{-1}]
m-ZrO$_2$	123	0.2	0.23	0.091
Impregnation SiO$_2$				
4 SiO$_2$-ZrO$_2$	111	4.1	0.26	0.11
16 SiO$_2$-ZrO$_2$	125	16	0.22	0.10
29 SiO$_2$-ZrO$_2$	130	29	0.19	0.08

[a] Derived from Si-ICP-OES analysis. [b] Determined by TPD of NH$_3$. [c] Determined by TPD of CO$_2$.
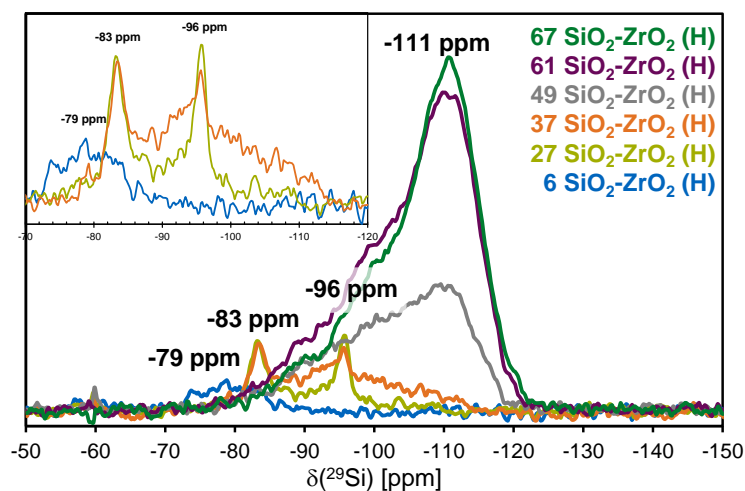
Figure A 3-1. ^{29}Si-MAS-NMR spectra of SiO$_2$-ZrO$_2$ (*one-pot* hydrothermal) with increasing mol%-SiO$_2$. Details of 6-, 27- and 37 SiO$_2$ZrO$_2$ as an enlargement of *Q1*, *Q2* and *Q3* range (top left).

Table A 3-3. Comparison of stearic acid conversion over SiO$_2$-ZrO$_2$-supported Ni catalysts.[a]

Catalyst/ Modification	Rate [$m$mol·g$_{cat}^{-1}$·h^{-1}]	Conv. [%]	Selectivity [%]				
			C$_{17}$	C$_{18}$	C$_{17}$-CHO	C$_{18}$-OH	Ester
Ni/ZrO$_2$	3.2	19	10	-	-	90	-
one-pot hydrothermal							
Ni/6 SiO$_2$-ZrO$_2$	3.6	21	8.0	-	-	92	-
Ni/27 SiO$_2$-ZrO$_2$	6.1	39	6.4	8.7	-	77	7.9
Ni/37 SiO$_2$-ZrO$_2$	8.6	43	14	12	-	49	25
Ni/49 SiO$_2$-ZrO$_2$	7.1	41	13	8.5	0.6	55	24
Ni/61 SiO$_2$-ZrO$_2$	6.6	42	11	6.9	0.4	60	21
Ni/67 SiO$_2$-ZrO$_2$	4.7	27	15	9.2	0.7	56	19
Ni/SiO$_2$	1.7	9.9	12	2.1	1.9	79	5.0

[a] Reaction conditions: stearic acid (0.5 g), Ni/SiO$_2$-ZrO$_2$ catalyst (10 wt% Ni, 0.05 g), dodecane (100 mL), 260 °C, p(H$_2$) = 40 bar, stirring at 600 rpm, 2 h.
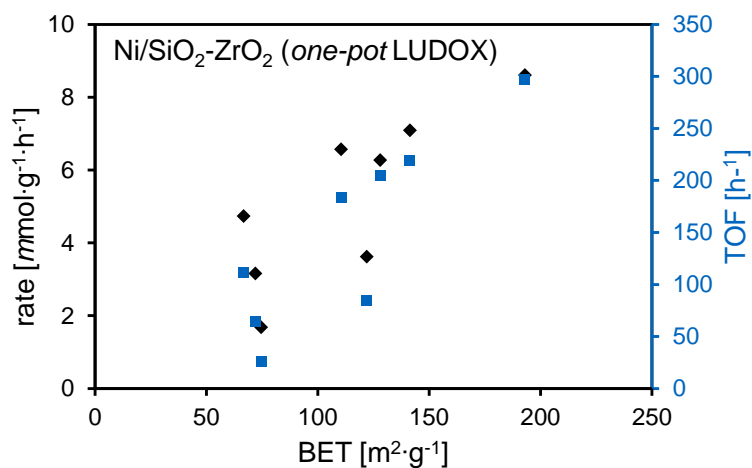
Figure A 3-2. Reaction rate and turn over Frequency (TOF) for the conversion of stearic acid as a function of specific surface area (BET). Reaction conditions: stearic acid (0.5 g), Ni/SiO$_2$-ZrO$_2$ catalyst (10 wt%, 0.05 g), dodecane (100 mL), 260 °C, p(H$_2$) = 40 bar.
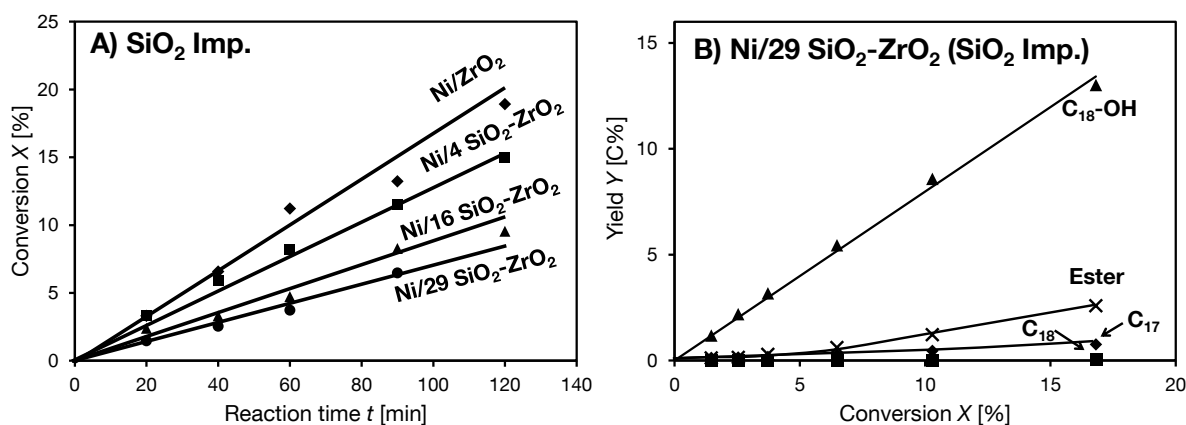
Figure A 3-3. A) Conversion of stearic acid as a function of time. **B)** Yields of 1-octadecanol, stearyl stearate, *n*-heptadecane and *n*-octadecane over Ni/29 SiO$_2$-ZrO$_2$ (SiO$_2$ Impregnation) as a function of stearic acid conversion. 1-octadecanol (▲), *n*-heptadecane (♦), *n*-octadecane (■) and stearyl stearate (×). Reaction conditions: stearic acid (0.5 g), Ni/SiO$_2$-ZrO$_2$ catalyst (10 wt% Ni, 0.05 g), dodecane (100 mL), 260 °C, $p(H_2)$ = 40 bar, stirring at 600 rpm, 2 h.

Table A 3-4. Comparison of stearic acid conversion over SiO$_2$-*impregnated* ZrO$_2$-supported Ni catalysts.[a]

Catalyst/	Rate	Conv.	Selectivity [%]			
Modification	[$m$mol·g$_{cat}^{-1}$·h^{-1}]	[%]	C$_{17}$	C$_{18}$	C$_{18}$-OH	Ester
Ni/ZrO$_2$	3.2	19	10	-	90	-
Impregnation SiO$_2$						
Ni/4 SiO$_2$-ZrO$_2$	2.3	15	4.9	0.3	91	3.6
Ni/16 SiO$_2$-ZrO$_2$	1.6	9.0	3.2	0.2	88	9.1
Ni/29 SiO$_2$-ZrO$_2$	1.4	10	4.4	0.3	82	13

[a] Reaction conditions: stearic acid (0.5 g), Ni/SiO$_2$-ZrO$_2$ catalyst (10 wt% Ni, 0.05 g), dodecane (100 mL), 260 °C, $p(H_2)$ = 40 bar, stirring at 600 rpm, 2 h.

Table A 3-5. Detailed amounts of LUDOX (SiO$_2$), ZrO(NO$_3$)$_2$ and urea used to synthesize the supports with *one-pot* hydrothermal method.

Support	m[ZrO(NO$_3$)$_2$ x H$_2$O]	n(Zr^{4+})	m(LUDOX)	m(SiO$_2$)	n(SiO$_2$)	m(urea)	n(urea)
	[g]	[mol]	[g]	[g]	[mol]	[g]	[mol]
m-ZrO$_2$	44.4	0.13	0	0	0	115	1.92
6 SiO$_2$-ZrO$_2$	44.4	0.13	1.29	0.52	0.0086	115	1.92
27 SiO$_2$-ZrO$_2$	44.4	0.13	7.08	2.83	0.047	115	1.92
37 SiO$_2$-ZrO$_2$	44.4	0.13	16.09	6.44	0.107	115	1.92
49 SiO$_2$-ZrO$_2$	44.4	0.13	22.28	8.91	0.148	115	1.92
61 SiO$_2$-ZrO$_2$	44.4	0.13	31.66	12.66	0.211	115	1.92
67 SiO$_2$-ZrO$_2$	44.4	0.13	67.98	27.19	0.453	115	1.92
SiO$_2$	0	0	15.74	6.30	0.105	115	1.92

Table A 3-6. Detailed amounts of *m*-ZrO$_2$ and LUDOX used for SiO$_2$ impregnation of ZrO$_2$.

Support	m(*m*-ZrO$_2$)	m(LUDOX)	m(SiO$_2$)
	[g]	[g]	[g]
4 SiO$_2$-ZrO$_2$	6.0	0.32	0.13
16 SiO$_2$-ZrO$_2$	6.0	1.60	0.51
29 SiO$_2$-ZrO$_2$	6.0	3.21	1.30

3.9   References

1. Huber, G. W.; Iborra, S.; Corma, A., Synthesis of Transportation Fuels from Biomass: Chemistry, Catalysts, and Engineering. *Chem. Rev.* **2006,** *106*, 4044-4098.
2. Jakkula, J.; Niemi, V.; Nikkonen, J.; Purola, V.-M.; Myllyoja, J.; Aalto, P.; Lehtonen, J.; Alopaeus, V. Process for producing a hydrocarbon component of biological origin. EP1396531A2, 2004.

3. (a) Zhao, C.; Bruck, T.; Lercher, J. A., Catalytic deoxygenation of microalgae oil to green hydrocarbons. *Green Chem.* **2013,** *15*, 1720-1739; (b) Furimsky, E., Chemistry of Catalytic Hydrodeoxygenation. *Catal. Rev.* **1983,** *25*, 421-458.

4. (a) Snåre, M.; Kubičková, I.; Mäki-Arvela, P.; Eränen, K.; Murzin, D. Y., Heterogeneous Catalytic Deoxygenation of Stearic Acid for Production of Biodiesel. *Ind. Eng. Chem. Res.* **2006,** *45*, 5708-5715; (b) Snåre, M.; Kubičková, I.; Mäki-Arvela, P.; Chichova, D.; Eränen, K.; Murzin, D. Y., Catalytic deoxygenation of unsaturated renewable feedstocks for production of diesel fuel hydrocarbons. *Fuel* **2008,** *87*, 933-945; (c) Immer, J. G.; Kelly, M. J.; Lamb, H. H., Catalytic reaction pathways in liquid-phase deoxygenation of C18 free fatty acids. *Appl. Catal., A* **2010,** *375*, 134-139.

5. (a) Gosselink, R. W.; Stellwagen, D. R.; Bitter, J. H., Tungsten-Based Catalysts for Selective Deoxygenation. *Angew. Chem., Int. Ed.* **2013,** *52*, 5089-5092; (b) Hollak, S. A. W.; Gosselink, R. W.; van Es, D. S.; Bitter, J. H., Comparison of Tungsten and Molybdenum Carbide Catalysts for the Hydrodeoxygenation of Oleic Acid. *ACS Catal.* **2013,** *3*, 2837-2844.

6. (a) Peng, B.; Yuan, X.; Zhao, C.; Lercher, J. A., Stabilizing Catalytic Pathways via Redundancy: Selective Reduction of Microalgae Oil to Alkanes. *J. Am. Chem. Soc.* **2012,** *134*, 9400-9405; (b) Peng, B.; Yao, Y.; Zhao, C.; Lercher, J. A., Towards Quantitative Conversion of Microalgae Oil to Diesel-Range Alkanes with Bifunctional Catalysts. *Angew. Chem., Int. Ed.* **2012,** *51*, 2072-2075.

7. Peng, B.; Zhao, C.; Kasakov, S.; Foraita, S.; Lercher, J. A., Manipulating Catalytic Pathways: Deoxygenation of Palmitic Acid on Multifunctional Catalysts. *Chem. - Eur. J.* **2013,** *19*, 4732-4741.

8. Xu, J.; Zheng, A.; Yang, J.; Su, Y.; Wang, J.; Zeng, D.; Zhang, M.; Ye, C.; Deng, F., Acidity of Mesoporous MoO$_x$/ZrO$_2$ and WO$_x$/ZrO$_2$ Materials: A Combined Solid-State NMR and Theoretical Calculation Study. *J. Phys. Chem. B* **2006,** *110*, 10662-10671.

9. (a) Zhao, Q.; Shih, W. H.; Chang, H. L.; Andersen, P., The effect of curing on the thermal stability of Si-doped ZrO$_2$ powders. *Appl. Catal., A* **2004,** *262*, 215-221; (b) Chandradass, J.; Han, K.-S.; Bae, D.-s., Synthesis and characterization of zirconia- and silica-doped zirconia nanopowders by oxalate processing. *J. Mater. Process. Technol.* **2008,** *206*, 315-321; (c) Chen, S.-G.; Yin, Y.-S.; Wang, D.-P., Formation of Ring-Like Si–O–Zr Bonds at Intergranular Interfaces in Silica-Doped Zirconia. *J. Am. Ceram. Soc.* **2005,** *88*, 1041-1045; (d) Lecarpentier, S.; van Gestel, J.; Thomas, K.; Gilson, J.-P.; Houalla, M., Influence of W loading on the environment of Si in WO$_3$/ZrO$_2$–SiO$_2$ catalysts. *Appl. Catal., A* **2010,** *374*, 137-141.

10. (a) Kung, H. H., Formation of new acid sites in dilute oxide solid solutions: A predictive model. *J. Solid State Chem.* **1984,** *52*, 191-196; (b) Tanabe, K.; Sumiyoshi, T.; Shibata,

K.; Kiyoura, T.; Kitagawa, J., New hypothesis regarding the surface acidity of binary metal oxides. *Bull. Chem. Soc. Jpn.* **1974,** *47*, 1064-1066.

11. Song, W.; Liu, Y.; Baráth, E.; Zhao, C.; Lercher, J. A., Synergistic effects of Ni and acid sites for hydrogenation and C-O bond cleavage of substituted phenols. *Green Chem.* **2015,** *17*, 1204-1218.

12. (a) Li, W.; Huang, H.; Li, H.; Zhang, W.; Liu, H., Facile Synthesis of Pure Monoclinic and Tetragonal Zirconia Nanoparticles and Their Phase Effects on the Behavior of Supported Molybdena Catalysts for Methanol-Selective Oxidation. *Langmuir* **2008,** *24*, 8358-8366; (b) Schmid, H. K., Quantitative Analysis of Polymorphic Mixes of Zirconia by X-ray Diffraction. *J. Am. Ceram. Soc.* **1987,** *70*, 367-376; (c) del Monte, F.; Larsen, W.; Mackenzie, J. D., Stabilization of Tetragonal ZrO$_2$ in ZrO$_2$–SiO$_2$ Binary Oxides. *J. Am. Ceram. Soc.* **2000,** *83*, 628-634; (d) Ko, J.-B.; Lee, S. W.; Kim, D. E.; Kim, Y. U.; Li, G.; Lee, S. G.; Chang, T.-S.; Kim, D.; Joo, Y. L., Fabrication of SiO$_2$-ZrO$_2$ composite fiber mats via electrospinning. *J. Porous Mater.* **2006,** *13*, 325-330.

13. Guimon, C.; Auroux, A.; Romero, E.; Monzon, A., Acetylene hydrogenation over Ni-Si-Al mixed oxides prepared by sol-gel technique. *Appl. Catal., A* **2003,** *251*, 199-214.

14. Rodríguez Avendaño, R. G.; de los Reyes, J. A.; Montoya, J. A.; Viveros, T., Effect of Synthesis Parameters on Sol–Gel Silica Modified by Zirconia. *J. Sol-Gel Sci. Technol.* **2005,** *33*, 133-138.

15. Faria, E. A.; Marques, J. S.; Dias, I. M.; Andrade, R. D. A.; Suarez, P. A. Z.; Prado, A. G. S., Nanosized and reusable SiO$_2$/ZrO$_2$ catalyst for highly efficient biodiesel production by soybean transesterification. *J. Braz. Chem. Soc.* **2009,** *20*, 1732-1737.

16. (a) Rhodes, M. D.; Bell, A. T., The effects of zirconia morphology on methanol synthesis from CO and over catalysts: Part I. Steady-state studies. *J. Catal.* **2005,** *233*, 198-209; (b) Rhodes, M. D.; Pokrovski, K. A.; Bell, A. T., The effects of zirconia morphology on methanol synthesis from CO and H$_2$ over Cu/ZrO$_2$ catalysts: Part II. Transient-response infrared studies. *J. Catal.* **2005,** *233*, 210-220.

17. Yamaguchi, T.; Morita, T.; Salama, T.; Tanabe, K., Surface properties of ZrO$_2$ dispersed on SiO$_2$. *Catal. Lett.* **1990,** *4*, 1-6.

18. (a) Jentys, A.; Pham, N. H.; Vinek, H., Nature of hydroxy groups in MCM-41. *J. Chem. Soc., Faraday Trans.* **1996,** *92*, 3287-3291; (b) Travert, A.; Vimont, A.; Sahibed-Dine, A.; Daturi, M.; Lavalley, J.-C., Use of pyridine CH(D) vibrations for the study of Lewis acidity of metal oxides. *Appl. Catal., A* **2006,** *307*, 98-107; (c) Parry, E. P., An infrared study of pyridine adsorbed on acidic solids. Characterization of surface acidity. *J. Catal.* **1963,** *2*, 371-379; (d) Ouyang, F.; Nakayama, A.; Tabada, K.; Suzuki, E., Infrared Study of a Novel Acid-Base Site on ZrO$_2$ by Adsorbed Probe Molecules. I. Pyridine, Carbon Dioxide, and Formic Acid Adsorption. *J. Phys. Chem. B* **2000,** *104*, 2012-2018.

19. Zaki, M. I.; Hasan, M. A.; Al-Sagheer, F. A.; Pasupulety, L., In situ FTIR spectra of pyridine adsorbed on SiO$_2$-Al$_2$O$_3$, TiO$_2$, ZrO$_2$ and CeO$_2$: general considerations for the identification of acid sites on surfaces of finely divided metal oxides. *Colloids Surf., A* **2001,** *190*, 261-274.

20. Gallei, E.; Eisenbach, D., Infrared internal reflection and transmission spectra of synthetic X and Y zeolites containing Na$^+$, NH$_4^+$ and Ca^{2+} cations. *J. Catal.* **1975,** *37*, 474-485.

21. (a) Jacobs, P. A.; Von Ballmoos, R., Framework hydroxyl groups of H-ZSM-5 zeolites. *J. Phys. Chem.* **1982,** *86*, 3050-3052; (b) Boronat, M.; Corma, A., Factors Controlling the Acidity of Zeolites. *Catal. Lett.* **2015,** *145*, 162-172; (c) Knözinger, H.; Huber, S., IR spectroscopy of small and weakly interacting molecular probes for acidic and basic zeolites. *J. Chem. Soc., Faraday Trans.* **1998,** *94*, 2047-2059.

22. (a) Gao, X.; Wachs, I. E., Titania–silica as catalysts: molecular structural characteristics and physico-chemical properties. *Catal. Today* **1999,** *51*, 233-254; (b) Galan-Fereres, M.; Alemany, L. J.; Mariscal, R.; Banares, M. A.; Anderson, J. A.; Fierro, J. L. G., Surface Acidity and Properties of Titania-Silica Catalysts. *Chem. Mater.* **1995,** *7*, 1342-1348.

23. Pokrovski, K. A.; Bell, A. T., Effect of dopants on the activity of Cu/M$_{0.3}$Zr$_{0.7}$O$_2$ (M = Ce, Mn, and Pr) for CO hydrogenation to methanol. *J. Catal.* **2006,** *244*, 43-51.

24. (a) Hattori, H.; Itoh, M.; Tanabe, K., The nature of active sites on TiO$_2$ and TiO$_2$-SiO$_2$ for the isomerization of butenes. *J. Catal.* **1975,** *38*, 172-178; (b) Gionco, C.; Paganini, M. C.; Giamello, E.; Burgess, R.; Di Valentin, C.; Pacchioni, G., Paramagnetic Defects in Polycrystalline Zirconia: An EPR and DFT Study. *Chem. Mater.* **2013,** *25*, 2243-2253.

25. Kataoka, T.; Dumesic, J. A., Acidity of unsupported and silica-supported vanadia, molybdena, and titania as studied by pyridine adsorption. *J. Catal.* **1988,** *112*, 66-79.

26. Liu, Z. F.; Tabora, J.; Davis, R. J., Relationships between Microstructure and Surface Acidity of Ti-Si Mixed Oxide Catalysts. *J. Catal.* **1994,** *149*, 117-126.

27. Shen, Y., A new hypothesis of micro-region acid sites regarding the surface acidity of binary oxides. *RSC Adv.* **2012,** *2*, 5957-5960.

28. (a) Tanabe, K.; Misono, M.; Ono, Y.; Hattori, H., *New Solid Acids and Bases*. Kodansha and Elsevier: Tokyo and Amsterdam, 1989; Vol. 51; (b) Sanderson, R. T., *Chemical Bonds and Bond Energy*. 2nd ed.; Academic Press: New York, 1976; Vol. 21; (c) Tanabe, K., Solid Acid and Base Catalysts. In *Catal. Sci. Technol.*, Anderson, J. R.; Boudart, M., Eds. Springer: Berlin, 1981; Vol. 2, pp 231-273.

29. (a) Vinek, H.; Noller, H.; Ebel, M.; Schwarz, K., X-ray photoelectron spectroscopy and heterogeneous catalysis, with elimination reactions as an example. *J. Chem. Soc., Faraday Trans. 1* **1977,** *73*, 734-746; (b) Lercher, J. A.; Noller, H., Infrared

spectroscopic study of hydroxyl group acid strength of silica, alumina, and magnesia mixed oxides. *J. Catal.* **1982,** *77*, 152-158.

30. (a) Anderson, J. A.; Fergusson, C.; Rodríguez-Ramos, I.; Guerrero-Ruiz, A., Influence of Si/Zr ratio on the formation of surface acidity in silica-zirconia aerogels. *J. Catal.* **2000,** *192*, 344-354; (b) Wang, Z.; Jiang, Y.; Hunger, M.; Baiker, A.; Huang, J., Catalytic Performance of Brønsted and Lewis Acid Sites in Phenylglyoxal Conversion on Flame-Derived Silica-Zirconia. *ChemCatChem* **2014,** *6*, 2970-2975.

31. (a) Nijhuis, T. A.; Beers, A. E. W.; Kapteijn, F.; Moulijn, J. A., Water removal by reactive stripping for a solid-acid catalyzed esterification in a monolithic reactor. *Chem. Eng. Sci.* **2002,** *57*, 1627-1632; (b) Corma, A., Inorganic Solid Acids and Their Use in Acid-Catalyzed Hydrocarbon Reactions. *Chem. Rev.* **1995,** *95*, 559-614.

32. Foraita, S.; Fulton, J. L.; Chase, Z. A.; Vjunov, A.; Xu, P.; Baráth, E.; Camaioni, D. M.; Zhao, C.; Lercher, J. A., Impact of the Oxygen Defects and the Hydrogen Concentration on the Surface of Tetragonal and Monoclinic ZrO$_2$ on the Reduction Rates of Stearic Acid on Ni/ZrO$_2$. *Chem. - Eur. J.* **2015,** *21*, 2423-2434.

33. Mäki-Arvela, P.; Kubickova, I.; Snåre, M.; Eränen, K.; Murzin, D. Y., Catalytic Deoxygenation of Fatty Acids and Their Derivatives. *Energy Fuels* **2006,** *21*, 30-41.

34. Xu, G.; Zhang, Y.-W.; Liao, C.-S.; Yan, C.-H., Doping and grain size effects in nanocrystalline ZrO$_2$-Sc$_2$O$_3$ system with complex phase transitions: XRD and Raman studies. *Phys. Chem. Chem. Phys.* **2004,** *6*, 5410 - 5418.

35. Maier, S. M.; Jentys, A.; Lercher, J. A., Steaming of Zeolite BEA and Its Effect on Acidity: A Comparative NMR and IR Spectroscopic Study. *J. Phys. Chem. C* **2011,** *115*, 8005-8013.

Chapter 4

Hydrodeoxygenation of Stearic Acid on bimetallic Ni$_x$Cu$_{1-x}$/ZrO$_2$

A manuscript with the content of the following chapter will be submitted to *ChemCatChem* for publication. Contributions from colleagues in addition to the author of this thesis are stated at the end of this chapter (page 103).

The physical or chemical mixture of Ni and Cu metal supported on ZrO$_2$ led to catalysts converting stearic acid to long chain alkanes more efficiently than monometallic Ni/ZrO$_2$.
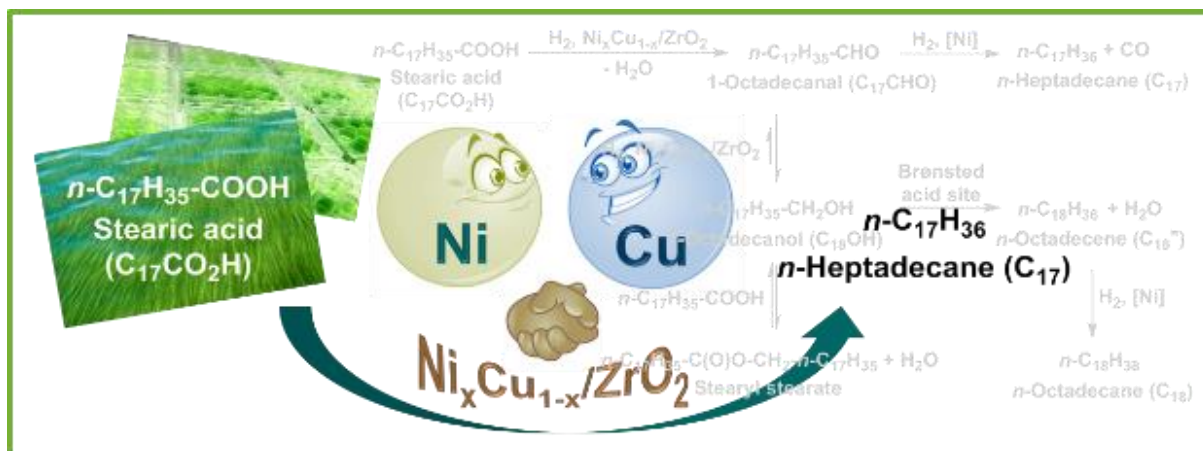
Keywords: Hydrodeoxygenation • Bimetallic Catalysts• Alloy • Ni Cu • ZrO$_2$ • Stearic acid

4.1   Abstract

Hydrodeoxygenation of stearic acid to *n*-heptadecane on Ni/ZrO$_2$ proceeds *via* hydrodeoxygenation of stearic acid to octadecanal with subsequent decarbonylation of the aldehyde to *n*-heptadecane. The addition of Cu to Ni/ZrO$_2$ enhanced the total reaction rate.

This effect is seen for a physical mixture with Cu/ZrO_2 and for the ZrO_2 supported Ni_xCu_{1-x} alloy. Cu/ZrO_2 was significantly more active for the hydrodeoxygenation of stearic acid to 1-octadecanol than Ni/ZrO_2. Decarbonylation of octadecanal that is in equilibrium with 1-octadecanol proceeded, however, with a much higher rate on Ni/ZrO_2 or Ni_xCu_{1-x}/ZrO_2. The combination of the higher hydrodeoxygenation of the acid to the aldehyde or alcohol and the high rate of elimination of water on Ni or Ni_xCu_{1-x} lead to the superior properties of the new catalyst.

4.2   Introduction

Microalgae are envisioned as the optimal raw material for producing third generation biofuels, because they are rich in lipids, provide rapid growth rates and are independent of arable land.[1] In order to obtain molecules in the diesel and kerosene range, the triglycerides need to be cleaved and deoxygenated. The commercial applicability of hydrotreating vegetable oils has been demonstrated by the NExBTL process (Neste Oil, Porvoo, 340 kt·a^{-1}) utilizing sulfide $NiMo/Al_2O_3$ catalysts.[2] Although such a process can use the existing infrastructure, the sulfide catalysts are disadvantageous for the conversion of triglyceride feedstocks that are virtually free of sulfur, because leaching of the sulfide catalysts leads to deactivation of the catalyst and contamination of the product stream.[3] Supported noble metals such as Ru, Pd and Pt catalysts offer high activity and selectivity for hydrodeoxygenation of triglycerides and fatty acids without catalyst leaching, but the use of such catalysts is economically challenging due to the high cost of such precious metals.[4] Other catalysts reported have been based on tungsten carbide. However, their activity was significantly lower than that of commercial hydrotreating catalysts ($NiMo/Al_2O_3$).[5]

Therefore, two types of novel sulfur-free Ni based catalysts were developed in order to directly convert microalgae oil quantitatively to diesel-range hydrocarbons at 260 °C and 40 bar H_2.[6] After fast hydrogenolysis of microalgae oil (triglycerides) into propane and fatty acids, the latter are hydrodeoxygenated into alkanes.[6a]

Stearic acid is one of the most abundant fatty acids in a representative microalgae oil and therefore used as a model compound.[6b] Its reductive conversion on Ni/ZrO_2 occurs *via* two redundant pathways – either by Ni alone or synergistically enhanced by Ni and the ZrO_2 support. On Ni, stearic acid is reduced to the alkane by hydrodeoxygenation and subsequent

decarbonylation *via* the aldehyde. Oxygen defect sites of ZrO_2 enable the combined adsorption and deoxygenation of fatty acid and the abstraction of α-H, leading to the formation of a ketene intermediate and the elimination of H_2O.[7] This ketene is in turn hydrogenated to aldehyde on Ni and subsequently decarbonylated to the corresponding alkane and CO.[8] Consequently, both routes lead to an alkane with one carbon less than the fatty acid, *i.e. n*-heptadecane (C_{17}) from stearic acid (C_{18}).

Two problems are prominent with Ni based catalysts. Their intrinsic rate for hydrogen addition reactions to oxygenates is significantly lower than those of noble metals and, moreover, Ni tends to form relatively large metal particles, further reducing the overall catalytic activity.[3a] Therefore, the focus of this research included Cu, as a catalyst component, that is well-known to catalyze hydrodeoxygenation of fatty acids to alcohols (*e.g.*, Adkins catalyst)[9] and which also helps keeping the base metal catalysts dispersed.[10] Thus, the impact of Cu on the Ni/ZrO_2 based catalysts is explored in this chapter, showing that both the fraction of exposed metal as well as the electronic properties were favorable modified to enhance the rates of hydrodeoxygenation and decarbonylation.

4.3 Results and Discussion

4.3.1 Catalyst characterization

Physicochemical properties

Five catalysts with different Ni_xCu_{1-x}-ratios were prepared, ranging from ZrO_2 supported pure Ni to pure Cu catalysts. The labeling denotes the atomic fraction of the two elements. The overall concentration of Ni and Cu is compiled in **Table 4-1**. N_2 physisorption showed the specific surface area of all catalysts to be (84 ± 3) $m^2 \cdot g^{-1}$. The varying Ni_xCu_{1-x}-concentrations did not influence the overall specific surface area. However, as the Cu and Ni fractions increased from 0.21:0.79 to 0.71:0.29, the dispersion of Ni increased from 1.5 to 2.8% and the particle size of Ni decreased from 68 to 36 nm (except Ni/ZrO_2) as calculated from H_2-chemisorption [11] and determined from the line broadening of the Ni peaks in the X-ray diffractogram (XRD).[12] The acid-base-properties of the catalysts did not change across all catalysts. The acidity was 0.19 ± 0.04 $m$mol·g^{-1}, the basicity 0.27 ± 0.02 $m$mol·g^{-1}, both originating from the ZrO_2 support.[13] From the constant BET surface area, concentration of acid-base-sites and diffraction pattern it is concluded that the support was not modified by

the present preparation method and subtle variations did not influence the kinetic measurements.

Table 4-1: Physicochemical properties of bimetallic Ni_xCu_{1-x}/ZrO_2 catalysts.

Catalyst [a]	S_{BET}	wt% Ni [b]	wt% Cu [b]	$d_{Ni(111)}$ [c]	$d_{Cu(111)}$ [c]	D_{Ni} [d]	d_{Ni} [d]	Conc. of acid sites [e]	Conc. of basic sites [f]
	$[m^2 \cdot g^{-1}]$	[%]	[%]	[nm]	[nm]	[%]	[nm]	$[m\text{mol} \cdot g^{-1}]$	$[m\text{mol} \cdot g^{-1}]$
Ni/ZrO_2	82	10	0	20	-	3.5	29	0.19	0.28
$Ni_{0.79}Cu_{0.21}/ZrO_2$	81	7.5	2.1	10	-	1.5	68	0.23	0.27
$Ni_{0.59}Cu_{0.41}/ZrO_2$	87	5.6	4.2	-	-	1.8	55	0.23	0.27
$Ni_{0.29}Cu_{0.71}/ZrO_2$	83	2.5	6.5	-	85	2.8	36	0.16	0.25
Cu/ZrO_2	85	0	8.7	-	> 100	-	-	0.15	0.29

[a] Label according to molar ratio of Cu-Ni. [b] Determined by AAS. [c] Calculated from XRD by Scherrer equation. [d] Dispersion (D) and particle size (d) were determined by H_2-Chemisorption. [e] Determined by TPD of NH_3. [f] Determined by TPD of CO_2.

Monoclinic ZrO_2 was detected by X-ray powder diffractogram (XRD) *via* the corresponding peaks at 24.5, 28.3, 31.6, 34.5°, 35.3° and 40.7° (JCPDS card No. 37-1484)[14] (**Figure 4-1**). A small shoulder at 30.2° is assigned to *tetragonal* ZrO_2 (JCPDS card No. 17-0923),[15] but it was only present in very low concentrations. Most diffractograms showed the distinctive peaks of Ni(111) at 44.6° and Ni(200) at 51.9° corresponding to Ni^0 (JCPDS 04-0850)[16] primarily for Ni/ZrO_2.
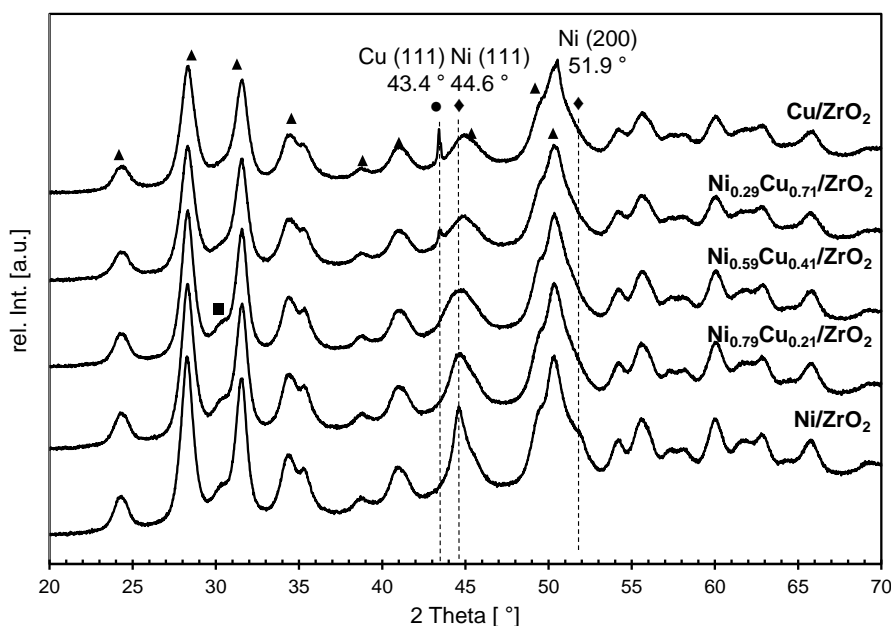
Figure 4-1. XRD patterns of Ni_xCu_{1-x}/ZrO_2 (x = 1, 0.79, 0.59, 0.29, 0) in the 2θ range of 20-70°. *Monoclinic* ZrO_2 (▲), *tetragonal* ZrO_2 (■).
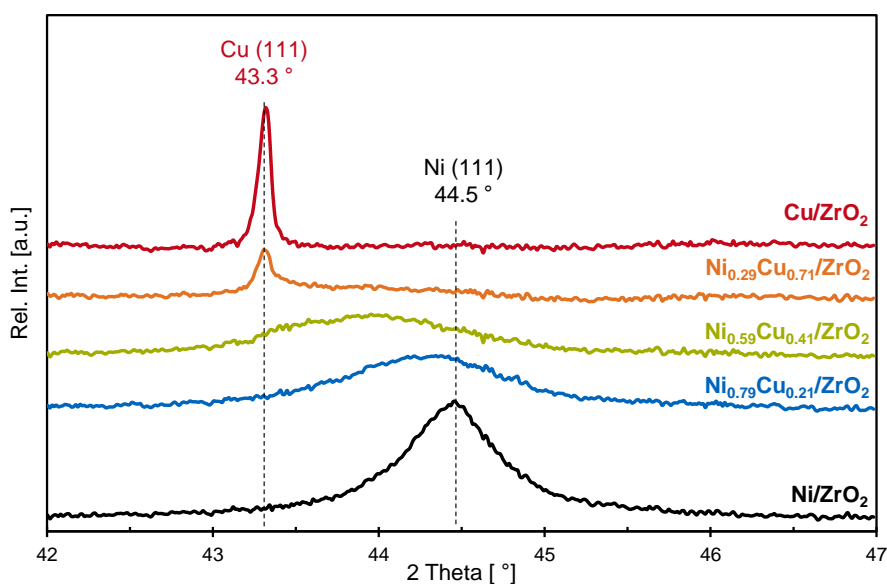
Figure 4-2. XRD patterns of Ni_xCu_{1-x}/ZrO_2 (x = 1, 0.79, 0.59, 0.29, 0) catalysts by subtraction of the support m-ZrO_2 in the 2θ range 42-47°.

In contrast, a signal of Cu(111) at 43.4° was only observed for Cu/ZrO_2 and $Ni_{0.29}Cu_{0.71}/ZrO_2$ (JCPDS 04-0836).[16] The Cu(200) peak at 50.6° overlaps with ZrO_2(220) at 50.1°.[15a, 17] it should be noted that the particle size of Cu in Cu/ZrO_2 is beyond the limitation of the Scherrer equation.[18] Between the peak of Cu(111) at 43.4° and Ni(111) 44.6° a broad signal appeared, attributed the presence of a Ni_xCu_{1-x}-alloy.[16] This broad reflection is

more visible, after subtraction of the m-ZrO_2 pattern (**Figure 4-2**), a peak broadening for increasing Cu content is overserved, which can be assigned to a decrease of the particle size of the alloy.

Figure 4-3 shows the IR spectra of adsorbed CO on various Ni_xCu_{1-x}/ZrO_2 catalysts at 40 °C and $p(CO)$ = 0.3 $m$bar. For monometallic Ni/ZrO_2, the band at 2038 cm^{-1} is attributed to linearly bound CO on Ni^0 (CO-Ni).[19] For the bimetallic Ni_xCu_{1-x}/ZrO_2 catalysts, the band of CO-Ni decreased to 2019, 2011 and 2004 cm^{-1} with increasing concentrations of Cu. This gradual downward shift indicates an increase in the electron density at the Ni surface atoms.[11, 20] Using rigid band to approximate the changes, it is hypothesized that electrons from the fully occupied d-band ($4s^1 3d^{10}$) of Cu are donated to the partially unoccupied d-band ($4s^2 3d^8$) of Ni.[20a] Bridged carbonyls (b-CO-Ni) are visible at 1921 cm^{-1} as a distinct peak for Ni/ZrO_2 and a small peak or shoulder for the Ni_xCu_{1-x}/ZrO_2 materials. Cu/ZrO_2 only shows minor adsorption of CO, which led to a band at 2100 cm^{-1}.[11]
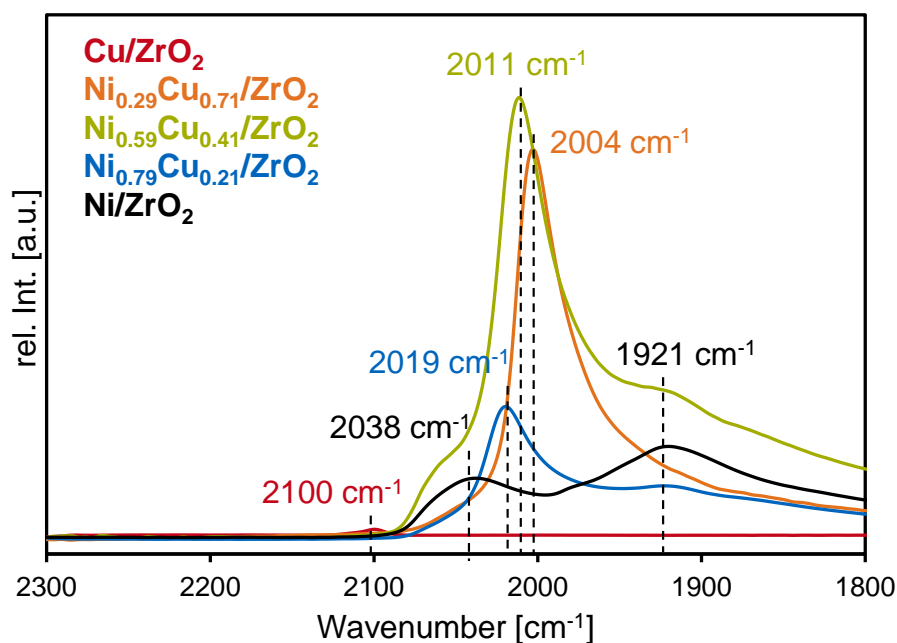
Figure 4-3. IR spectra of CO (0.3 $m$bar) adsorbed at 40 °C on Ni_xCu_{1-x}/ZrO_2 (x = 1, 0.79, 0.59, 0.29, 0).

4.3.2 Kinetic measurements and product distribution

Proposed reaction network for hydrodeoxygenation of stearic acid is shown in **Scheme 4-1**. The first step of the HDO reaction sequence is the hydrodeoxygenation of the stearic acid to octadecanal followed by a reversible hydrogenation to 1-octadecanol. This step is catalyzed by each of Ni, Cu or ZrO_2 with varying rates. In the subsequent step, octadecanal is decarbonylated to *n*-heptadecane. This reaction occurs only on Ni. Catalyzed by Brønsted acid sites, water is eliminated from 1-octadecanol forming *n*-octadecene, which is further hydrogenated to *n*-octadecane. It should be pointed out that additionally 1-octadecanol and stearic acid reversibly form stearyl stearate, which is consumed during the reaction.[6b, 7-8]
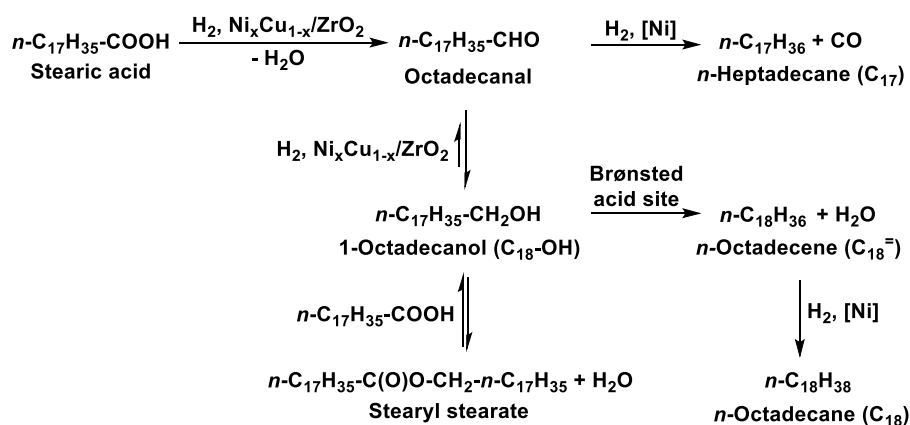
Scheme 4-1. Proposed reaction network for the hydrodeoxygenation of stearic acid.[6b, 7-8]

The reaction network presented in **Scheme 4-1** consists of two key pathways, which require in-depth analysis, (i) the hydrodeoxygenation to 1-octadecanol *via* octadecanal and (ii) the decarbonylation of octadecanal. As presented previously, the hydrodeoxygenation of stearic acid to the aldehyde is the rate determining step on Ni/ZrO_2 (**Scheme 4-1**).[6a] Since this reaction step can be catalyzed by all catalyst components, adjustments of the individual rates to hydrodeoxygenation are critical in order to achieve higher activity.
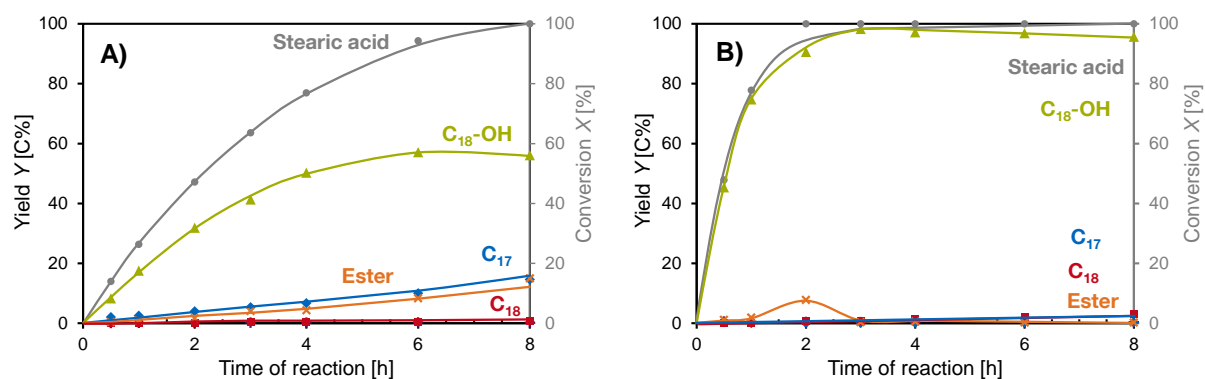
Figure 4-4. Product distribution for the hydrodeoxygenation of stearic acid over Ni/ZrO_2 **(A)** and Cu/ZrO_2 **(B)** as a function of time, conversion of stearic acid (●), yield of 1-octadecanol (▲), *n*-heptadecane (♦), *n*-octadecane (■), octadecanal (+) and stearyl stearate (×). Reaction conditions: Stearic acid (0.5 g), Ni/ZrO_2 or Cu/ZrO_2 (0.2 g), dodecane (100 mL), 260 °C, $p(H_2)$ = 40 bar, stirring at 600 rpm.
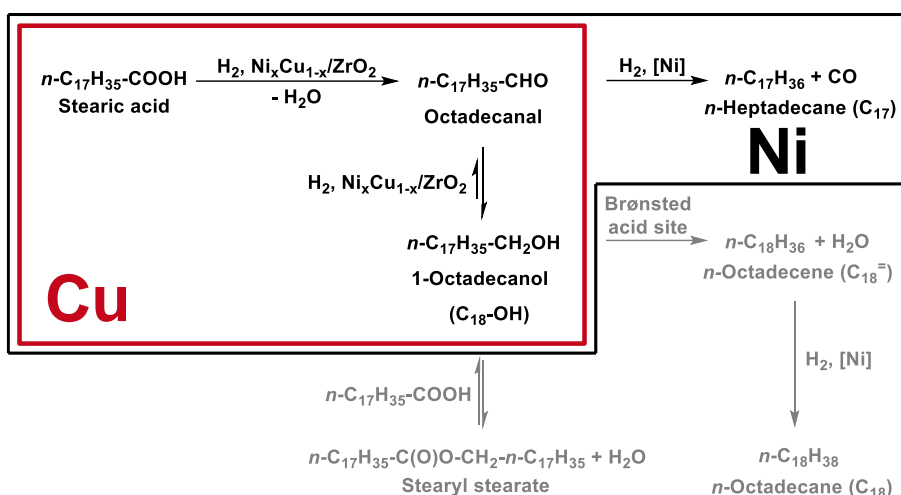
Scheme 4-2. Schematic representation of the hydrodeoxygenation sequence of stearic acid on Ni/ZrO_2 and Cu/ZrO_2.

In **Figure 4-4** the full conversion of stearic acid over Ni/ZrO_2 and Cu/ZrO_2 are compared as a function of time. On both catalysts, hydrodeoxygenation of stearic acid to 1-octadecanol *via* octadecanal appears as a primary reaction, and the formation rates of alkanes including *n*-heptadecane and small amount *n*-octadecane were secondary reactions. Stearyl stearate is concluded to be caused by the reversible esterification between 1-octadecanol and stearic acid and only occurring on Ni/ZrO_2. Despite the fast consumption of stearic acid on Cu/ZrO_2, 1-octadecanol was hardly converted further, in line with earlier observations by Ponec.[21] Thus the formation of hydrocarbons were very slow. In contrast, Ni/ZrO_2 catalysts showed a faster formation of hydrocarbons even though the conversion of stearic acid was

slower.[6a, 7] This observation clearly indicates that Cu is active in the hydrodeoxygenation of the carboxylic acid, but not in the decarbonylation of the aldehyde formed (**Scheme 4-2**).

Stearic acid hydrodeoxygenation

In order to enhance the overall conversion rate of stearic acid, physical mixtures of monometallic Ni/ZrO_2 and Cu/ZrO_2 were used as catalysts. With increasing content of Cu/ZrO_2 in the mixture, the reaction rate increased linearly (**Figure 4-5**). The slope in the yield of 1-octadecanol versus the conversion of stearic acid is only slightly lower than one for all five materials, indicating a very selective conversion (**Figure 4-6**).
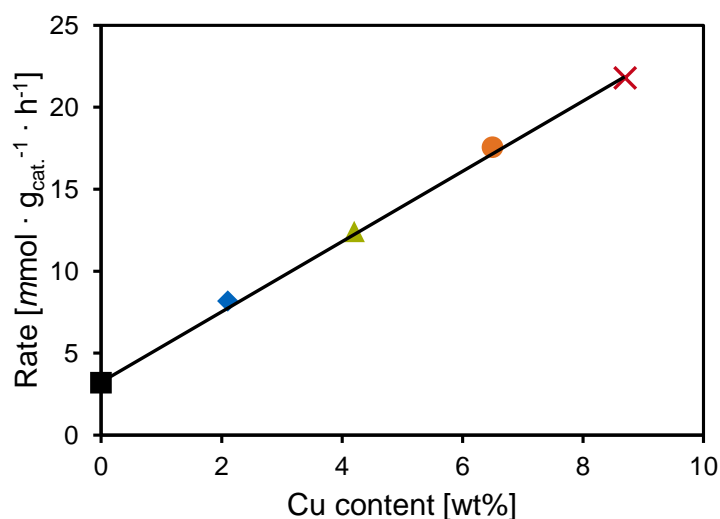
Figure 4-5. Initial reaction rate for the hydrodeoxygenation of stearic acid over physical mixtures of monometallic Ni/ZrO_2 and Cu/ZrO_2 as a function of Cu content. Reaction conditions: Stearic acid (0.5 g), x Ni/ZrO_2 + (1-x) Cu/ZrO_2 catalyst (x = 1, 0.79, 0.59, 0.29, 0, sum 0.05 g), dodecane (100 mL), 260 °C, $p(H_2)$ = 40 bar, stirring at 600 rpm. Cu/ZrO_2 (×), 0.29 Ni/ZrO_2 + 0.71 Cu/ZrO_2 (●), 0.59 Ni/ZrO_2 + 0.41 Cu/ZrO_2 (▲), 0.79 Ni/ZrO_2 + 0.21 Cu/ZrO_2 (♦), Ni/ZrO_2 (■).
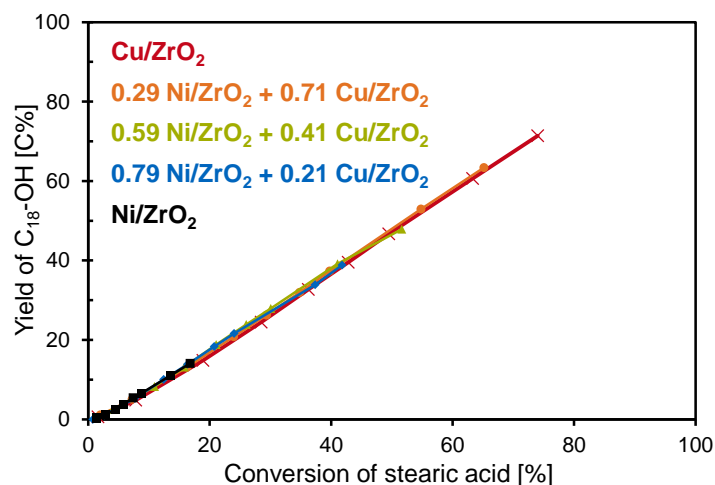
Figure 4-6. Yield of 1-octadecanol as function of stearic acid conversion over physical mixtures of monometallic Ni/ZrO_2 and Cu/ZrO_2. Reaction conditions: Stearic acid (0.5 g), Stearic acid (0.5 g), x Ni/ZrO_2 + (1-x) Cu/ZrO_2 catalyst (x = 1, 0.79, 0.59, 0.29, 0, sum 0.05 g), dodecane (100 mL), 260 °C, $p(H_2)$ = 40 bar, stirring at 600 rpm.

In addition, co-impregnated Ni_xCu_{1-x}/ZrO_2 led to identical reaction rates (**Figure A 4-1, Appendix,** page 104) than for the physical mixtures (**Figure 4-5**). Thus, it is concluded that the alloy formation does not enhance the rate of hydrodeoxygenation.

Decarbonylation of 1-octadecanol

Under typical reaction conditions ($p(H_2)$ = 40 bar), mainly 1-octadecanol is present and the concentration of octadecanal is low at equilibrium concentration.[6a] Thus, to explore the decarbonylation 1-octadecanol was used as starting material. The respective turn over frequencies (TOF) are given in **Figure 4-7**. On Cu/ZrO_2, 1-octadecanol was not converted to *n*-heptadecane. In general, the physically mixed Ni/ZrO_2 + Cu/ZrO_2 catalysts had a slightly higher TOF than Ni/ZrO_2. The similar TOFs for the three physical mixtures demonstrate the absence of a promoting effect on the Ni sites by the physical mixture. In contrast, all co-impregnated Ni_xCu_{1-x}/ZrO_2 catalysts had higher TOF (> 440 $mol_{C_{18}-OH}\cdot mol_{Ni}^{-1}\cdot h^{-1}$) than the physically mixed equivalents (< 125 $mol_{C_{18}-OH}\cdot mol_{Ni}^{-1}\cdot h^{-1}$). This higher activity is attributed to the higher electron density on Ni in Ni_xCu_{1-x}. In line with the lower wave number of adsorbed CO with increasing Cu concentration, the TOFs increased gradually in parallel.
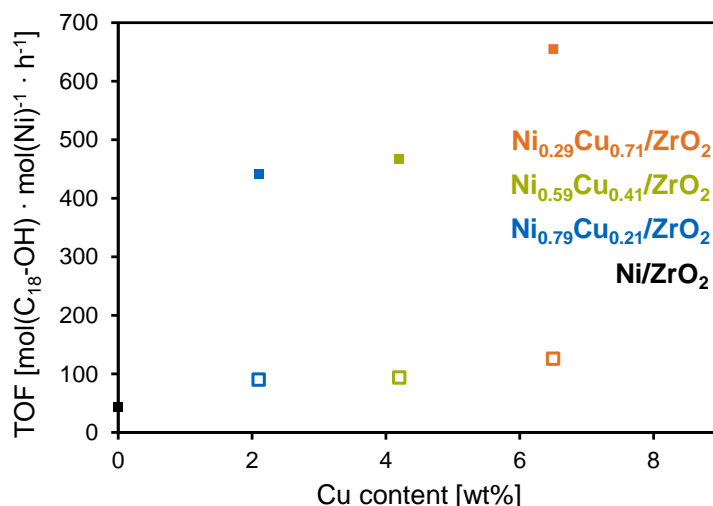
Figure 4-7. Turn over frequency converting 1-octadecanol as a function of Cu content. Reaction conditions: 1-octadecanol (0.5 g), x Ni/ZrO_2 + (1-x) Cu/ZrO_2 (□) or Ni_xCu_{1-x}/ZrO_2 (■), x = 1, 0.79, 0.59, 0.29 (sum 0.05 g), dodecane (100 mL), 260 °C, $p(H_2)$ = 40 bar, stirring at 600 rpm.

Full conversion experiments with stearic acid

The first reaction step (hydrodeoxygenation of the carboxylic acid) occurred mainly on Cu. The second reaction step (decarbonylation of 1-octadecanol) was not catalyzed by Cu (**Figure 4-4**). The yield of 1-octadecanol as a function of reaction time is given for the physical mixtures x Ni/ZrO_2 and (1-x) Cu/ZrO_2 catalyst (x = 1, 0.79, 0.59, 0.29, 0) in **Figure 4-8, A** and for co-impregnated catalysts Ni_xCu_{1-x}/ZrO_2 (x = 1, 0.79, 0.59, 0.29, 0) in **Figure 4-9, A**. Note that the rate for hydrodeoxygenation of stearic acid is the same for physical mixtures and respective Ni_xCu_{1-x}/ZrO_2 catalysts (**Figure A 4-1**). The decarbonylation is more sensitive to the Nickel content and the alloy formation (**Figure 4-7**). Consequently, the same formation rate of 1-octadecanol is seen in **Figure 4-8, A** and **Figure 4-9, A**, but a more rapid consumption of the intermediately formed 1-octadecanol on Ni_xCu_{1-x}/ZrO_2 than on respective physical mixtures. Within the physical mixtures, 0.29 Ni/ZrO_2 + 0.71 Cu/ZrO_2 gave the highest yield of 1-octadecanol after eight hours and consequently the lowest yield of *n*-heptadecane (**Figure 4-8, B**). For the other two mixtures with a higher content of Ni, 1-octadecanol is formed comparably fast, but consumed more rapidly in line with a higher rate of *n*-heptadecane formation. Additionally, the obtained yields of *n*-heptadecane are higher than over pure Ni/ZrO_2,[6a, 7-8] which emphasizes the benefit of Cu/ZrO_2 as a co-catalyst for the conversion of stearic acid to *n*-heptadecane.
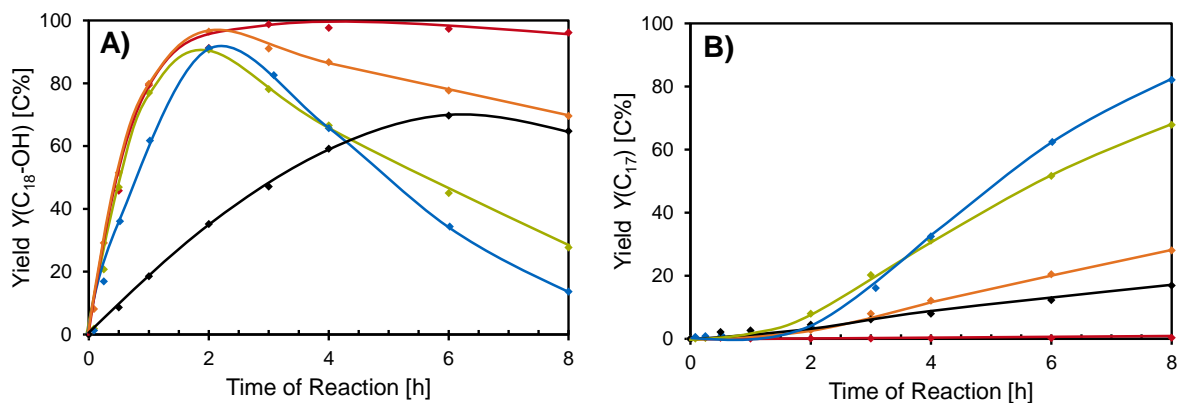
Figure 4-8. Yield of 1-octadecanol (**A**) and yield of *n*-heptadecane (**B**) as function of time over physical mixtures of monometallic Ni/ZrO$_2$ and Cu/ZrO$_2$ (molar ratio Cu:Ni). Reaction conditions: Stearic acid (0.5 g), x Ni/ZrO$_2$ and (1-x) Cu/ZrO$_2$ catalyst (x = 1, 0.79, 0.59, 0.29, 0, sum 0.20 g), dodecane (100 mL), 260 °C, p(H$_2$) = 40 bar, stirring at 600 rpm. Cu/ZrO$_2$ (♦), 0.29 Ni/ZrO$_2$ + 0.71 Cu/ZrO$_2$ (♦), 0.59 Ni/ZrO$_2$ + 0.41 Cu/ZrO$_2$ (♦), 0.79 Ni/ZrO$_2$ + 0.21 Cu/ZrO$_2$ (♦), Ni/ZrO$_2$ (♦).

The TOF (**Figure 4-7**) for the decarbonylation was higher on co-impregnated Ni$_x$Cu$_{1-x}$/ZrO$_2$ catalysts than on physical mixed, leading to a more rapid consumption of 1-octadecanol (**Figure 4-9, A**) and higher yields of *n*-heptadecane (**Figure 4-9, B**). For Ni$_{0.29}$Cu$_{0.71}$/ZrO$_2$, **Figure 4-9, B** shows a lower yield of *n*-heptadecane compared to the other two alloys. Hence, the yield of *n*-heptadecane increased with decreasing Cu content. The influence of the electronic promotion effect of Cu becomes more visible through enhanced decarbonylation. After four hours of reaction, nearly quantitative conversion to *n*-hepta-decane was achieved for Ni$_{0.59}$Cu$_{0.41}$/ZrO$_2$ and Ni$_{0.79}$Cu$_{0.21}$/ZrO$_2$, when starting with stearic acid. In the same time, less than 10% of *n*-heptadecane was formed on Ni/ZrO$_2$.
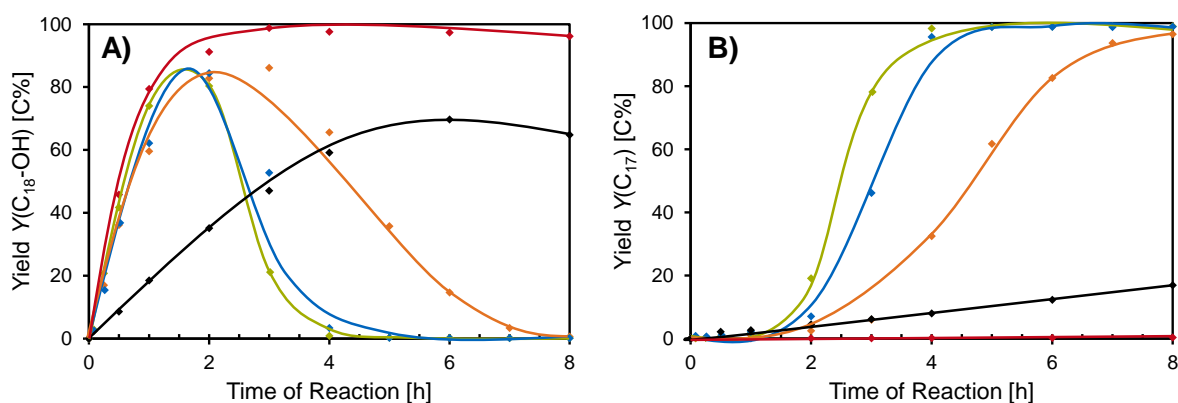
Figure 4-9. Yield of 1-octadecanol over Ni$_x$Cu$_{1-x}$/ZrO$_2$ (**A**) and yield of *n*-heptadecane over Ni$_x$Cu$_{1-x}$/ZrO$_2$ (**B**) as a function reaction time. Reaction conditions: Stearic acid (0.5 g), Ni$_x$Cu$_{1-x}$/ZrO$_2$ catalyst (x = 1, 0.79, 0.59, 0.29, 0, 0.20 g), dodecane (100 mL), 260 °C, p(H$_2$) = 40 bar, stirring at 600 rpm. Cu/ZrO$_2$ (♦), Ni$_{0.29}$Cu$_{0.71}$/ZrO$_2$ (♦), Ni$_{0.59}$Cu$_{0.41}$/ZrO$_2$ (♦), Ni$_{0.79}$Cu$_{0.21}$/ZrO$_2$ (♦), Ni/ZrO$_2$ (♦).

On pure Ni catalyst (*e.g.* Ni/ZrO_2) stearic acid is hydrodeoxygenated to 1-octadecanol and further decarbonylated to alkane.[7-8] In presence of Cu, the first step, the hydrodeoxygenation is enhanced by nearly a factor of eight. The decarbonylation (cleaving a C–C bond) was however, not affected by Cu.[22] The higher electron density of Ni in Ni_xCu_{1-x}-alloy accelerates the decarbonylation of octadecanal to *n*-heptadecane by a factor of four to six (**Figure 4-7**) compared to Ni/ZrO_2. Therefore, the content of Ni and Cu has to be balanced in order combine high conversion rates with a high yield of *n*-heptadecane.

4.4   Conclusions

The physical or chemical mixture of Ni and Cu metal supported on ZrO_2 led to catalysts converting stearic acid to long chain alkanes more efficiently than monometallic Ni/ZrO_2. The conversion rate of stearic acid increased linearly with increasing content of Cu concentration and the selectivity of 1-octadecanol was nearly 100% under initial conditions, independent from the content of Cu and the preparation method. The higher electron density of Ni in Ni_xCu_{1-x}/ZrO_2 enhanced the rate of decarbonylation up to six times compared to Ni/ZrO_2. Too high Cu concentrations in the alloy, however, reduced the rate of *n*-heptadecane formation (not the TOF), because of the lower concentration of nickel available at the surface. Thus, the present catalyst demonstrates how two functions can be combined in this bimetallic catalyst to optimize the conversion of carboxylic acids to alkanes.

4.5   Experimental Section – Materials and Methods

4.5.1   Chemicals

All chemicals, *i.e.*, $Zr(OH)_4 \times H_2O$ (XZO 1247/01, MEL Chemicals), $Ni(NO_3)_2 \times 6 H_2O$ (Acros Organics, ≥98.5%), $Cu(NO_3)_2 \times H_2O$ (Sigma-Aldrich, 99.999%), synthetic air (20.5% O_2/ 79.5% N_2, Westfalen), hydrogen (Westfalen, 99.9999%), argon (Westfalen, 99.9999%), stearic acid (Sigma-Aldrich, ≥99.5% analytical standard), 1-octadecanol (Sigma-Aldrich, ≥99.5% SelectophoreTM), *n*-octadecane (Sigma-Aldrich, 99%), *n*-heptadecane (Sigma-Aldrich, 99%), dodecane (Sigma-Aldrich, ≥99%, ReagentPlus), were purchased commercially and were not further purified.

4.5.2 Catalyst preparation

The support ZrO_2 material was prepared by calcination of $Zr(OH)_4 \times H_2O$ at 400 °C in ambient air for 4 h (heating rate: 10 °C min^{-1}). Bimetallic Ni_xCu_{1-x}/ZrO_2 catalysts with five different Ni_xCu_{1-x}-ratios and a total metal loading of 10 wt% were prepared by wetness impregnation. $Ni(NO_3)_2 \times 6\ H_2O$ and $Cu(NO_3)_2 \times H_2O$ (**Table A 4-1**) were dissolved in de-ionized H_2O (5.0 g), and the resulting solution was added dropwise to the support under stirring in ambient air (co-impregnation). The slurry was further stirred for 4 h, followed by drying at 110 °C overnight. Subsequently, the ground solid was calcined in synthetic air (flow rate: 100 mL min^{-1}) at 450 °C for 4 h (heating rate: 2 °C·min^{-1}) and reduced in H_2 flow (flow rate: 100 mL min^{-1}) at 500 °C for 4 h (heating rate: 2 °C min^{-1}).

4.5.3 Catalyst characterization

X-Ray powder diffraction (XRD) was performed on a Philips X'Pert Pro and a PANalytical Empyrean System equipped with a Cu Kα radiation source (40 kV/45 mA) with a step size of 0.01711° and a scan rate of 1.08° min^{-1} in the 2θ range of 5−70°; with a step size of 0.0131303° and a scan rate of 0.002205° min^{-1} in the 2θ range of 42−47° using Kα1). The particle size of Ni- and Cu-metal clusters was determined from peak broadening of Ni(111) and Cu(111) reflex, fitted with HighScore Plus program,[12] using the Scherrer equation. Deconvoluted diffraction patterns resulted by subtracting the diffractogram of the ZrO_2-support normalized to the maximum intensity of the m-ZrO_2 peak from the diffractogram of Ni_xCu_{1-x}/ZrO_2 catalyst normalized to the maximum intensity of the m-ZrO_2 peak.

N₂-sorption: For measurement of the BET surface area, the sample was activated in vacuum at 250 °C for 2 h before measurement. The adsorption of N_2 was performed at -196 °C by using the Sorptomatic 1990 series instrument.

H₂-chemisorption: After reducing the Ni based catalyst samples in H_2-flow at 450 °C for 1 h, they were evacuated at 300 °C for 1 h. The H_2 adsorption isotherms accounting for both chemisorption and physisorption were measured on a Thermo Scientific's Surfer instrument at a pressure ranging from 9 to 400 $m$bar at 25 °C. For removing physisorbed H_2, the system was evacuated for 20 min afterwards. By extrapolating the isotherm to zero H_2-pressure, the concentration of chemisorbed hydrogen on the metal was determined. The Ni

dispersion was derived by assuming an average surface Ni to H ratio of 1. Furthermore, it is assumed that Cu does not chemisorb H_2.[11]

Temperature programmed desorption (TPD) of ammonia and carbon dioxide was carried out in a parallel reactor system (six fold). A prior activation of the pressed samples (500-710 µm) in He at 500 °C for 1 h was conducted. Consequently, the sample was evacuated at 10^{-2} $m$bar the adsorbent NH_3 or CO_2 was loaded at a partial pressure of 1 $m$bar and 100 °C or 40 °C, respectively. The sample was then purged with He for 1 h in order to remove physisorbed molecules. After activation, the six samples were heated from 100 to 770 °C with a rate of 10 °C·min^{-1} to desorb NH_3 and from 40 to 700 °C to desorb CO_2. The signals were detected by a Balzer QME 200 mass spectrometer. For calibration purposes, NH_3 was desorbed from a HMFI-90 standard and CO_2 generation from $NaHCO_3$ decomposition was used for CO_2 calibration.

Atomic absorption spectroscopy (AAS) was used to determine the Ni and Cu content of the catalysts with a ThermoFisher Solaar M5 AA-Spectrometer. Prior to Ni and Cu determination, the catalysts were dissolved in a mixture of HF, HNO_3 and boiling concentrated H_2SO_4.

IR spectroscopy of adsorbed CO was performed on a Bruker VERTEX 70 spectrometer at a resolution of 2 cm^{-1} with 128 scans in the range of 1000-4000 cm^{-1}. For the measurements, the samples were pressed into self-supporting wafers and mounted in the sample holder. The Ni-Cu/ZrO$_2$ catalysts were activated in H_2-flow at 450 °C for 1 h, and then subsequently outgassed under vacuum ($p = 10^{-7}$ $m$bar) to remove H_2 while cooling to 40 °C. The adsorption of CO was performed at 0.3 $m$bar until equilibrium was reached, then evacuated ($p = 10^{-7}$ $m$bar) for 5 min to remove physisorbed and gas phase CO. The IR spectra of adsorbed CO were obtained by subtracting the activated sample, and then were normalized by the weight of the Ni in the respective wafer.

4.5.4   Catalyst activity and kinetic measurement

Catalytic reactions were carried out in an autoclave (Parr, 300 mL). Stearic acid or 1-octdadecanol, catalyst and 100 mL dodecane were loaded into the autoclave and pressurized with H_2 (3 × 20 bar). Typically, the reaction was carried out at 260 °C in presence of

40 bar H_2 at a stirring speed of 600 rpm. *In situ* sampling was performed during the reaction. Typically, each sample of max. 0.5 mL was withdrawn from the reaction slurry and filtered through a 2 µm filter at the bottom of the reactor in order to make sure that the sample is free of catalyst, that the reaction in the sample vial is stopped and that the mass of catalyst in the reactor stays constant. The dead volume between filter and end of the sampling tube (0.05 mL) was flushed and discarded prior to every sampling. The liquid samples were analyzed by a Agilent 7890B GC system, equipped with a flame ionization detector (FID) and Agilent 5977 MS detector, using a HP-5 capillary column (30 m, 0.32 mm inner diameter, 0.25 µm film). Quantification error is less than ±5% for all experiments.

Conversion = (weight of converted reactant / weight of the starting reactant) × 100%. Yield (C%) = (C atoms in each product / C atoms in the starting reactant) × 100%. Selectivity (C%) = (C atoms in each product/sum of C atoms in all the products) × 100%. The initial reaction rate was deduced from the slope of the linear fit to the conversion *versus* time plot in the linear region at low conversions (<20%). Rate = mole of converted reactant/ mass of catalyst / reaction time. TOF = rate / mole of accessible Ni on the catalyst's surface = mole of converted reactant / mole of accessible Ni on the catalyst's surface / reaction time.

4.6   Contributions

In addition to the author of this thesis, Christoph Denk carried out the full conversion experiments of physical mixed x Ni/ZrO_2 + (1-x) Cu/ZrO_2 catalysts and the experiments with 1-octadecanol as starting material. Eszter Baráth drew the graphical abstract.

4.7 Appendix
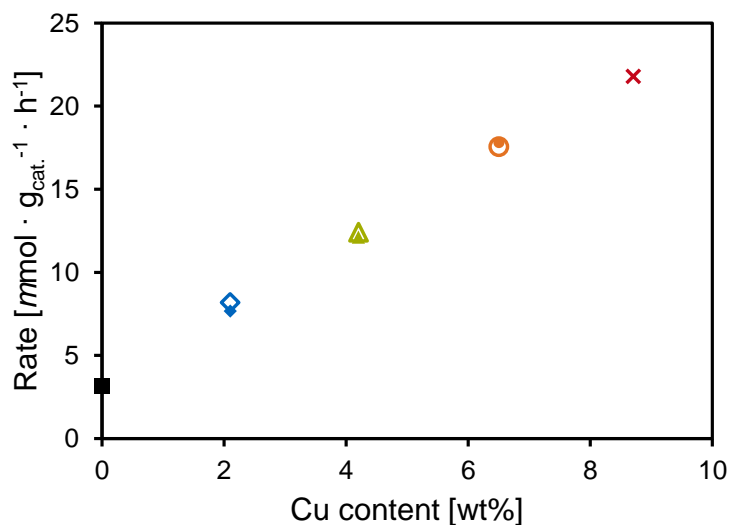
Figure A 4-1. Initial reaction rate for the hydrodeoxygenation of stearic acid over physical mixtures of monometallic x Ni/ZrO_2 and (1-x) Cu/ZrO_2 and co-impregnated Ni_xCu_{1-x}/ZrO_2 as a function of Cu content. Total wt% metal (= Ni+Cu) is 10 wt%. Reaction conditions: stearic acid (0.5 g), $Ni-Cu/ZrO_2$ (0.05 g), dodecane (100 mL), 260 °C, $p(H_2)$ = 40 bar, stirring at 600 rpm. Cu/ZrO_2 (×), 0.29 Ni/ZrO_2 + 0.71 Cu/ZrO_2 (○), 0.59 Ni/ZrO_2 + 0.41 Cu/ZrO_2 (△), 0.79 Ni/ZrO_2 + 0.21 Cu/ZrO_2 (◇), Ni/ZrO_2 (■), $Ni_{0.29}Cu_{0.71}/ZrO_2$ (●), $Ni_{0.59}Cu_{0.41}/ZrO_2$ (▲), $Ni_{0.79}Cu_{0.21}/ZrO_2$ (◆).

Table A 4-1. Detailed amounts of reagents to synthesize bimetallic $Ni-Cu/ZrO_2$ *via* wetness impregnation technique.

Catalyst [a]	$m(ZrO_2)$	$m[Ni(NO_3)_2 \times 6\,H_2O]$	$m[Cu(NO_3)_2 \times H_2O]$
	[g]	[g]	[g]
Ni/ZrO_2	7.0	3.85	–
$Ni_{0.79}Cu_{0.21}/ZrO_2$	7.0	2.89	0.57
$Ni_{0.59}Cu_{0.41}/ZrO_2$	7.0	1.93	1.15
$Ni_{0.29}Cu_{0.71}/ZrO_2$	7.0	0.96	1.72
Cu/ZrO_2	7.0	–	2.30

[a] Label according to atomic ratio of Cu-Ni.

4.8   References

1. Huber, G. W.; Iborra, S.; Corma, A., Synthesis of Transportation Fuels from Biomass: Chemistry, Catalysts, and Engineering. *Chem. Rev.* **2006,** *106*, 4044-4098.

2. Jakkula, J.; Niemi, V.; Nikkonen, J.; Purola, V.-M.; Myllyoja, J.; Aalto, P.; Lehtonen, J.; Alopaeus, V. Process for producing a hydrocarbon component of biological origin. EP1396531B1, 2007.

3. (a) Zhao, C.; Bruck, T.; Lercher, J. A., Catalytic deoxygenation of microalgae oil to green hydrocarbons. *Green Chem.* **2013,** *15*, 1720-1739; (b) Furimsky, E., Chemistry of Catalytic Hydrodeoxygenation. *Catal. Rev.* **1983,** *25*, 421-458.

4. (a) Snåre, M.; Kubičková, I.; Mäki-Arvela, P.; Eränen, K.; Murzin, D. Y., Heterogeneous Catalytic Deoxygenation of Stearic Acid for Production of Biodiesel. *Ind. Eng. Chem. Res.* **2006,** *45*, 5708-5715; (b) Snåre, M.; Kubičková, I.; Mäki-Arvela, P.; Chichova, D.; Eränen, K.; Murzin, D. Y., Catalytic deoxygenation of unsaturated renewable feedstocks for production of diesel fuel hydrocarbons. *Fuel* **2008,** *87*, 933-945; (c) Immer, J. G.; Kelly, M. J.; Lamb, H. H., Catalytic reaction pathways in liquid-phase deoxygenation of C18 free fatty acids. *Appl. Catal., A* **2010,** *375*, 134-139.

5. (a) Hollak, S. A. W.; Gosselink, R. W.; van Es, D. S.; Bitter, J. H., Comparison of Tungsten and Molybdenum Carbide Catalysts for the Hydrodeoxygenation of Oleic Acid. *ACS Catal.* **2013,** *3*, 2837-2844; (b) Gosselink, R. W.; Stellwagen, D. R.; Bitter, J. H., Tungsten-Based Catalysts for Selective Deoxygenation. *Angew. Chem., Int. Ed.* **2013,** *52*, 5089-5092.

6. (a) Peng, B.; Yuan, X.; Zhao, C.; Lercher, J. A., Stabilizing Catalytic Pathways via Redundancy: Selective Reduction of Microalgae Oil to Alkanes. *J. Am. Chem. Soc.* **2012,** *134*, 9400-9405; (b) Peng, B.; Yao, Y.; Zhao, C.; Lercher, J. A., Towards Quantitative Conversion of Microalgae Oil to Diesel-Range Alkanes with Bifunctional Catalysts. *Angew. Chem., Int. Ed.* **2012,** *51*, 2072-2075.

7. Foraita, S.; Fulton, J. L.; Chase, Z. A.; Vjunov, A.; Xu, P.; Baráth, E.; Camaioni, D. M.; Zhao, C.; Lercher, J. A., Impact of the Oxygen Defects and the Hydrogen Concentration on the Surface of Tetragonal and Monoclinic ZrO_2 on the Reduction Rates of Stearic Acid on Ni/ZrO_2. *Chem. - Eur. J.* **2015,** *21*, 2423-2434.

8. Peng, B.; Zhao, C.; Kasakov, S.; Foraita, S.; Lercher, J. A., Manipulating Catalytic Pathways: Deoxygenation of Palmitic Acid on Multifunctional Catalysts. *Chem. - Eur. J.* **2013,** *19*, 4732-4741.

9. Adkins, H.; Folkers, K., Catalytic hydrogenation of esters to alcohols. *J. Am. Chem. Soc.* **1931,** *53*, 1095-7.

10. (a) Brands, D. S.; Poels, E. K.; Bliek, A., Ester hydrogenolysis over promoted Cu/SiO_2 catalysts. *Appl. Catal., A* **1999,** *184*, 279-289; (b) Voeste, T.; Buchold, H., Production of fatty alcohols from fatty acids. *J. Am. Oil Chem. Soc.* **1984,** *61*, 350-2; (c) Turek, T.;

Trimm, D. L.; Cant, N. W., The catalytic hydrogenolysis of esters to alcohols. *Catal. Rev.: Sci. Eng.* **1994,** *36*, 645-83; (d) Song, W.; Zhao, C.; Lercher, J. A., Importance of Size and Distribution of Ni Nanoparticles for the Hydrodeoxygenation of Microalgae Oil. *Chem. - Eur. J.* **2013,** *19*, 9833-9842; (e) Kukushkin, R. G.; Bulavchenko, O. A.; Kaichev, V. V.; Yakovlev, V. A., Influence of Mo on catalytic activity of Ni-based catalysts in hydrodeoxygenation of esters. *Appl. Catal., B* **2015,** *163*, 531-538; (f) Smirnov, A. A.; Khromova, S. A.; Bulavchenko, O. A.; Kaichev, V. V.; Saraev, A. A.; Reshetnikov, S. I.; Bykova, M. V.; Trusov, L. I.; Yakovlev, V. A., Effect of the Ni/Cu ratio on the composition and catalytic properties of nickel-copper alloy in anisole hydrodeoxygenation. *Kinet. Catal.* **2014,** *55*, 69-78; (g) Zavarukhin, S.; Yakovlev, V.; Parmon, V.; Sister, V.; Ivannikova, E.; Eliseeva, O., Development of a process for refining rape seed oil into biodiesel and high-cetane components of diesel fuel. *Chem. Technol. Fuels Oils* **2010,** *46*, 1-8; (h) Dundich, V. O.; Khromova, S. A.; Ermakov, D. Y.; Lebedev, M. Y.; Novopashina, V. M.; Sister, V. G.; Yakimchuk, A. I.; Yakovlev, V. A., Nickel catalysts for the hydrodeoxygenation of biodiesel. *Kinet. Catal.* **2010,** *51*, 704-709; (i) Alonso, D. M.; Wettstein, S. G.; Dumesic, J. A., Bimetallic catalysts for upgrading of biomass to fuels and chemicals. *Chem. Soc. Rev.* **2012,** *41*, 8075-8098; (j) Van der Grift, C. J. G.; Wielers, A. F. H.; Joghi, B. P. J.; Van Beijnum, J.; De Boer, M.; Versluijs-Helder, M.; Geus, J. W., Effect of the reduction treatment on the structure and reactivity of silica-supported copper particles. *J. Catal.* **1991,** *131*, 178-89.

11. Kitla, A.; Safonova, O. V.; Foettinger, K., Infrared studies on bimetallic copper/nickel catalysts supported on zirconia and ceria/zirconia. *Catal. Lett.* **2013,** *143*, 517-530.

12. *HighScore Plus*, 3.0a (3.0.1); PANalytical B.V.: Almelo, 2010.

13. Tanabe, K., Surface and catalytic properties of ZrO_2. *Mater. Chem. Phys.* **1985,** *13*, 347-364.

14. (a) Li, W.; Huang, H.; Li, H.; Zhang, W.; Liu, H., Facile Synthesis of Pure Monoclinic and Tetragonal Zirconia Nanoparticles and Their Phase Effects on the Behavior of Supported Molybdena Catalysts for Methanol-Selective Oxidation. *Langmuir* **2008,** *24*, 8358-8366; (b) Schmid, H. K., Quantitative Analysis of Polymorphic Mixes of Zirconia by X-ray Diffraction. *J. Am. Ceram. Soc.* **1987,** *70*, 367-376.

15. (a) Bachiller-Baeza, B.; Rodriguez-Ramos, I.; Guerrero-Ruiz, A., Interaction of Carbon Dioxide with the Surface of Zirconia Polymorphs. *Langmuir* **1998,** *14*, 3556-3564; (b) Wang, Z.; Jiang, Y.; Hunger, M.; Baiker, A.; Huang, J., Catalytic Performance of Brønsted and Lewis Acid Sites in Phenylglyoxal Conversion on Flame-Derived Silica-Zirconia. *ChemCatChem* **2014,** *6*, 2970-2975; (c) Zhao, Y.; Li, W.; Zhang, M.; Tao, K., A comparison of surface acidic features between tetragonal and monoclinic nanostructured zirconia. *Catal. Commun.* **2002,** *3*, 239-245.

16. Saw, E. T.; Oemar, U.; Tan, X. R.; Du, Y.; Borgna, A.; Hidajat, K.; Kawi, S., Bimetallic Ni–Cu catalyst supported on CeO_2 for high-temperature water–gas shift reaction: Methane suppression via enhanced CO adsorption. *J. Catal.* **2014,** *314*, 32-46.

17. Lin, J.-H.; Biswas, P.; Guliants, V. V.; Misture, S., Hydrogen production by water–gas shift reaction over bimetallic Cu–Ni catalysts supported on La-doped mesoporous ceria. *Appl. Catal., A* **2010,** *387*, 87-94.

18. Alexander, L.; Klug, H. P., Determination of Crystallite Size with the X-Ray Spectrometer. *J. Appl. Phys.* **1950,** *21*, 137-142.

19. Bandara, A.; Dobashi, S.; Kubota, J.; Onda, K.; Wada, A.; Domen, K.; Hirose, C.; Kano, S. S., Adsorption of CO and NO on NiO(111)Ni(111) surface studied by infrared-visible sum frequency generation spectroscopy. *Surf. Sci.* **1997,** *387*, 312-319.

20. (a) Harris, I. R.; Dillamore, I. L.; Smallman, R. E.; Beeston, B. E. P., Influence of d-band structure on stacking-fault energy. *Philos. Mag. (1798-1977)* **1966,** *14*, 325-33; (b) Blyholder, G., Molecular orbital view of chemisorbed carbon monoxide. *J. Phys. Chem.* **1964,** *68*, 2772-8; (c) Gajdoš, M.; Eichler, A.; Hafner, J., CO adsorption on close-packed transition and noble metal surfaces: trends from ab initio calculations. *J. Phys.: Condens. Matter* **2004,** *16*, 1141-1164.

21. Van der Burg, A.; Doornbos, J.; Kos, N. J.; Ultee, W. J.; Ponec, V., Selectivity of nickel-copper and platinum-gold alloys in reactions of butanol and related compounds. *J. Catal.* **1978,** *54*, 243-53.

22. (a) Yun, Y. S.; Park, D. S.; Yi, J., Effect of nickel on catalytic behaviour of bimetallic Cu-Ni catalyst supported on mesoporous alumina for the hydrogenolysis of glycerol to 1,2-propanediol. *Catal. Sci. Technol.* **2014,** *4*, 3191-3202; (b) Harnos, S.; Onyestyák, G.; Valyon, J., A study of the catalytic hydroconversion of biocarboxylic acids to bioalcohols using octanoic acid as model reactant. *Appl. Catal., A* **2012,** *439–440*, 31-40.

Chapter 5

Conclusions and Outlook

Renewable diesel can be produced from microalgae oil and is therefore envisioned as a promising third generation sustainable energy carrier. The potential for increasing the rate of stearic acid conversion of a supported and bi-functional hydrodeoxygenation catalyst and enhancing the selectivity towards desired products was demonstrated. Although it is difficult to differentiate contributions caused by the oxide from those of the metal in supported metal catalysts, the support's properties were separately investigated from the state of the active metals. Due to thorough catalyst characterization, dependencies of the reaction results on catalyst properties could be derived.

One key towards increasing the activity is the role of the support. Bare ZrO_2 support alone is active for the hydrodeoxygenation of stearic acid. The crystal phase of the support has an effect to the overall rate that was deduced to be related to significantly higher adsorption of carboxylic acid on *monoclinic* ZrO_2 than *tetragonal* (Chapter 2). This was measured by IR spectroscopy due to higher concentration of oxygen defects, which were quantified by isotope exchange experiments (TPIE) and the ability of dissociating H_2. From that, a correlation of reaction rate and phase composition of ZrO_2 and a three times higher activity of stearic acid hydrogenation on Ni/m-ZrO_2 than on Ni/t-ZrO_2 could be derived. The experimentally determined reaction rate constants were comparable with fitted values for individual reactions.

In this thesis, the investigations of the support were focused on ZrO_2. Furthermore, the addition of SiO_2, substituted into the crystal lattice of ZrO_2, was forming a binary oxide, increasing the specific surface area of the support, forming novel nano-layered spherical particles and generating Brønsted acid sites (Chapter 3). In proximity of Ni, those BAS promote the conversion of stearic acid. Moreover, the reaction pathway is controlled towards dehydration, increasing the selectivity of n-octadecane over n-heptadecane.

Furthermore, the impact of the active metal site was enhanced without the use of precious metals (Chapter 4). The addition of Cu to Ni (both base metals) increased the rate of 1-octadecanol formation from stearic acid – hence enhancing the first step of the reaction sequence. Mixing Ni with Cu resulted in the formation of a Ni_xCu_{1-x}-alloy with higher electron density at Ni. This catalyzes the decarbonylation of 1-octadecanol to alkane more rapidly, leading to higher yield of *n*-heptadecane. On pure Cu/ZrO_2 no alkanes are formed.

In this thesis, catalysts were developed that increased the rate for the hydrodeoxygenation of stearic acid by an order of magnitude. The perceptions of this work can make a valuable contribution to the mild production of third generation biofuels. They offer magnificent potential for new means of novel catalyst design. Although not explicitly mentioned, the catalysts described in this work are stable and recyclable. In order to develop those systems towards large-scale use and technical application, further investigations in a continuous system are required.

Moreover, many other preparation techniques for advanced ZrO_2 supports with beneficial properties (*e.g.* specific surface area, pore distribution, concentration-, strength- and type of acid sites) that deserve investigation in more depth. Analog, the dispersion of Ni can be increased by alternative preparation conditions leading to a higher rate of hydrodeoxygenation as well. Here, a more homogenous particle size distribution would reduce the scatter of the experimental results.

Chapter 6

Schlussfolgerungen und Ausblick

Erneuerbarer Diesel kann aus Mikroalgenöl hergestellt werden und gilt als vielversprechender und nachhaltiger Energieträger der dritten Generation. In dieser Arbeit wurden Möglichkeiten gezeigt, wie die Reaktionsgeschwindigkeit auf geträgerten und bifunktionellen Katalysatoren für die Hydrodeoxygenierung erhöht und die Selektivität zu erwünschten Produkten verbessert werden kann. Obwohl es bei geträgerten Metallkatalysatoren schwierig ist, die Beiträge des Oxids von denen des Metalls zu differenzieren, wurden die Eigenschaften des Trägers getrennt vom Zustand des aktiven Metalls untersucht. Durch gründliche Charakterisierung der Katalysatoren konnten Ursachen der Reaktionsergebnisse von den Katalysatoreigenschaften ab- und hergeleitet werden.

Der Träger nimmt eine Schlüsselrolle ein um die Aktivität des Katalysators zu erhöhen. ZrO_2 Träger alleine ist bereits für die Hydrodeoxygenierung von Stearinsäure aktiv. Die Kristallphase des Trägers hat einen Einfluss auf die Gesamtrate, was von der signifikant höheren Adsorption der Carboxysäure auf *monoklinem* im Vergleich zu *tetragonalem* ZrO_2 hergeleitet wurde (Kapitel 2). Dies wurde mittels IR Spektroskopie durch eine höhere Konzentration von Sauerstoffdefektstellen gemessen, welche durch Isotopenaustauschexperimente und die Dissoziationsfähigkeit von H_2 quantifiziert wurden. Daraus lässt sich eine Korrelation der Reaktionsrate mit der Phasenzusammensetzung von ZrO_2 und eine dreimal höhere Aktivität der Hydrierung von Stearinsäure auf Ni/m-ZrO_2 als auf Ni/t-ZrO_2 ableiten. Die experimentell bestimmten Reaktionskonstanten waren mit den numerisch bestimmten Werten der einzelnen Reaktionen vergleichbar.

Die Untersuchungen des Trägers waren in dieser Arbeit auf ZrO_2 konzentriert. Des Weiteren wurde durch Zugabe von SiO_2 – eingebaut in das Kristallgitter von ZrO_2 – ein binäres Oxid gebildet, welches die spezifische Oberfläche des Trägers erhöht, neuartige runde Partikel mit Nano-Schichtstruktur bildet und Brønsted-Säure-Zentren generiert (Kapitel 3). In der Nähe von Ni erhöhen diese Brønsted-Säure-Zentren die Umsetzung von

Stearinsäure. Zudem wird der Reaktionspfad zur Dehydratisierung hin gesteuert, was die Selektivität von *n*-Octadecan gegenüber *n*-Heptadecan erhöht.

Weiterhin wurde der Einfluss des aktiven Metallzentrums ohne den Einsatz von Edelmetallen erhöht (Kapitel 4). Durch das Hinzufügen von Cu zu Ni (beides Nichtedelmetalle) wurde die Rate der Bildung von 1-Octadecanol aus Stearinsäure erhöht – folglich wurde der erste Schritt des Reaktionsnetzwerkes verbessert. Durch Mischen von Ni und Cu wurde eine Ni_xCu_{1-x}-Legierung gebildet, die eine höhere Elektronendichte als Ni besitzt. Dadurch wird die Decarbonylierung von 1-Octadecanol zu einem Alkan schneller katalysiert, was zu einer höheren Ausbeute von *n*-Heptadecan führt. Durch reines Cu/ZrO_2 werden keine Alkane gebildet.

In der vorliegenden Arbeit wurden Katalysatoren entwickelt, welche die Reaktionsrate zur Hydrodeoxygenierung von Stearinsäure um mehr als eine Größenordnung erhöhen. Die Erkenntnisse dieser Arbeit können einen wertvollen Beitrag zur Produktion von Biokraftstoffen der dritten Generation unter milden Bedingungen leisten. Sie bieten vielfältige Möglichkeiten, neue Verfahren zur Herstellung neuartiger Katalysatoren zu entwickeln. Auch wenn es nicht ausdrücklich dargestellt wurde, sind die in dieser Arbeit beschriebenen Katalysatoren stabil und mehrfach verwendbar. Um sie für großtechnische Anwendungen nutzbar zu machen, sind weitere anknüpfende Untersuchungen in einem kontinuierlichen Verfahren notwendig.

Darüber hinaus verdienen weitere Präparationsmethoden für hoch entwickeltes ZrO_2 mit vorteilhaften Eigenschaften (z. B. spezifische Oberfläche, Porenverteilung, Konzentration-, Stärke- und Arten von Säurezentren), eine eingehende Untersuchung. Entsprechend kann auch die Dispersion von Ni durch andere Präparationsbedingungen erhöht werden, was zu einer höheren Hydrodeoxygenierungsrate führt. Zudem würde eine homogenere Partikelgrößenverteilung die Streuung der Versuchsergebnisse verringern.

List of Figures and Schemes

List of Tables

Curriculum Vitae

Sebastian Dieter Foraita

Born on February 09, 1987 in Deggendorf

Since 04/2016	Trainee (Brandreferendar) at the Fire Department of Frankfurt am Main
02/2012-03/2016	PhD Student at Technische Universität München, Technische Chemie II, Prof. Dr. Johannes A. Lercher: "Investigation of Ni/ZrO$_2$ catalysts for the hydrodeoxygenation of microalgae oil"
10/2009-11/2011	Master of Science (Chemistry), Technische Universität München

- Technical Chemistry (Major)
- Construction Chemistry (Minor)

04-11/2011	Master's Thesis, Technische Universität München, Construction Chemistry, Prof. Dr. Johann Plank: "Preparation and characterization of new bio-nanocomposite materials consisting of Creatine respectively microbial polysaccharides and layered double-hydroxides"
07-12/2010	Exchange semester, National University of Singapore (NUS)
10/2006-08/2009	Bachelor of Science (Chemistry), Technische Universität München
03-04/2009	Bachelor's Thesis, Technische Universität München, Radiochemistry, Prof. Dr. Andreas Türler: "Electrolytic accumulation of tritium in aqueous solutions – Determining the tritium-separation-factor of platinum cathodes"
08/1997-06/2006	Robert-Koch-Gymnasium Deggendorf
	Final degree: "Allgemeine Hochschulreife"

List of Publications

Journal publications

Sebastian Foraita, Yue Liu, Gary L. Haller, Eszter Baráth, Chen Zhao, Johannes A. Lercher "Controlling Hydrodeoxygenation of Stearic Acid to *n*-Heptadecane and *n*-Octadecane by Adjusting the Chemical Properties of Ni/SiO$_2$-ZrO$_2$", *ChemCatChem* **2017,** *9*, 195-203.

Sebastian Foraita, John L. Fulton, Zizwe A. Chase, Aleksei Vjunov, Pinghong Xu, Eszter Baráth, Donald M. Camaioni, Chen Zhao, Johannes A. Lercher "Impact of the Oxygen Defects and the Hydrogen Concentration on the Surface of Tetragonal and Monoclinic ZrO$_2$ on the Reduction Rates of Stearic Acid on Ni/ZrO$_2$", *Chemistry – A European Journal* **2015**, *21*, 2423-2434.

Baoxiang Peng, Chen Zhao, Stanislav Kasakov, Sebastian Foraita, Johannes A. Lercher "Manipulating Catalytic Pathways: Deoxygenation of Palmitic Acid on Multifunctional Catalysts", *Chemistry – A European Journal* **2013**, *19*, 4732-4741.

Johann Plank, Serina Ng, Sebastian Foraita "Intercalation of Microbial Biopolymers Welan gum and EPS I into Double Layered Hydroxides", *Zeitschrift für Naturforschung B* **2012,** *67b*, 479-487.

Oral presentations

Sebastian Foraita, Eszter Baráth, Chen Zhao, Johannes A. Lercher "Novel sponge shaped high surface area SiO$_2$-ZrO$_2$ supports for hydrodeoxygenation of stearic acid with Ni/SiO$_2$-ZrO$_2$" DGMK Conversion of Biomass, 12.-14. May 2014, Rotenburg a.d. Fulda, Germany

Sebastian Foraita, Eszter Baráth, Chen Zhao, John L. Fulton, Zizwe A. Chase, Donald M. Camaioni, Aleksei Vjunov, Johannes A. Lercher "Effect of Zirconia Morphology of Ni/ZrO$_2$ for Stearic Acid Hydrodeoxygenation" 247th American Chemical Society National Meeting & Exposition, 16.-20. March 2014, Dallas (TX), USA

Poster presentations

"Effect of ZrO_2 morphology and novel doughnut shaped high surface area supports for hydrodeoxygenation of stearic acid with Ni/ZrO_2" Sebastian Foraita, Eszter Baráth, Chen Zhao, Johannes A. Lercher, 47th Annual Meeting German Catalysis Society, March 2014, Weimar, Germany

"The Impact of Zirconia Morphology on Hydrodeoxygenation of Stearic Acid with Ni/ZrO_2" Sebastian Foraita, Chen Zhao, Johannes A. Lercher, 46th Annual Meeting German Catalysis Society, March 2013, Weimar, Germany

"The Support Influence and the Role of Zirconia Morphology on Hydrodeoxygenation of Stearic Acid over Ni/ZrO_2" Sebastian Foraita, Chen Zhao, Johannes A. Lercher, 6th IDECAT/ERIC-JCAT Conference on Catalysis, March 2013, Brixen, Italy

"Selective transformation of algae oil to diesel range alkanes with Ni/ZrO_2" Baoxiang Peng, Sebastian Foraita, Chen Zhao, Johannes A. Lercher, 15th International Congress on Catalysis, July 2012, Munich, Germany

"Hydrocarbon biodiesel production from microalgae oil with Ni/zeolite" Baoxiang Peng, Sebastian Foraita, Chen Zhao, Johannes A. Lercher, Energy Challenges 2050, Munich School of Engineering, June 2012, Munich, Germany

Statutory Declaration

I declare that I have authored this thesis independently, that I have not used other than the declared sources and resources, and that I have explicitly marked all material which has been quoted either literally or by content from the used sources. At the end of each chapter all collaborators are listed and their specific contribution is addressed. Published content of this thesis is clearly marked at the beginning of each chapter and reused according to the terms of the publisher. The content of chapter 4 is about to be published as well.

München, _____   _____